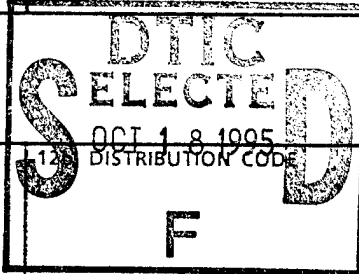


REPORT DOCUMENTATION PAGE

Form Approved
OMB No. 0704-0188

Public reporting burden for this collection of information is estimated to average 1 hour per response, including the time for reviewing instructions, searching existing data sources, gathering and maintaining the data needed, and completing and reviewing the collection of information. Send comments regarding this burden estimate or any other aspect of this collection of information, including suggestions for reducing this burden, to Washington Headquarters Services, Directorate for Information Operations and Reports, 1215 Jefferson Davis Highway, Suite 1204, Arlington, VA 22202-4302, and to the Office of Management and Budget, Paperwork Reduction Project (0704-0188), Washington, DC 20503.

1. AGENCY USE ONLY (Leave blank)	2. REPORT DATE	3. REPORT TYPE AND DATES COVERED
	10 Sep 95	
4. TITLE AND SUBTITLE The Initiation and Development of A Long-Lived, High Plains Squall Line		5. FUNDING NUMBERS New 125
6. AUTHOR(S) Rodney Lynn Grady		
7. PERFORMING ORGANIZATION NAME(S) AND ADDRESS(ES) AFIT Students Attending: Pennsylvania State University		8. PERFORMING ORGANIZATION REPORT NUMBER 95-108
9. SPONSORING/MONITORING AGENCY NAME(S) AND ADDRESS(ES) DEPARTMENT OF THE AIR FORCE AFIT/CI 2950 P STREET, BLDG 125 WRIGHT-PATTERSON AFB OH 45433-7765		10. SPONSORING/MONITORING AGENCY REPORT NUMBER
11. SUPPLEMENTARY NOTES		
12a. DISTRIBUTION / AVAILABILITY STATEMENT Approved for Public Release IAW AFR 190-1 Distribution Unlimited BRIAN D. GAUTHIER, MSgt, USAF Chief of Administration		
13. ABSTRACT (Maximum 200 words)		

DTIC QUALITY INSPECTED 6

14. SUBJECT TERMS		15. NUMBER OF PAGES 109
		16. PRICE CODE
17. SECURITY CLASSIFICATION OF REPORT	18. SECURITY CLASSIFICATION OF THIS PAGE	19. SECURITY CLASSIFICATION OF ABSTRACT
		20. LIMITATION OF ABSTRACT

The Pennsylvania State University
The Graduate School
Department of Meteorology

THE INITIATION AND DEVELOPMENT
OF A LONG-LIVED, HIGH PLAINS SQUALL LINE

Accesion For	
NTIS CRASH	<input checked="" type="checkbox"/>
DTIC TAB	<input type="checkbox"/>
Unannounced	<input type="checkbox"/>
Justification	
By	
Distribution /	
Availability Codes	
Dist	Avail and / or Special
A-1	

A Thesis in
Meteorology

by

Rodney Lynn Grady

Submitted in Partial Fulfillment
of the Requirements
for the Degree of

Master of Science

August 1995

19951017 136

We approve the thesis of Rodney Lynn Grady.

Date of Signature



Johannes Verlinde
Assistant Professor of Meteorology
Thesis Adviser

15 June 1995


J. Michael Fritsch
Professor of Meteorology

17 June 1995


Dennis W. Thomson
Professor of Meteorology
Head of the Department of Meteorology

19 June 95

ABSTRACT

A non-severe squall line that developed on 21 June 1993 along the northern foothills of the Colorado Rocky Mountains is analyzed using a series of triple-Doppler analyses and compared to the conceptual model for a typical squall line with trailing stratiform rain area. One group of numerical modelers has successfully modeled many of the features identified within the conceptual model. Based on the simulations, they hypothesize that the observed features can be explained through a balance between the circulations induced by the low-level ambient vertical shear of the horizontal wind ahead of the line and that induced by the horizontal buoyancy gradient along the leading edge of the convectively generated cold pool. These circulations dictate the orientation of the updraft which is key to understanding the structure and longevity of squall lines. Although this balance may be significant in some cases, observations in this case suggest that in differing environments, the hypothesis may need to be expanded.

While the low-level shear has been identified as most critical to squall line development, strong upper-level shear present in this case was significant to the establishment of a forward anvil. The forward anvil allowed

for the development of a suppression zone which in turn resulted in a discrete mode of squall line propagation.

The drier thermodynamic profile, as characterized by a higher lifting condensation level, and weak low-level shear resulted in convection forming not along, but rather 7-10 km behind the leading edge of the shallow cold pool. At this location, the hypothesized circulations were not a factor and any tilt of the updraft came through the conservation of momentum and non-hydrostatic forces.

TABLE OF CONTENTS

LIST OF FIGURES	vi
LIST OF TABLES	x
ACKNOWLEDGEMENTS	xi
Chapter 1. INTRODUCTION	1
Chapter 2. DATA SOURCES AND METHOD OF ANALYSIS	8
Chapter 3. SYNOPTIC OVERVIEW AND SQUALL LINE MORPHOLOGY	13
3.1. Synoptic Environment	13
3.2. Radar and Satellite Overview	20
3.3. Surface Reflection of the Squall Line	34
Chapter 4. MESOSCALE ENVIRONMENT	37
4.1. Pre-MCS Initiation	37
4.2. MCS Initiation	45
Chapter 5. DOPPLER RADAR ANALYSIS	55
5.1. 2017 Doppler and 2015 Mesonet Analyses	55
5.2. 2102 Doppler and 2100 Mesonet Analyses	60
5.3. Vertical Profiles of Kinematic Fields	70
Chapter 6. DISCUSSION	82
6.1. Impacts of Shear	84
6.2. Impacts of Thermodynamics and Topography	89
Chapter 7. SUMMARY AND CONCLUSIONS	96
REFERENCES	103

LIST OF FIGURES

1. Conceptual model of a squall line with a trailing stratiform area viewed in a vertical cross-section oriented normal to the line (from Houze et al. 1990)	4
2. Topographic map of the RAPS-93 area with instrument locations	9
3. Upper air analysis for 1200 UTC 21 June 1993 at 500 hPa	14
4. Synoptic surface analysis for 1200 UTC 21 June 1993	15
5. The Denver skew T-log P sounding for 1200 UTC 21 June 1993 and a CLASS sounding for 1700 UTC 21 June 1993	17
6. Synoptic surface analysis for 1800 UTC 21 June 1993	18
7. The 1700 UTC CLASS sounding modified with 1930 UTC 21 June 1993 surface conditions	19
8. Enhanced infrared GOES satellite images showing the intensification of the MCS between 2000 and 2300 UTC 21 June 1993	22
9a-c. Enhanced infrared GOES satellite images showing the breadth and longevity of the MCS between 0000 and 1200 UTC 22 June 1993 ..	23
9d-f. Enhanced infrared GOES satellite images showing the breadth and longevity of the MCS between 1800 UTC 22 June 1993 and 0600 UTC 23 June 1993	24
10a. Horizontal MHR reflectivity cross-section at 3.0 km for 1957 UTC and PROFS/PAM mesonet winds for 2000 UTC 21 June 1993	25
10b. Horizontal MHR reflectivity cross-section at 3.0 km for 2033 UTC and PROFS/PAM mesonet winds for 2030 UTC 21 June 1993	27
10c. Horizontal MHR reflectivity cross-section at 3.0 km for 2103 UTC and PROFS/PAM mesonet winds for 2100 UTC 21 June 1993	28

10d. Horizontal MHR reflectivity cross-section at 3.0 km for 2127 UTC and PROFS/PAM mesonet winds for 2130 UTC 21 June 1993	30
10e. Horizontal MHR reflectivity cross-section at 3.0 km for 2203 UTC and PROFS/PAM mesonet winds for 2200 UTC 21 June 1993	31
10f. Horizontal MHR reflectivity cross-section at 3.0 km for 2233 UTC and PROFS/PAM mesonet winds for 2230 UTC 21 June 1993	32
10g. Horizontal MHR reflectivity cross-section at 3.0 km for 2335 UTC and PROFS/PAM mesonet winds for 2330 UTC 21 June 1993	33
11. Time series plot of PAM station 10 data from 1900 UTC on 21 June 1993 until 0100 UTC 22 June 1993	35
12a. Mesonet surface analysis for 1200 UTC 21 June 1993	38
12b. Mesonet surface kinematic analysis for 1200 UTC 21 June 1993	39
13a. Mesonet surface analysis for 1700 UTC 21 June 1993	40
13b. Mesonet surface kinematic analysis for 1700 UTC 21 June 1993	41
14. Time series of the 12 °C isodrosotherm between 1200 and 1500 UTC 21 June 1993	43
15. Mesonet surface analysis for 1800 UTC 21 June 1993	44
16a. Time series plot of PAM station 12 data between 1800 and 2100 UTC 21 June 1993	46
16b. Vertical time series plot of virtual potential temperature between 1900 and 2000 UTC 21 June 1993	47
17. Mesonet surface analysis for 1940 UTC 21 June 1993	52
18. EVAD vertical profiles of horizontal divergence and vertical velocities for 1937 UTC 21 June 1993	53

19.	Horizontal triple-Doppler analysis at 3.0 km for 2017 UTC 21 June 1993	56
20.	Vertical triple-Doppler analysis for southern of the squall line at 2017 UTC and the northern end at 2045 UTC 21 June 1993	59
21.	Mesonet surface analysis for 2015 UTC 21 June 1993	61
22.	Horizontal triple-Doppler analysis at 3.0 km for 2102 UTC 21 June 1993	62
23.	Vertical triple-Doppler analysis for southern end of the squall line at 2102 UTC and the northern end at 2131 UTC 21 June 1993	64
24.	Vertical cross-section of isotachs of the averaged u-component of the wind perpendicular to the southern end of the squall line at 2102 UTC 21 June 1993	66
25.	Horizontal dual-Doppler analysis at 7.5 km for the northern end of the squall line at 2131 UTC 21 June 1993	67
26.	Mesonet surface analysis for 2100 UTC 21 June 1993	69
27.	Vertical time series plot of horizontal divergence of the southern end of squall line between 1958 and 2115 UTC 21 June 1993	71
28.	Time series plot of the maximum vertical velocities for a WKR numerical simulation and the southern end of the squall line for the first 90 minutes	72
29.	Vertical time series plot of averaged winds for the front and back of the southern end of the squall line between 2014 and 2115 UTC 21 June 1993	74
30.	Vertical time series plot of horizontal divergence of the northern end of squall line between 2032 and 2129 UTC 21 June 1993	76

31. Vertical time series plot of averaged winds for the front and back of the northern end of the squall line between 2032 and 2115 UTC 21 June 1993	78
32. Vertical time series of the updraft tilt for southern and northern ends of the squall line between 1958 and 2129 UTC 21 June 1993 .	80
33. Ambient wind profiles of the u and v components of wind relative to the differently oriented line using the 1700 UTC CLASS sounding	86
34. Wind profile of the u-component of the wind relative to the storm motion using three WKR numerical simulations and the observed conditions	88

LIST OF TABLES

1. Values of the ratio of the cold pool strength to ambient low-level wind shear for 1938 and 1947 UTC 21 June 1993	50
2. Comparisons between WKR numerical simulations in weakly sheared environments and the observations from the northern and southern ends of the squall line	83

ACKNOWLEDGMENTS

To my Lord and Savior, Jesus Christ, goes all the praise and credit. You got me through the tough times and you cheered me along during the good times.

To my wife Shelly, without you none of this work would have been possible. You were a constant source of love, support, perspective, and acted in the role of Dad much too often. To my five wonderful, God given children, Dad is on his way home!

To the United States Air Force and Air Force Institute of Technology (AFIT) Civilian Institution Program, whose financial support made this academic endeavor possible.

To my advisor, Dr. Johannes (Hans) Verlinde, your immeasurable patience, open door, wisdom, understanding, and computer assistance have made this masters program experience as good as it could possibly be. I am honored to have worked and shared many conversations with you. A heart felt thank you to you and your family.

To my second reader, Dr. Michael Fritsch, your professionalism and meteorological insight have made it a great privilege to have worked with you.

To the many people who provided data in many shapes, sizes, and colors, thank you. Without Dr. Kultegin Aydin, Penn State University, and Bob Rilling, NCAR, the radar data used in this project would not have been possible. Peter

Neilley, NCAR, provided much of the data accumulated during the RAPS-93 field project. Tom Ross, NCDC, provided the profiler data, Dave Merritt, NOAA ERL, provided the Denver 915 MHz RASS data.

This project would have taken a minimum of five years to complete without the many people who provided software and software support. Michele Case, NCAR, was invaluable with her assistance on RDSS. Jay Miller and Bill Anderson, NCAR, provided CEDRIC expertise and help that saved many days of work. Paul Hein and Jason Nachamkin, CSU, provided plotting packages that have allowed this project to be presentable. Art Person and Dave Mornhinweg, PSU, provided assistance in making the PSU software and systems work to their fullest potential.

To all of you and the many others who have helped in various capacities, my sincere appreciation and gratitude is extended. You all made this project possible. Thank you!

Chapter 1

INTRODUCTION

Much of the precipitation that occurs over the Central United States during the summer months occurs at night and has its roots in thunderstorm activity along the eastern slopes of the Rocky Mountains (Wallace 1975, Maddox 1980). Often this convective activity develops into squall lines which, in turn, develop into mesoscale convective complexes (MCCs) (Menard and Fritsch 1989, Schmidt and Cotton 1989). Although MCCs contribute most to the total precipitation (Fritsch et al. 1981, Fritsch et al. 1986), Midwestern squall lines constitute a much higher frequency of occurrence. In Oklahoma alone during the span of 11 years for the months of April, May, and June, Bluestein and Jain (1985) and Bluestein et al. (1987) observed the formation of approximately 150 squall lines.

Because of their number and spatial extent, squall lines have traversed many special higher density observational networks, allowing them to be well documented. Most observational studies of mid-latitude squall lines document the mature stage when a well defined stratiform region exists and the squall line has propagated out of its source region (Ogura and Liou 1980, Zipser and Matejka 1982,

Smull and Houze 1985, Kessinger et al. 1987, Smull and Houze 1987a). However, few case studies have examined the initial stages of squall line development (Bluestein and Jain 1985, Bluestein et al. 1987, Klimowski 1994). In this paper, we investigate the initial stages of a squall line that developed at 1930 UTC on 21 June 1993 over the foothills of the Colorado Rocky Mountains in an environment where the vertical wind shear was weak at low to mid-levels but strong at upper-levels. The mesoscale convective system (MCS) produced hail 14 mm in diameter and surface wind gusts to 19 m s^{-1} within the first two and one-half hours of its existence. This non-severe squall line was part of a much larger MCS that developed around 1730 UTC on 21 June 1993 and persisted till 0800 UTC on 23 June, at which time the system had propagated into Minnesota.

Squall lines are typically long-lived meteorological phenomena. Two mechanisms which cause this longevity have been documented. The first mechanism involves persistent propagating updraft and downdraft couplets co-existing within the same line, and was proposed by Browning and Ludlam (1962) and numerically simulated in 2-D by Moncrieff and Miller (1976), Thorpe et al. (1982; hereafter TMM), and Miller and Moncrieff (1983). Browning and Ludlam's 2-D model was based upon a 3-D supercell in a deeply sheared environment. In the numerical simulations of TMM, they used

a moderate low-level shear environment and found that the developing storm involved only one cell and so was classified as a "2-D supercell". While rotating 3-D supercells are frequently observed, "2-D supercells" have not been documented. The second mechanism, where the squall line propagates through the redevelopment of ordinary cells (Byers and Braham 1949), was first observed and postulated by Newton (1950). Since Newton's first observations, many other recent observations validated this mechanism for longevity as common place (Zipser 1977, Leary and Houze 1979, Gamache and Houze 1982, Houze and Hobbs 1982). The most dominant conceptual model of the structure of a typical squall line that propagates by redevelopment of ordinary cells was presented by Smull and Houze (1987a) and Houze et al. (1989) and is shown in Fig. 1. Flow from a slightly upshear tilted updraft branches into a gradually ascending front-to-rear flow in a predominantly trailing anvil. Another weaker branch of winds off the updraft flows into the leading anvil. Below the trailing anvil is an area of descending rear-inflow that, coupled with downdrafts, helps to keep a nearly continual source of surface convergence and upward motion along the leading edge of the gust front. Along with numerous observations, several numerical modelers have successfully simulated the regeneration propagation mechanism (Dudhia et al. 1987, Rotunno et al.

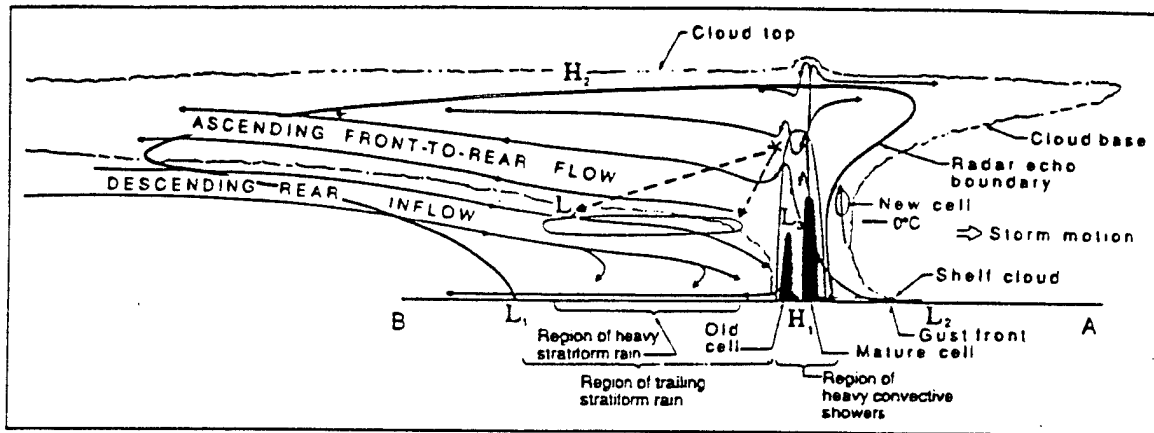


FIG. 1. Conceptual model of a squall line with a trailing stratiform area viewed in a vertical cross-section oriented normal to the line (from Houze et al. 1989).

1988 (hereafter RKW), and Fovell and Ogura 1989). While observations are typically spatially and temporally limited, numerical models afford researchers detail and understanding that is not often possible in a natural environment. From the numerical simulations of RKW, they were able to establish a conceptual model for cell redevelopment and propagation that rested upon the balance between baroclinically generated horizontal vorticity at the cold pool boundary and horizontal vorticity inherent in the ambient vertical low-level wind shear. Along the leading edge of the gust front, the balanced state produced the deepest lifting and was most likely to regenerate strong convective cells. A typical unbalanced state existed when the vorticity induced by an ever increasing cold pool was greater than the vorticity present in the low-level ambient shear. A representative simulation was accomplished in weakly sheared environments (Weisman et al. 1990; hereafter WKR) and resulted in convective cells decaying after 1.5 hours and creating an apparent upshear tilted updraft by 2 hours. Generally speaking, balanced circulations lead to longevity and unbalanced circulations lead to decay. Many of the observed features within mid-latitude squall lines have been explained as a function of this cold pool/low-level ambient shear conceptual model. These features include the tilted updraft and trailing anvil (RKW and WKR),

and rear-inflow jet (Weisman 1992). All these studies used a 3-D non-hydrostatic model and were initialized with similar idealized ambient environmental conditions. The idealized conditions were horizontally homogeneous and characterized by a single sounding representative of typical squall line environments.

In light of the many inhomogeneities present within the environment, many differences and variations to the conceptual model from numerical simulations are found in observations. This wide range of environmental factors that vary both spatially and temporally creates asymmetries within the squall line. Asymmetries in an inhomogeneous environment are normal and found at any stage of the squall line's life. Houze et al. (1990) documented asymmetries in their study of the radar reflectivity patterns of mature squall lines. Bluestein and Jain (1985) and Bluestein et al. (1987) documented the formative stage of squall lines and found that development into a linearly oriented structure occurred in a variety of ways. Most of these asymmetries still occur within the same general conceptual model put forth in Fig. 1 and simulated by RKW, WKR, and Weisman. The significance of this case study is the asymmetries do not fit the conceptual model and therefore suggest that the cold-pool/low-level ambient shear arguments

cannot completely explain all the observed features of squall lines.

The large degree of asymmetries and inhomogeneities observed are dependent upon a number of factors including synoptic and mesoscale forcing, atmospheric stability, vertical wind shear and topography. Under the right set of environmental conditions, the possibility exists to develop an asymmetric, quasi "2-D supercellular" squall line. The 21 June 1993 squall line is such a case.

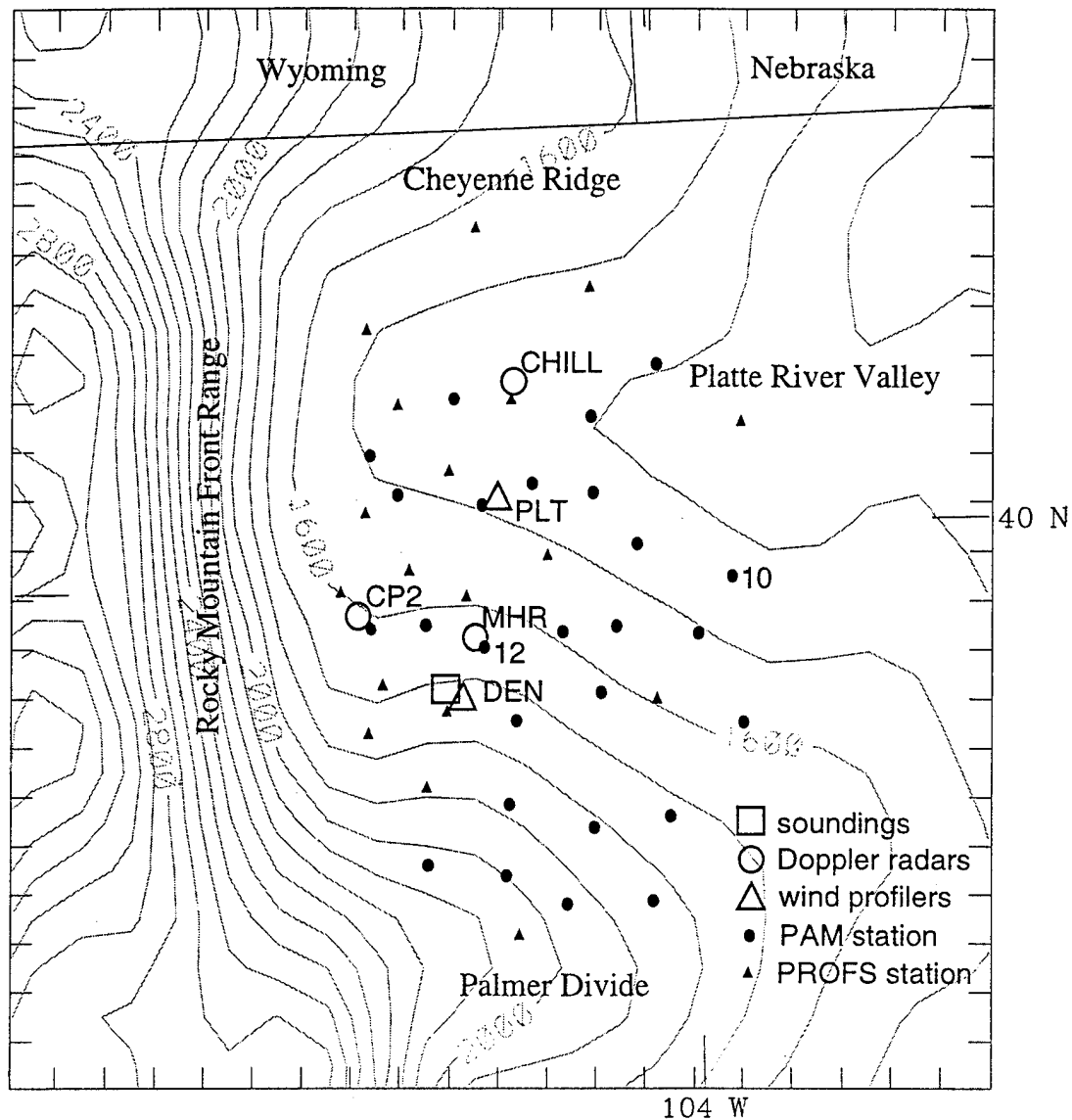
The purpose of this investigation is to document a non-typical, asymmetric squall line and to describe several environmental factors that may have contributed to the atypical, asymmetric structure. Of particular interest is the discrete mode by which the squall line propagated. The following chapter begins with a general description of the data set and analysis procedures. The synoptic situation and squall line overview are then analyzed and presented in chapter 3 followed by a presentation of the mesoscale environment prior to and at squall line initiation in chapter 4. Using Doppler radar analyses and associated meso-analyses, the inhomogeneities within the squall line are drawn out in chapter 5. In chapter 6, the variant environmental factors and their impact on creating a non-typical and asymmetric squall line are discussed, and the summary and conclusions follows in chapter 7.

Chapter 2

DATA SOURCES AND METHODS OF ANALYSIS

The data for the analyses were collected in late morning to early afternoon of 21 June 1993 during the NCAR RAPS-93 (Realtime Analysis and Prediction of Storms, 1993, Neilliey et al. 1993) field project. Fig. 2 shows the locations of the surface mesonet, wind profilers, radio acoustic sounding system (RASS), rawinsondes, and Doppler radars used in this analysis.

Surface data were collected every five minutes from the NOAA Program for Regional Observing and Forecasting Services (PROFS) mesonet and additional Portable Automated Mesonet (PAM) observing platforms. Surface pressure data were adjusted to 1500 m MSL and individual station biases were corrected through comparison with National Weather Service (NWS) Standard Airways Observations (SAO). Objective analyses of kinematic fields were accomplished using the mesonet data interpolated to a 8 km grid using a nearest neighbor analysis grid. Dew point temperatures for the PROFS Keenesburg, CO station prior to 2030 UTC 21 June 1993 were removed because of an apparent stuck hygrometer and pressures for the PAM station 3 were removed because of wildly fluctuating values. The 915-MHz Denver/Stapleton



wind profiler and companion NOAA/Wave Propagation Laboratory RASS (Strauch et al. 1984) measured the vertical wind structure and the derived virtual temperature profile (Marshall et al. 1972) respectively. The RASS observations were taken at 150 m intervals through the lowest 1.5 km AGL. Height coordinates were converted to pressure coordinates by integrating the hydrostatic equation upward, using the surface observation as the lower boundary condition and RASS virtual temperatures as the mean-level temperatures, in order to calculate virtual potential temperatures (Neiman et al. 1991). Standard NWS rawinsonde observations and a supplemental CLASS sounding were used in calculating vertical environmental quantities. Rawinsonde data were analyzed using a software package developed at the National Center for Atmospheric Research (NCAR) called "The System for User-editing and Display of Soundings" (SUDS) (Burghart 1993).

The S-band radars used in the analysis included the NCAR, CP2 and CSU-CHILL Doppler and dual-polarization radars, as well as the Mile High Doppler radar (MHR). The dual-Doppler lobes were defined to be the intersection between the area of a between-beam angle $30^\circ \leq \theta \leq 150^\circ$ and the area that provided 1.5 km spatial resolution (Davies-Jones 1979). Reflectivities and Doppler velocities were initially edited and unfolded using the interactive software

Research Data Support System (RDSS) (Oye and Carbone 1981), and then interpolated onto a Cartesian grid using REORDER (Oye 1994). The grid extended up to 14.0 km AGL, with horizontal and vertical spacing of 1.5 and 0.5 km respectively.

Before the radial velocity and reflectivity fields were advected to a volume-scan average time, data voids left from side-lobe problems were filled using a local-least-squares method with stringent constraints. A final composite reflectivity field was developed using the maximum value at each grid point from either of the three radars. Using the software CEDRIC (Mohr et al. 1983), the horizontal wind field was calculated from the three radial wind fields using a three-equation solution. Where data from only two of the radars were available, a two-equation solution was implemented. A two-step Leise filter (Leise 1981) was used to smooth the horizontal winds, completely damping all disturbances shorter than four times the horizontal grid spacing, or 6 km. Vertical motions were obtained using a downward integration of the mass continuity equation that required the upper boundary at storm top to equal zero. The vertical velocities for the northern end of the convective line are suspect for analyses through 2102 and for portions of analyses 2102 through 2130. This is due to CSU-CHILL's maximum elevation scan of 13° not resolving storm-top while

the MCS was in close proximity to the radar. An unresolved storm-top does not pose problems to the derived horizontal winds and its derivatives, since at the low elevation scans, the radial velocities measured by the radar were comprised predominantly from the horizontal component of the winds. Vertical cross-sections and profiles of selected kinematic fields shown in chapter 5 were constructed using averaged, normal-to-the-line cross-sections of certain cells and line segments specified within the text. These cells and lines were defined by their alongline 40 dBZ reflectivity extent. Squall line motion was determined from the average movement of discernable reflectivity cores. The reflectivity cores and the axis of highest reflectivities within the convective line were observed to move at the same speed and direction. Therefore, an average cell and line movement (241° at 7.9 m s^{-1}) was subtracted from Doppler derived winds to yield line relative flow. The average direction varied by 15° and the average speed varied by 1.5 m s^{-1} .

Satellite imagery of Colorado from GOES-7 were processed using Unidata McIDAS. Regional satellite imagery from GOES-7 were processed by Weather Services Incorporated of Bedford, MA.

Chapter 3

SYNOPTIC OVERVIEW AND SQUALL LINE MORPHOLOGY

3.1. Synoptic Environment

The environment of MCS birth and growth was influenced by a slow moving, upper-level, short-wave trough, located over Colorado and Wyoming that is readily evident at 1200 UTC (all times hereafter UTC), 21 June (Fig. 3). Satellite images and vorticity analyses helped to identify the trough position upstream from the Colorado Front Range. Also present at this time was a north to south oriented 700 hPa thermal ridge shown in Fig. 3 as the thick line. A time series (not shown) of the horizontal wind profiles at the Platteville wind profiler, located 49 km north of the Denver rawinsonde site, indicated passage of the trough at roughly 1600-1700.

On the surface at 1200 (Fig. 4), light south-southwesterly flow into a stationary boundary extending across southern Nebraska helped keep higher dew point temperatures over the plains states. Winds along the foothills of the Rocky Mountains and westward were light and variable.

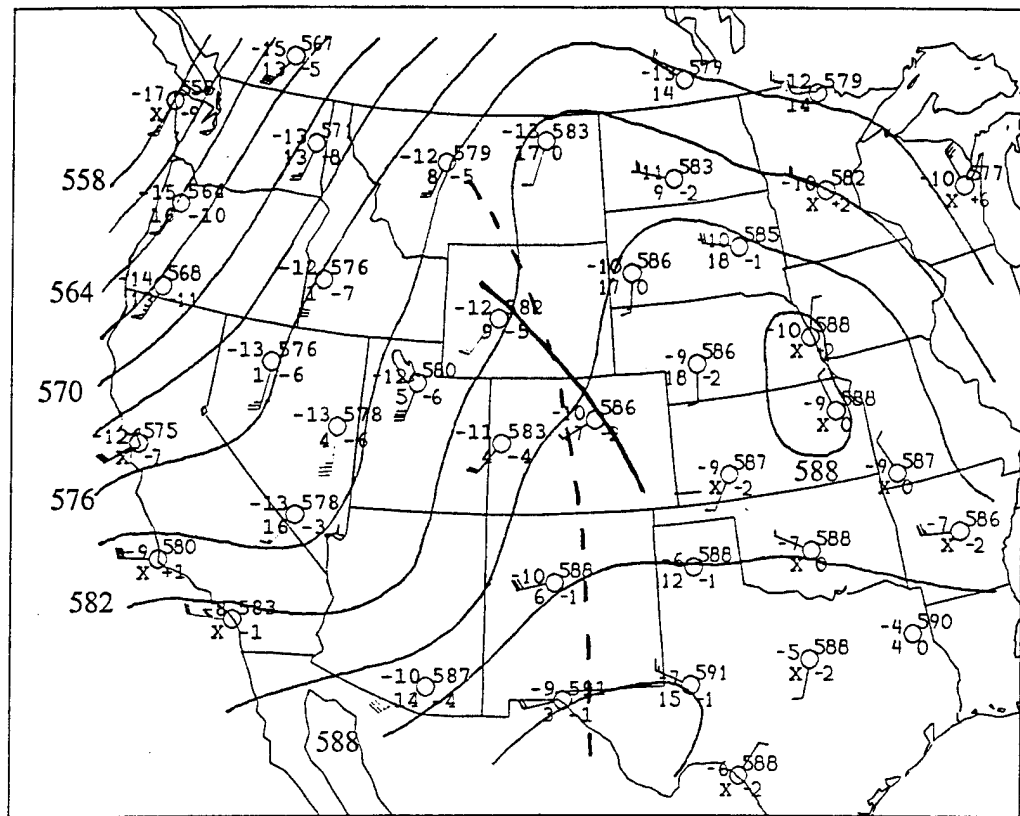


FIG. 3. Upper air analysis for 1200 UTC 21 June 1993 at 500 hPa. Plotted station parameters include temperature (deg C), dew point depression (deg C), geopotential height (decameters), and 12 h height changes. Geopotential heights (solid) are contoured every 30 m. Trough position is indicated by the thick solid line and the 1200 UTC 21 June 1993 700 hPa thermal ridge is indicated by the thick dashed line.

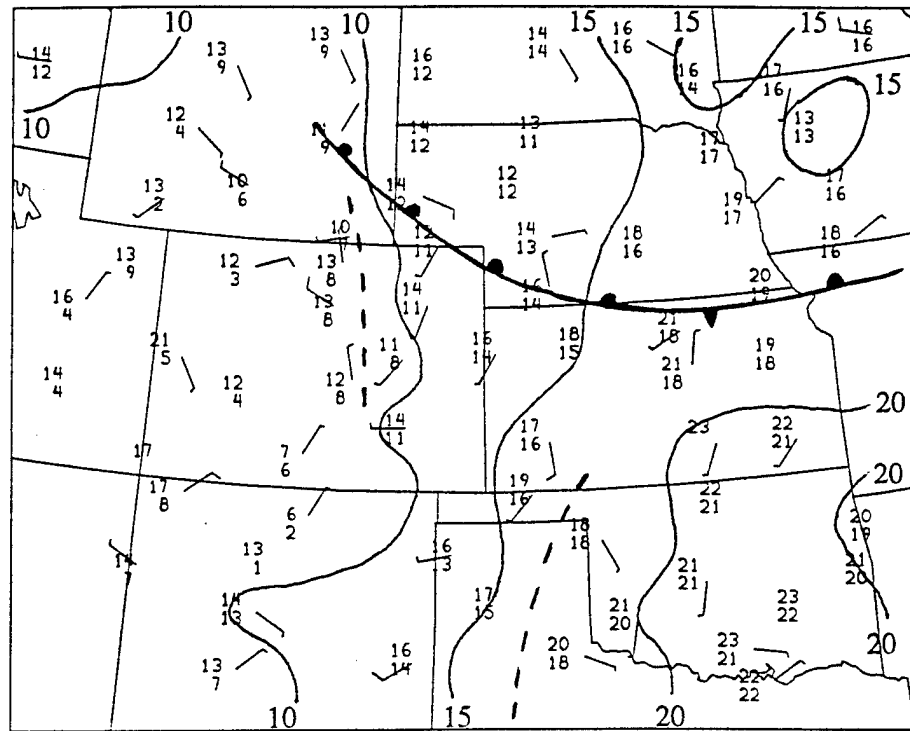


FIG. 4. Synoptic surface conditions for 1200 UTC 21 June 1993. Plotted station parameters include temperature (deg C) and dew point (deg C). Isodrosotherms (solid) are contoured every 5 deg C.

Comparing the Denver 1200 and a CLASS sounding released at 1700 revealed change to the vertical structure of the environment (Fig. 5). The layer below 450 hPa destabilized. The lower to middle troposphere was generally warmer and the averaged mixing ratio in the lowest 50 hPa increased slightly from 7.1 to 7.5 g kg⁻¹ while overall, the lower troposphere dried. A surface-based layer of east-southeast flow deepened to the 700 hPa level. Additionally, the vertical wind shear was generally weak to 350 hPa but increased above this level.

By 1800, surface conditions showed increased winds over the plains from the southeast with the surface front in Fig. 4 now located over southeast Nebraska into Missouri. (Fig. 6). Easterly to southerly winds over the High Plains are often associated with advecting humid maritime air into the region and increasing the potential for severe weather (Doswell 1980). Dew points in Northeast Colorado rose 4.5 °C during the last 6 hours.

Using prevalent surface conditions just prior to MCS initiation at 1930, the 1700 sounding was modified (Fig 7). The lowest layers were warmed dry adiabatically using the surface temperature. Dew points in the lower 50 hPa were increased by 1.1 °C which was the increase observed in the surface dew point since the time of the sounding. The surface based LCL and LFC were 2.4 km and 3.1 km AGL

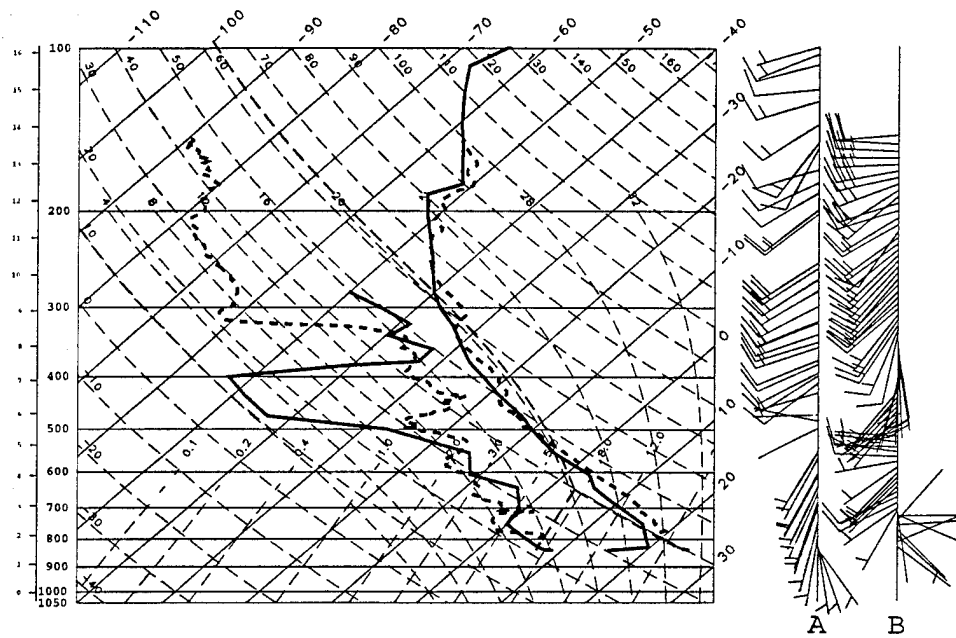


FIG. 5. The Denver skew T-log P sounding (solid) for 1200 UTC 21 June 1993 and associated winds (m/s) on the wind profile labeled A. The CLASS sounding (short dashed) for 1700 UTC and associated winds on the wind profile labeled B. Parcel ascent (long dashed) based on average conditions near the surface for the CLASS sounding.

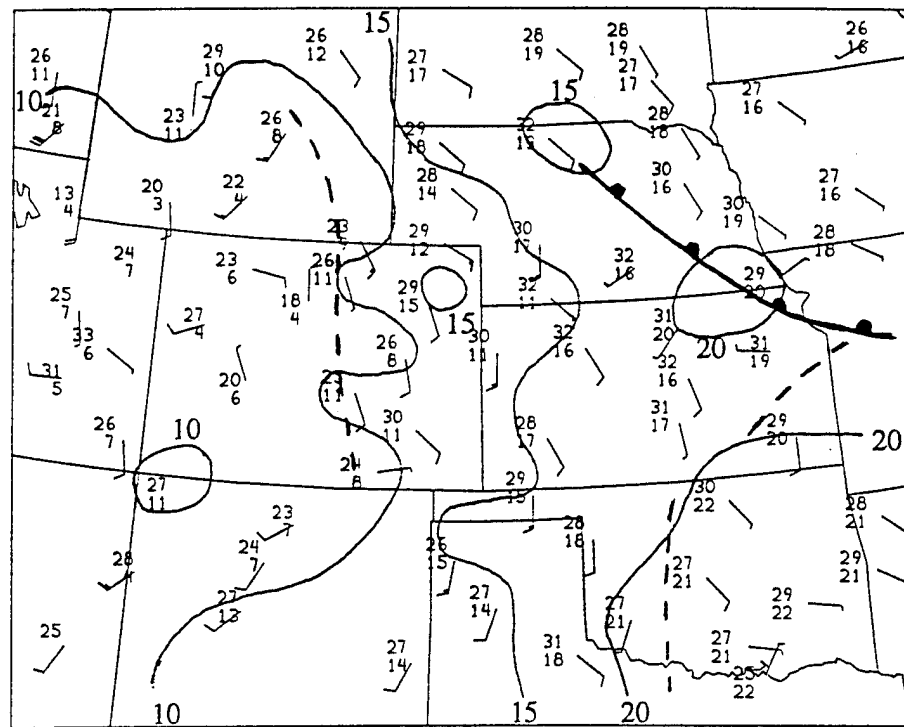


FIG. 6. As in Fig. 4 except for 1800 UTC 21 June 1993.

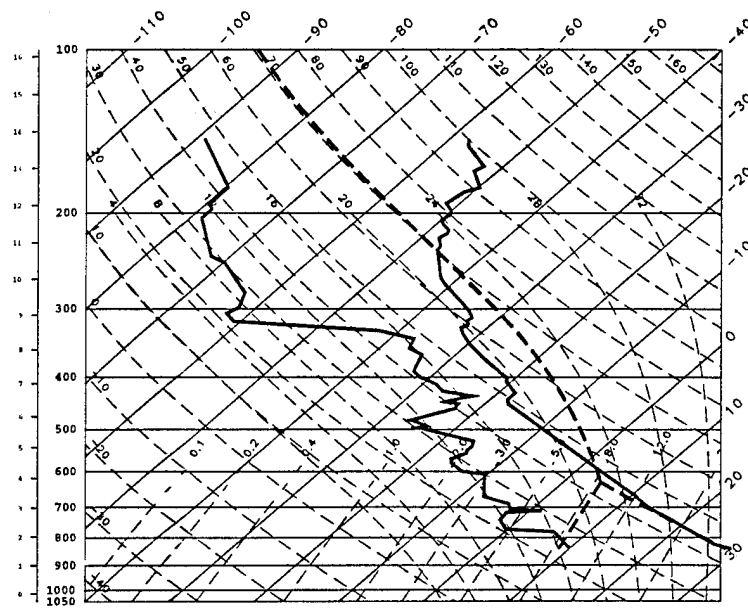


FIG. 7. The 1700 UTC 21 June 1993 CLASS sounding (see Fig. 5) modified with 1930 UTC surface observations. Parcel ascent based on average conditions near the surface.

respectively. The amount of negative buoyancy below the LFC was 54 J kg^{-1} . CAPE increased to 1149 J kg^{-1} and the Bulk Richardson Number (BRN), calculated using the same procedures as in Weisman and Klemp (1982), was 127. Weisman and Klemp (1982) found BRNs greater than 30 favored multicell storms.

3.2. Radar and Satellite Overview

The convection that was associated with the squall line under investigation here, occurred in three discrete cycles. A cycle is defined as a distinct line of convective cells that initiate, intensify, then decay. Cycle 1 initiated over the Front Range of the Colorado Rocky Mountains, cycle 2 initiated along the foothills of the mountains, and cycle 3 initiated about 100 km east of the Front Range, just outside of the surface mesonet.

Cycle 1's convection over the Front Range began at 1720 (1120 Mountain Standard Time (MST)). Convection between 1000-1300 MST along the Front Range is common during the summer months (Karr and Wooten 1976, Cotton et al. 1982, Klitch et al. 1985). This convection is typically driven by convergence at ridge-top from upslope flow induced by differential surface heating (Tripoli and Cotton 1989). Convection over the mountains and Front Range on 21 June

1993 was widespread and was aided by the passing short-wave trough. This convection laid down a gust front that created strong surface convergence and initiated the squall line of interest in cycle 2 at 1945. The enhanced IR satellite picture at 2000 showed the convective activity over the mountains and foothills with the beginning of the squall line in Fig. 8a. The MCS rapidly grew in the following 2 hours (Figs. 8b,c) moving in an east-northeast direction while developing new convective cells along the northern end of the MCS. By 2300, the MCS merged with the convection along the western border of Nebraska (Fig. 8d).

The MCS of interest was a subset of a larger system of MCS's oriented northwest to southeast along the Rocky Mountains (Fig. 9a). This larger system began along the front range of the Wyoming and Colorado Rocky Mountains and was associated with the east-northeast moving short-wave trough in Fig. 3. Convection of varying intensities was predominantly linearly organized and moved from Nebraska to Minnesota, lasting through 0800, 23 June (Fig. 9b-f).

Horizontal cross-sections of radar reflectivities from the MHR of cycle 2 and 3, revealed in greater detail the squall line's formation, intensification, and initial stages of maturity. At 2000, 20 minutes after initiation, four new reflectivity cells labelled A through D had developed east of the original activity over the mountains (Fig. 10a).

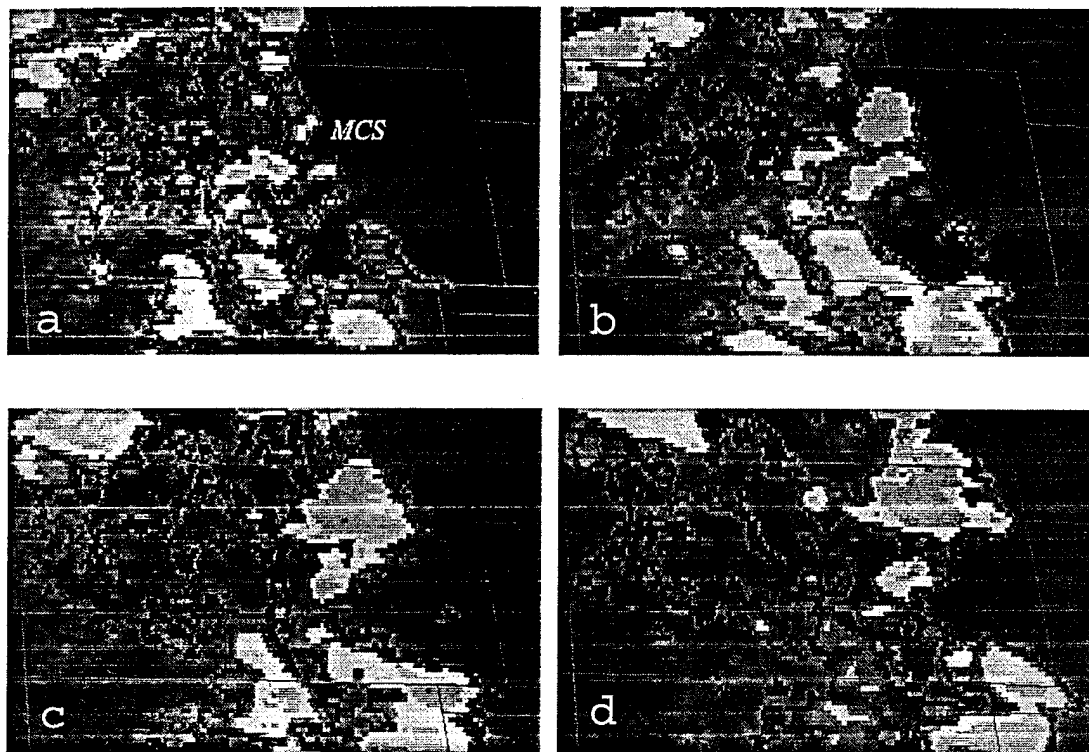


FIG. 8. Enhanced infrared GOES satellite images showing the intensification of the MCS: (a) 2000 UTC, 21 June 1993, (b) 2100 UTC, (c) 2200 UTC, and (d) 2300 UTC. The cells to the immediate left of the MCS labelling in (a) are the beginnings of the squall line of interest. The stepped shades of dark grey, light grey, grey, and medium grey are the thresholds for areas with apparent blackbody temperatures that become progressively colder.

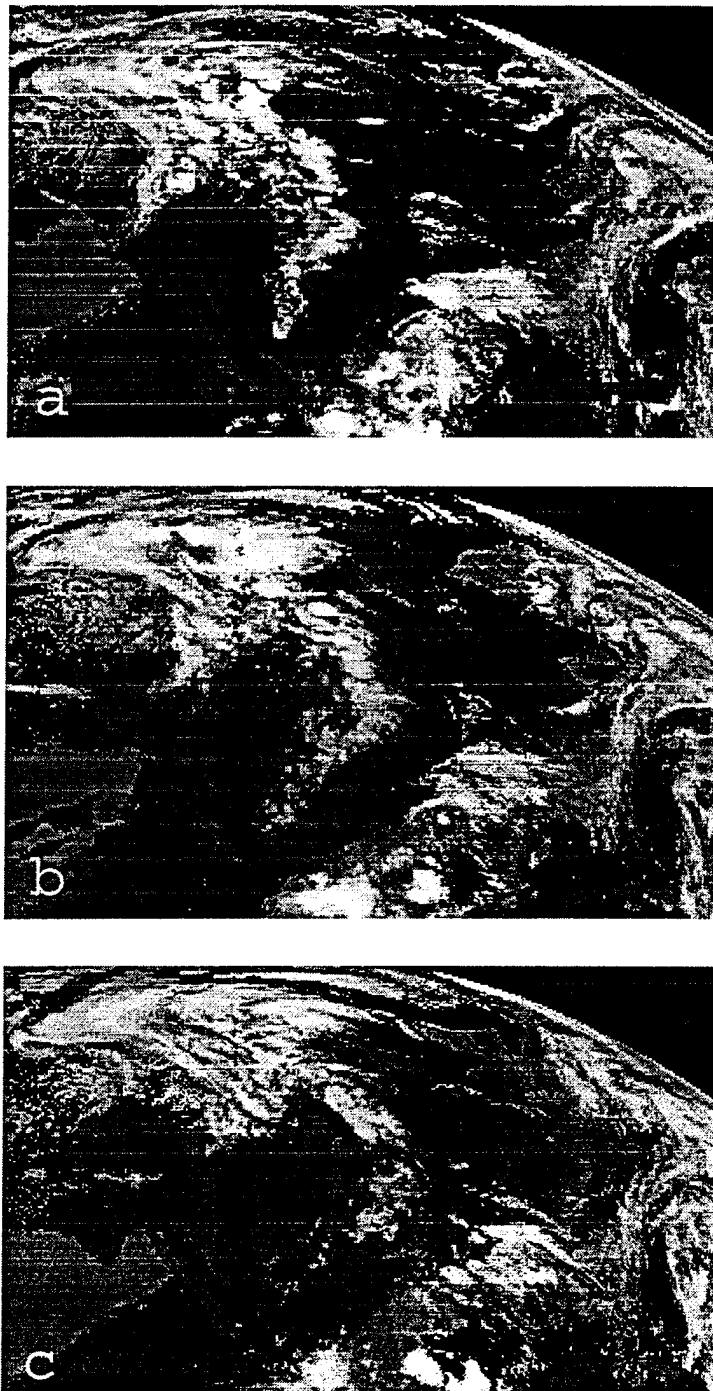


FIG. 9a-c. Enhanced infrared GOES satellite images showing the breadth and longevity of the MCS: (a) 0000 UTC, 22 June 1993, (b) 0600 UTC, and (c) 1200 UTC. The brightest whites are the coldest apparent blackbody temperatures.

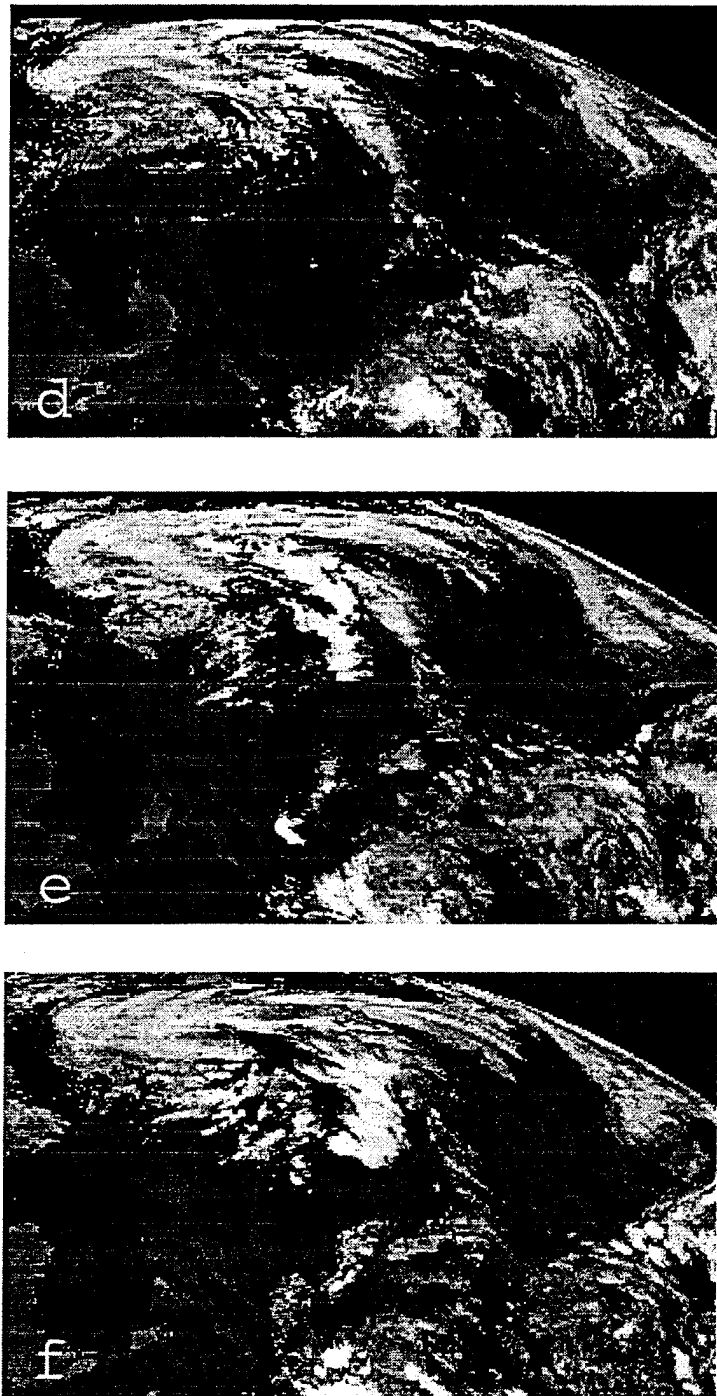


FIG. 9d-f. As in Fig 10a-c except d) 1800 UTC, 22 June 1993, (e) 0000 UTC, 23 June 1993, and (f) 0600 UTC.

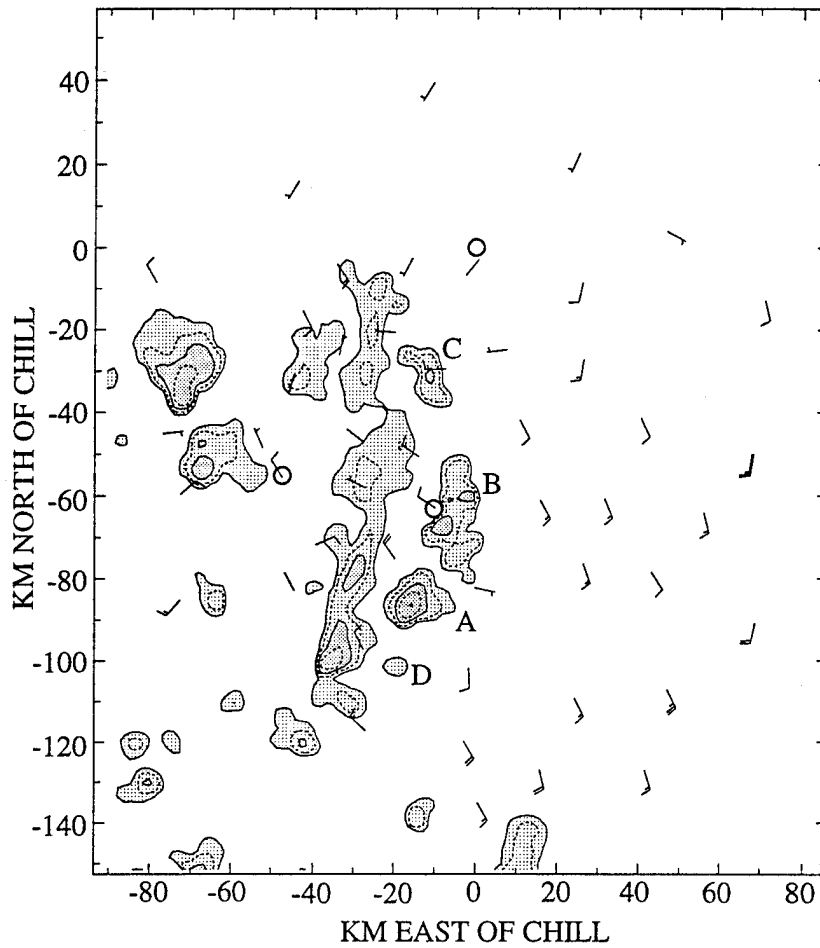


FIG. 10a. Horizontal MHR reflectivity cross section at 3.0 km for 1957 UTC. Contour intervals are in 7.5 dBZ increments beginning with 15 dBZ. Shading intervals are 15, 30, and 45 dBZ. Surface winds (full barb = 5 m/s) for 2000 UTC from the PROFS/PAM mesonet. Circles identify the three Doppler radars. Reflectivity cells labelled A, B, C, and D are discussed in the text.

Cell labelling was done alphabetically with the oldest cell being A and the newest labelled D. The linearly oriented individual cells are considered the formative stage of the squall line (Leary and Houze 1979) and the initiation of cycle 2. The reflectivities to the west of the labelled cells was the convection from cycle 1 that laid down the outflow boundary that initiated cycle 2's convection.

Within one hour (Fig. 10b,c), the individual convective cells merged into a convective line approximately 100 km in length. Using the Bluestein and Jain (1985) categorization scheme for squall line formation, this squall line exhibited broken line formation. In their study of severe squall lines that formed within the Norman, Oklahoma WSR-57 radar domain, 35% of their working sample of 40 formed from a broken line situation. At this point, the convective line fit Houze's definition for an MCS of "a contiguous precipitation area approximately 100 km or more in horizontal scale in at least one direction" (Houze 1993). Also at this time, the mesoscale convective system was categorized as being in the intensification stage (Leary and Houze 1979). The southern half of the squall line was more homogeneous along its length, while the northern half was more cellular with the northern most cell exhibiting strongest reflectivities. Along the leading edge of the squall line at $y=-35$, -60 and -80 were the beginnings of

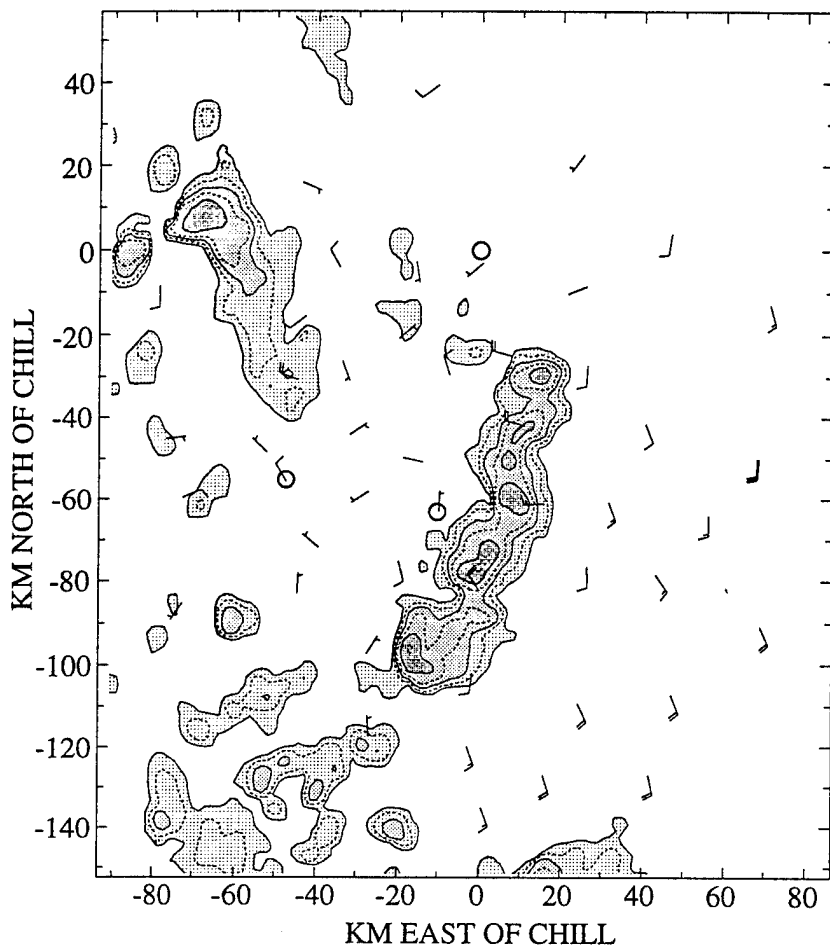


FIG. 10b. As in Fig. 10a except MHR radar reflectivities for 2033 UTC and PROFS/PAM mesonet winds for 2030 UTC.

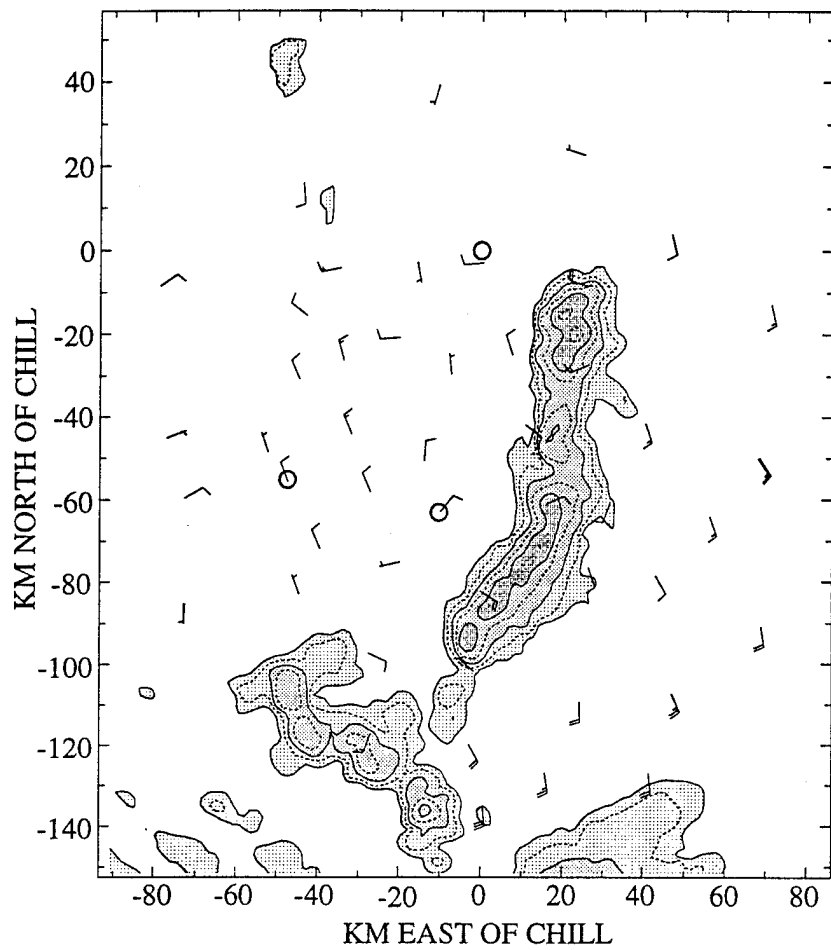


FIG. 10c. As in Fig. 10a except MHR radar reflectivities for 2103 UTC and PROFS/PAM mesonet winds for 2100 UTC.

three small cells. The growth of these new cells was suppressed as they did not develop much beyond what is shown. To the southwest of MHR, new convection formed along the Palmer Divide.

At 2130, Fig. 10d revealed a lengthening of the MCS to 120 km. The southern end of the squall line merged with the convection south-southwest of MHR. The three cells located ahead of the main convective line seen in Fig. 10c were again apparent along the leading edge of the squall line at $y=-35, -60$, and -70 with a new, stronger cell located at $y=5$. As in Fig. 10c, the northern end of line showed the largest reflectivities.

Over the next one and a half hours, cycle 2 shifted into a mature stage as new convection developed ahead of the squall line and the older convection became more stratiform in nature. Fig. 10e shows the line of new convective cells oriented approximately 30° off the northern end of the original line (note the change in scale of the figure). These new cells began the formative stage of cycle 3. The new line continued to grow and expand southward through new development that formed discretely ahead of the southern portion of the original squall line in cycle 2 (Fig. 10f,g). While the newer cycle 3 convection grew, the older convection from cycle 2 became more stratiform in nature, eventually setting up a precipitation area 60 km in width.

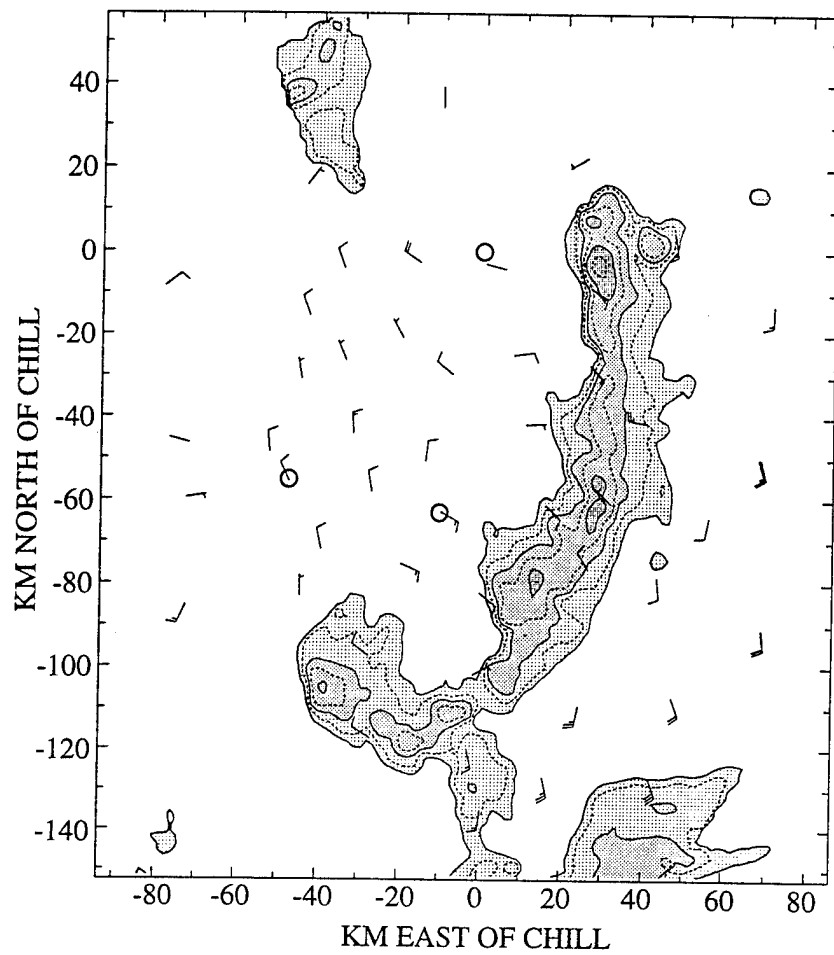


FIG. 10d. As in Fig. 10a except MHR radar reflectivities for 2127 UTC and PROFS/PAM mesonet winds for 2130 UTC.

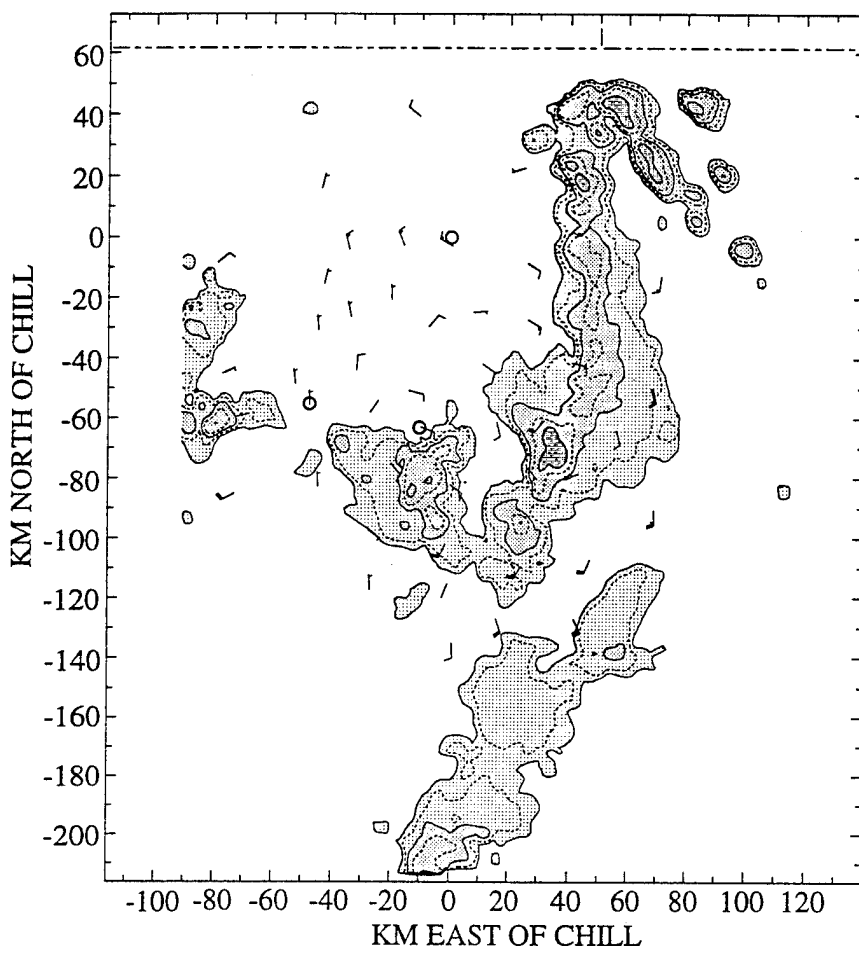


FIG. 10e. As in Fig. 10a except MHR radar reflectivities for 2203 UTC and PROFS/PAM mesonet winds for 2200 UTC.

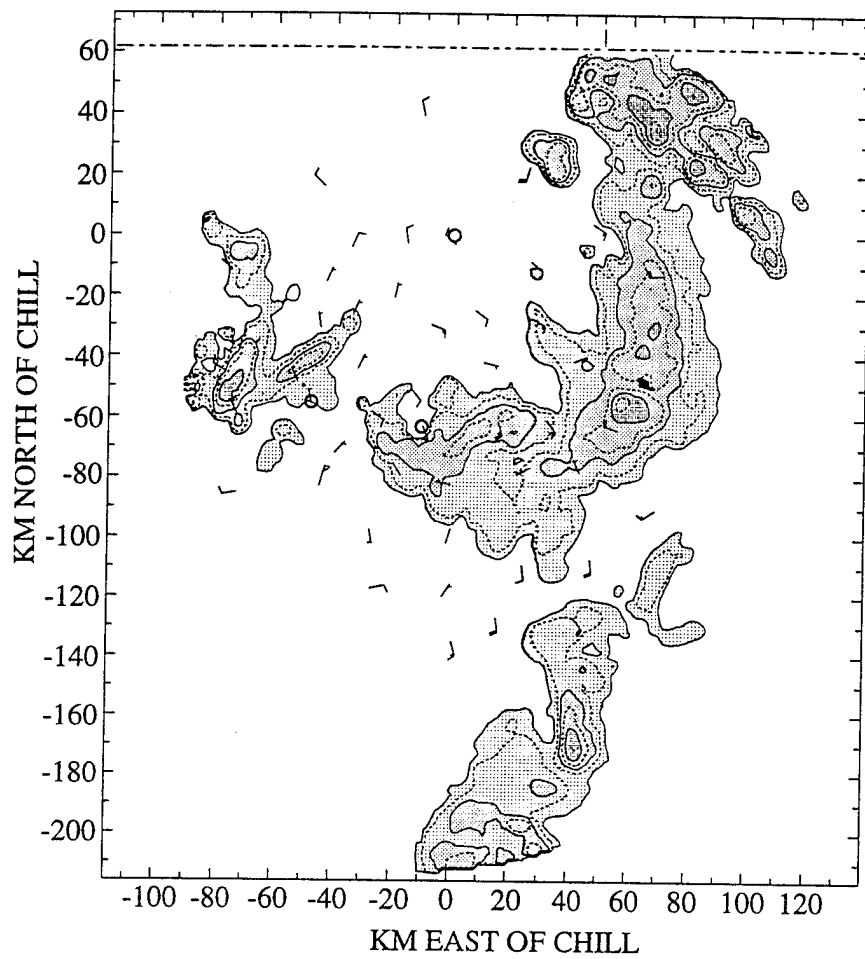


FIG. 10f. As in Fig. 10a except MHR radar reflectivities for 2233 UTC and PROFS/PAM mesonet winds for 2230 UTC.

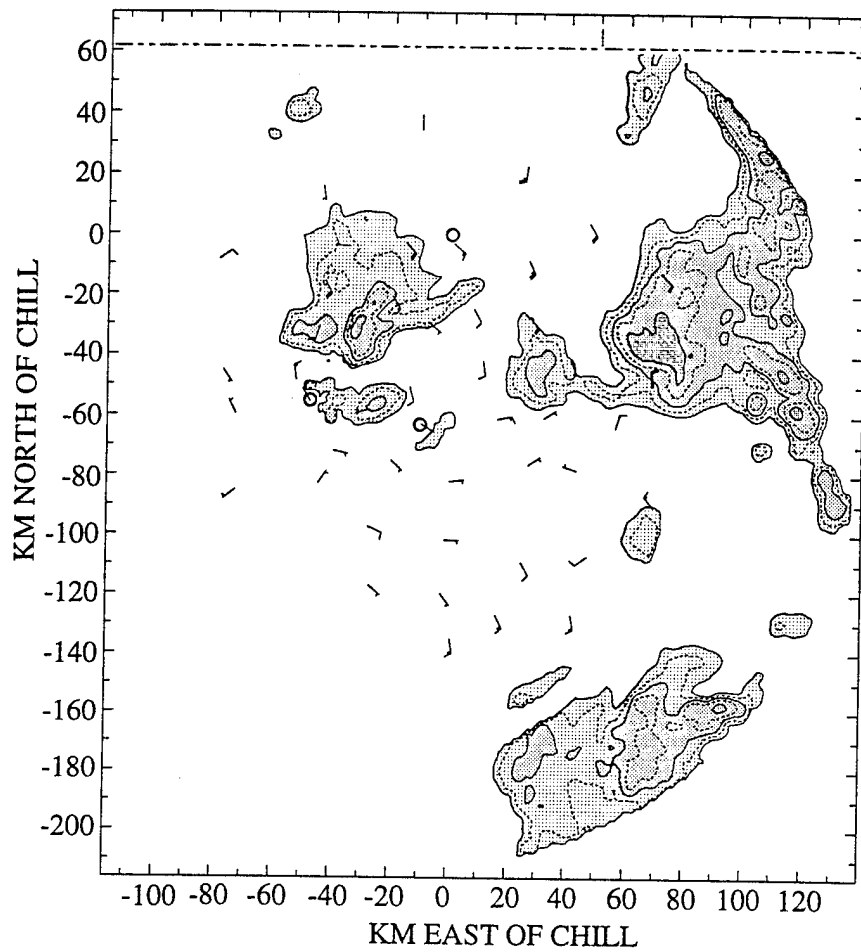


FIG. 10g. As in Fig. 10a except MHR radar reflectivities for 2335 UTC and PROFS/PAM mesonet winds for 2330 UTC.

normal to the line in Fig. 10g. Off the southern end of the squall line, the convection that was noted in Fig. 10c continued to develop and eventually merged with the stratiform region of the original convective line.

3.3. Surface Reflection of the Squall Line

A time series of the surface data for PAM station #10 (see Fig. 2 for location) is presented in Fig. 11. During passage of the squall line at the PAM station, the MCS was in its mature stage as cycle 3's convection began ahead of the line. The time series was very representative of a squall line passage (Maddox 1980) with two exceptions. First was the relatively short duration of the pressure rise and fall. Maddox noted an approximate 2 hour pressure rise with nearly continual precipitation during the period. The 45 minute pressure dome in this case was explained by the squall line being only 2 hours and 45 minutes old and not having developed an extensive meso-high yet. The second exception was the lack of heavy precipitation falling just after the gust frontal passage. This lack of heavier precipitation could be accounted for by the discrete nature of propagation noted in this case as the main convective line formed ahead of the station and did not traverse it. The measured precipitation was from cycle 2 as the

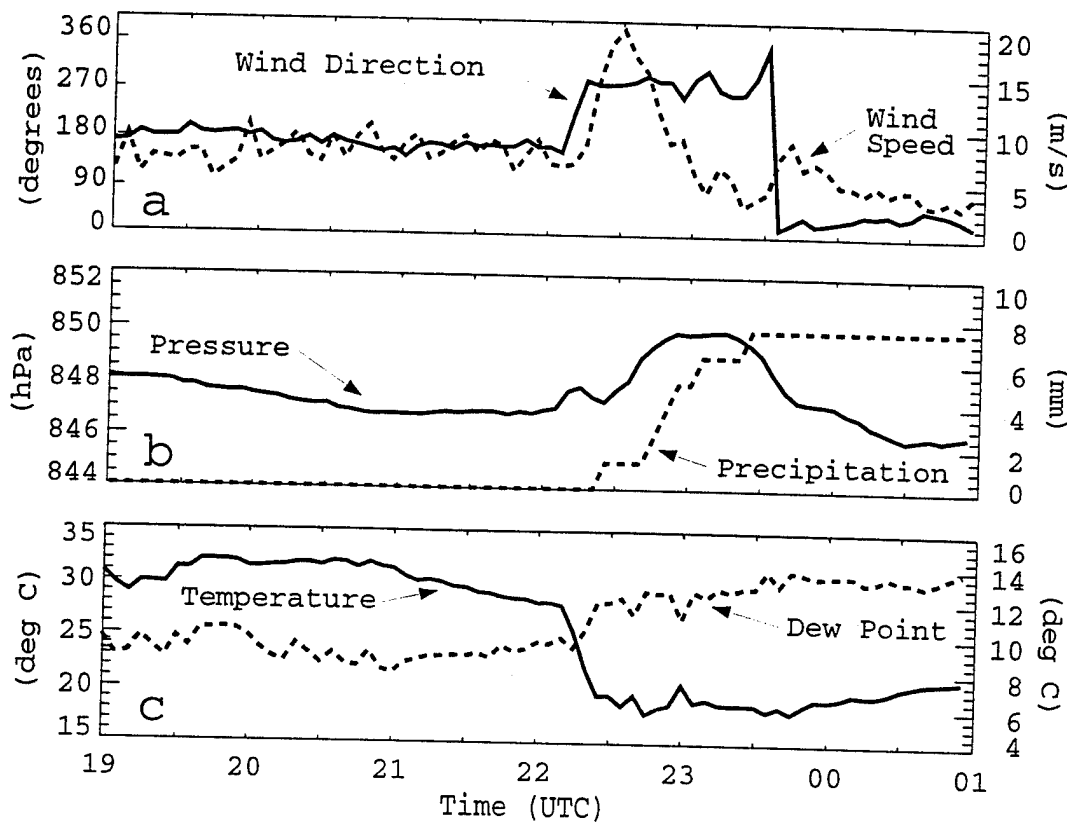


FIG. 11. Time series plot of PAM station 10 data from 1900 UTC on 21 June 1993 until 0100 UTC on 22 June 1993. Data values are 5 minute averages. (a) Wind direction (degrees from true north, solid) and wind speed (m/s, dashed). (b) Station pressure adjusted to 1500 m (hPa, solid) and 5 minute accumulated precipitation (mm, dashed). (c) Temperature (deg C, solid) and dew point temperature (deg C, dashed).

convection was moving from a convective to stratiform type. The precipitation was moderate and sporadic with the largest duration occurring from the older, dying convective line.

Other observations noted during squall line passage were more normal in nature. Observed was a sharp temperature fall preceded by a gradual temperature fall. The gradual drop was caused by reduced solar IR radiation from a predominant leading anvil. The distinct temperature fall was accompanied with increased moisture from evaporation of precipitation in the downdraft air and a sharp pressure rise. A sharp wind shift and strong gusty winds clearly identified the gust front passage and another wind shift and weaker gusty winds were seen from the outflow on the back side of the squall line. Not surprisingly, time series at other mesonet sites west of station #10 showed a similar squall line passage but with less amplitude in the surface changes as the squall line was still in its formative and intensifying stages.

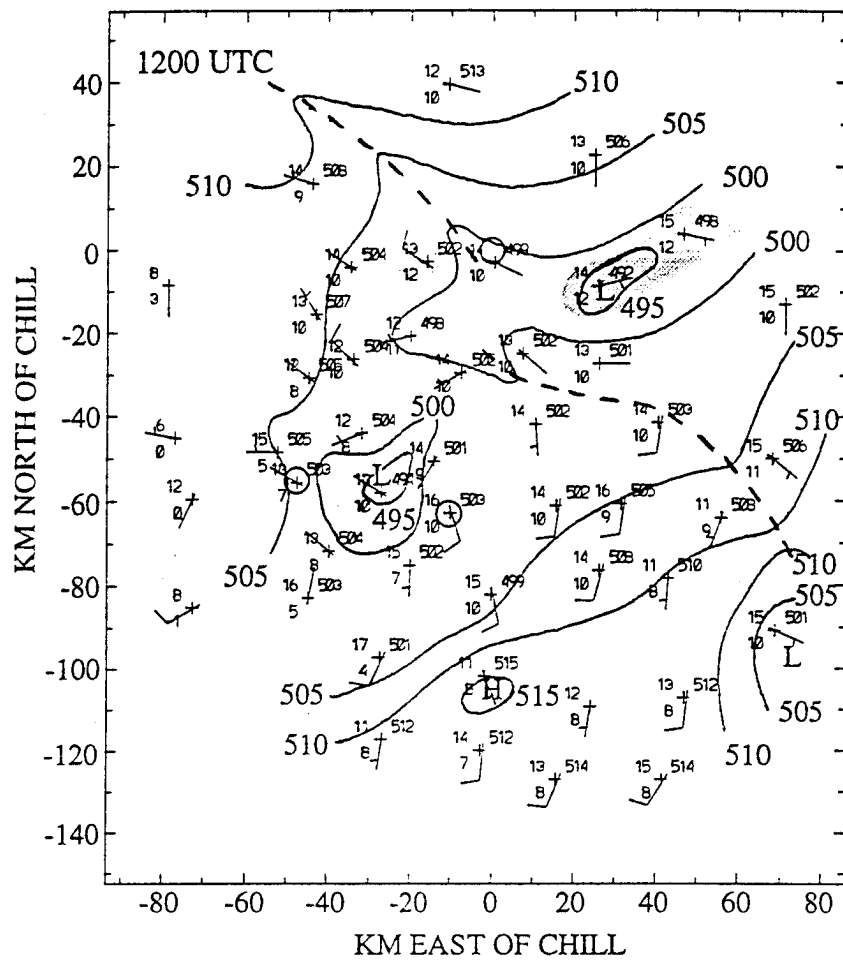


FIG. 12a. Mesonet surface analysis for 1200 UTC 21 June 1993. Plotted station parameters include temperature (deg C), dew point (deg C), corrected station pressure adjusted to 1500 m (hPa) multiplied by 10 with the leading 8 dropped), and the wind barbs (full barb = 5 m/s). Station pressure is contoured at 0.5 hPa intervals. Areas where dew points are greater than 12 deg C are lightly shaded. Circles identify the location of the three Doppler radars.

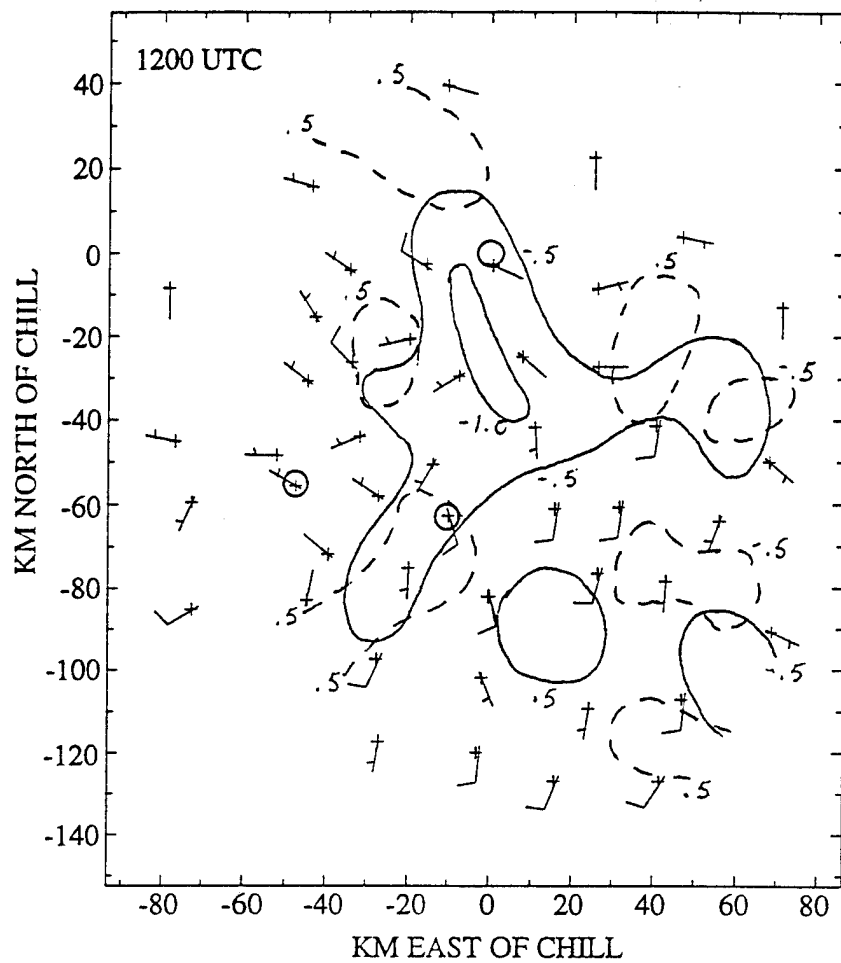


FIG. 12b. Mesonet surface kinematic analysis for 1200 UTC 21 June 1993. Mesonet winds plotted (full barb = 5 m/s). Vertical vorticity (dashed) and divergence (solid) are contoured at 0.5 times 10^{-4} /s intervals.

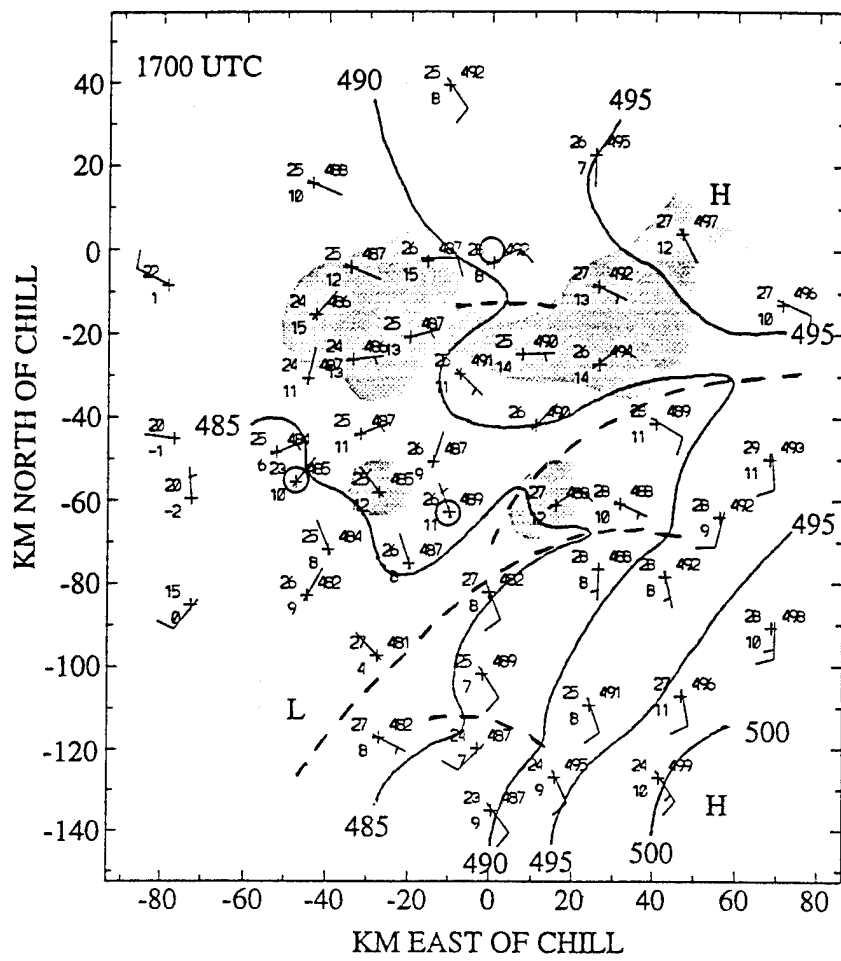


FIG. 13a. As in Fig. 12a except for 1700 UTC 21 June 1993.

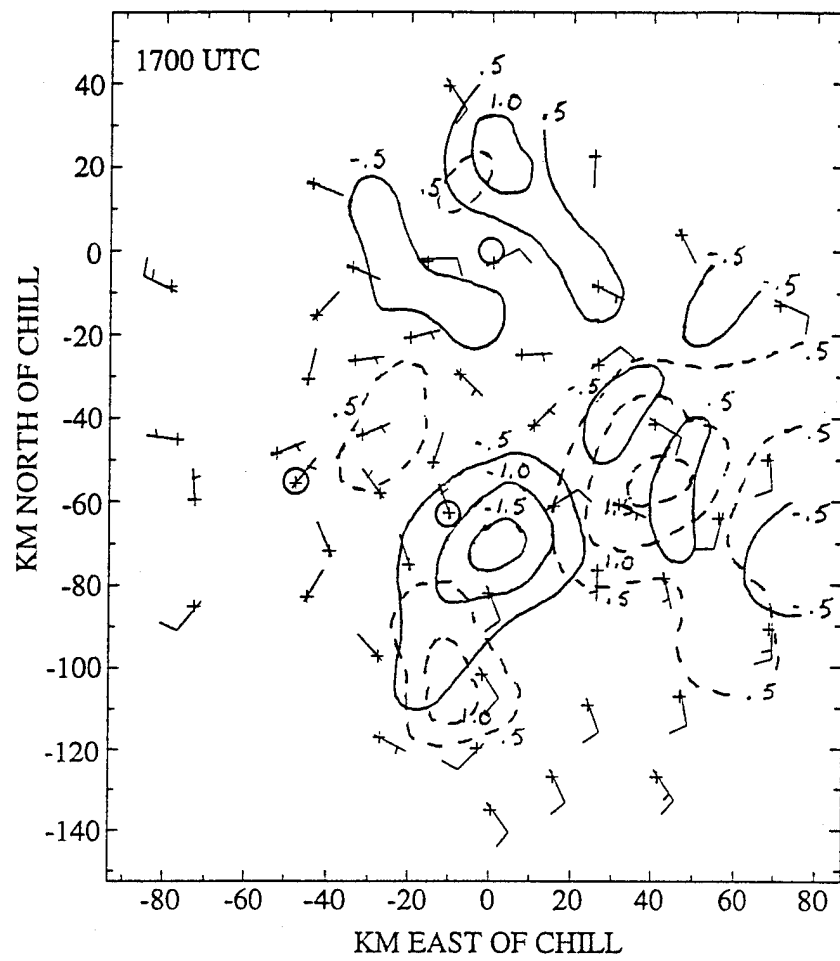


FIG. 13b. As in Fig. 12b except for 1700 UTC 21 June 1993.

The strengthened cyclonic circulation (Fig. 13b) advected moister air into the mesonet area from the plains of eastern Colorado. Fig. 14 shows a time series of 12 °C dew point isopleths advancing into the mesonet. The cyclonic circulation, commonly called the Denver Cyclone, is associated with surface convergence and cyclonic vorticity. This feature is well-documented and often associated with severe weather (Szoke et al. 1984, Blanchard and Howard 1986, Brady and Szoke 1989) and the Denver cyclone is generally accepted as being orographically induced (Wilczak and Glendening 1988).

The 1800 meso-analysis in Fig. 15 shows a changed Denver cyclone. Surface temperatures predominantly warmed to greater 27 °C, and the surface inversion was eliminated. Though a small area of cyclonic circulation remained, the surface winds became predominately south-southeasterly and responded more to the synoptic pressure pattern than to the topography. Because of the elimination of the inversion, mixing took place through a greater depth and the moister air mass that advected down into the Denver metropolitan area started retreating northward. A large area of higher surface dew points remained, hemmed in by the Colorado Rockies and the Cheyenne Ridge.

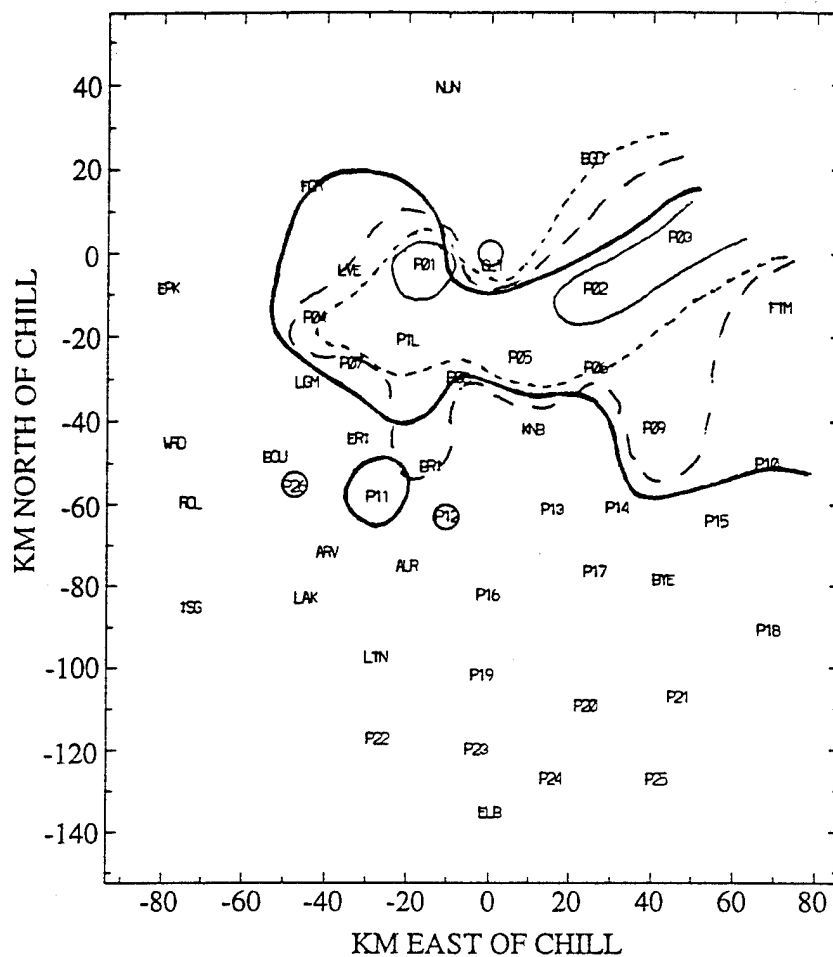


FIG. 14. Time series of the 12 deg C isodrosotherm for 1200 UTC (solid), 1300 UTC (short dashed), 1400 UTC (long dashed), and 1500 UTC (thick solid) 21 June 1993. Circles identify the location of the three Doppler radars and the alpha-numeric identifiers mark the location of the PROFS and PAM surface stations.

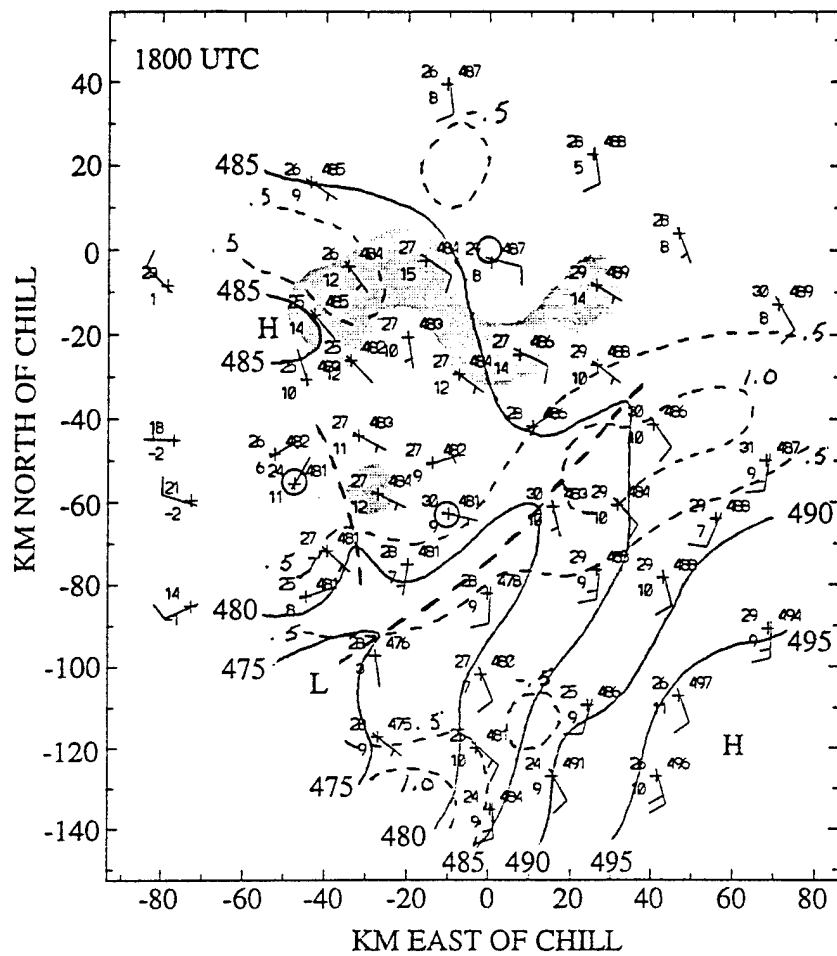


FIG. 15. Mesonet surface analysis for 1800 UTC 21 June 1993. Same plotting convention as in Fig. 13a. Station pressure is contoured at 0.5 hPa intervals (solid). Areas where dew points are greater than 12 deg C are lightly shaded. Vertical vorticity is contoured at 0.5 times 10^{-4} /s.

4.2. MCS Initiation

Weak, low-level convergence present from the Denver cyclonic flow in Fig. 15, would have created upward vertical motion through mass continuity. Since no convection was present at that time over the foothills, this suggests that the forced upward motion was not strong enough to penetrate the negatively buoyant air below the LFC (see Fig. 7). The trigger for the MCS initiation and the beginning of cycle 2 was the gust front from cycle 1's convection. Cycle 2 convection began in earnest at 1720. The fine-line reflectivity pattern associated with the gust front became evident in the MHR reflectivity data at 1915. From the reflectivity data at 1937, the gust front was observed to be about 110 km long. At this time, the gust front passed over the MHR, the Stapleton wind profiler and accompanying RASS. Combining these multiple observing platforms with a time series from a mesonet station, a vertical and horizontal picture of the gust front is shown in Fig. 16.

At the PAM mesonet station 12, a typical gust front and associated cold pool signature was reflected (Fig. 16a). Surface conditions associated with a passing gust front were identified in a detailed temporal sense by Charba (1974). Though the 5 minute averaged mesonet observations were not detailed enough to resolve all of Charba's temporal

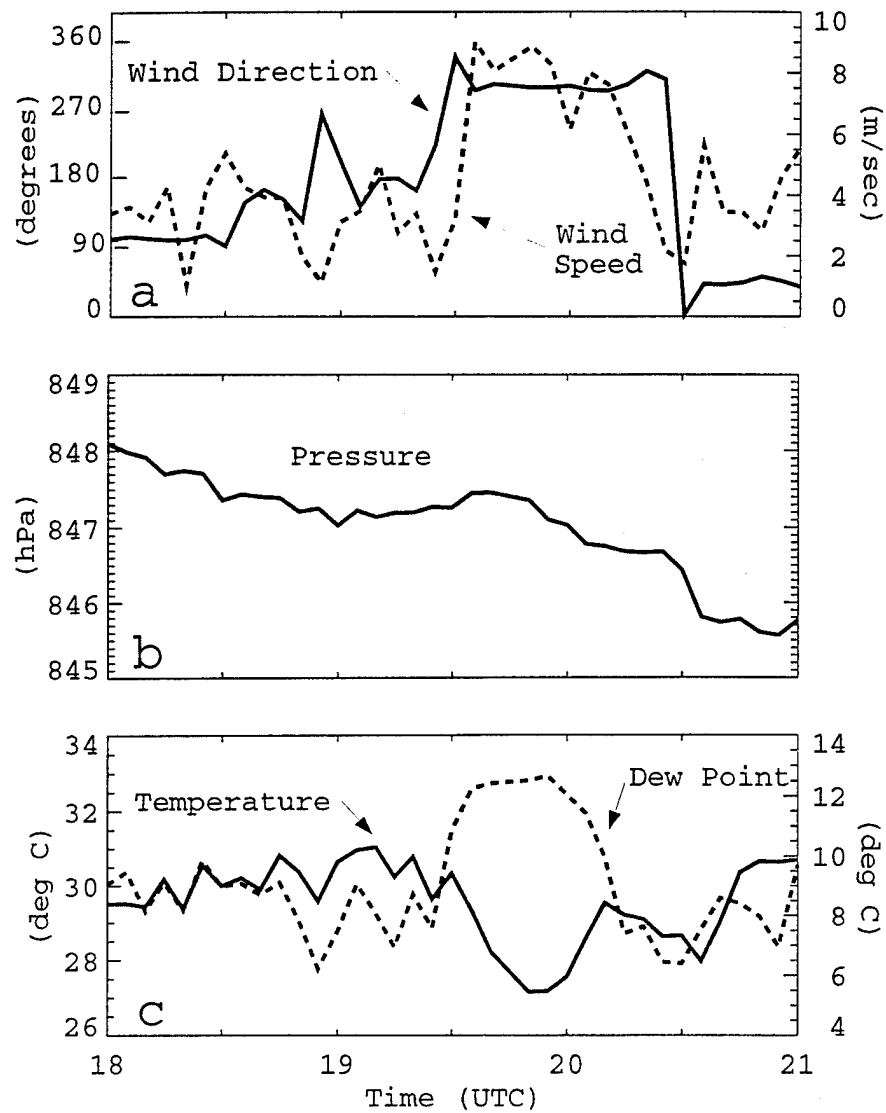


FIG. 16a. Time series plot of PAM station 12 data from 1800 to 2100 UTC on 21 June 1993. Data values are 5 minute averages. (a) Wind direction (degrees from true north, solid) and wind speed (m/s, dashed). (b) Station pressure adjusted to 1500 m (hPa, solid). (c) Temperature (deg C, solid) and dew point temperature (deg C, dashed).

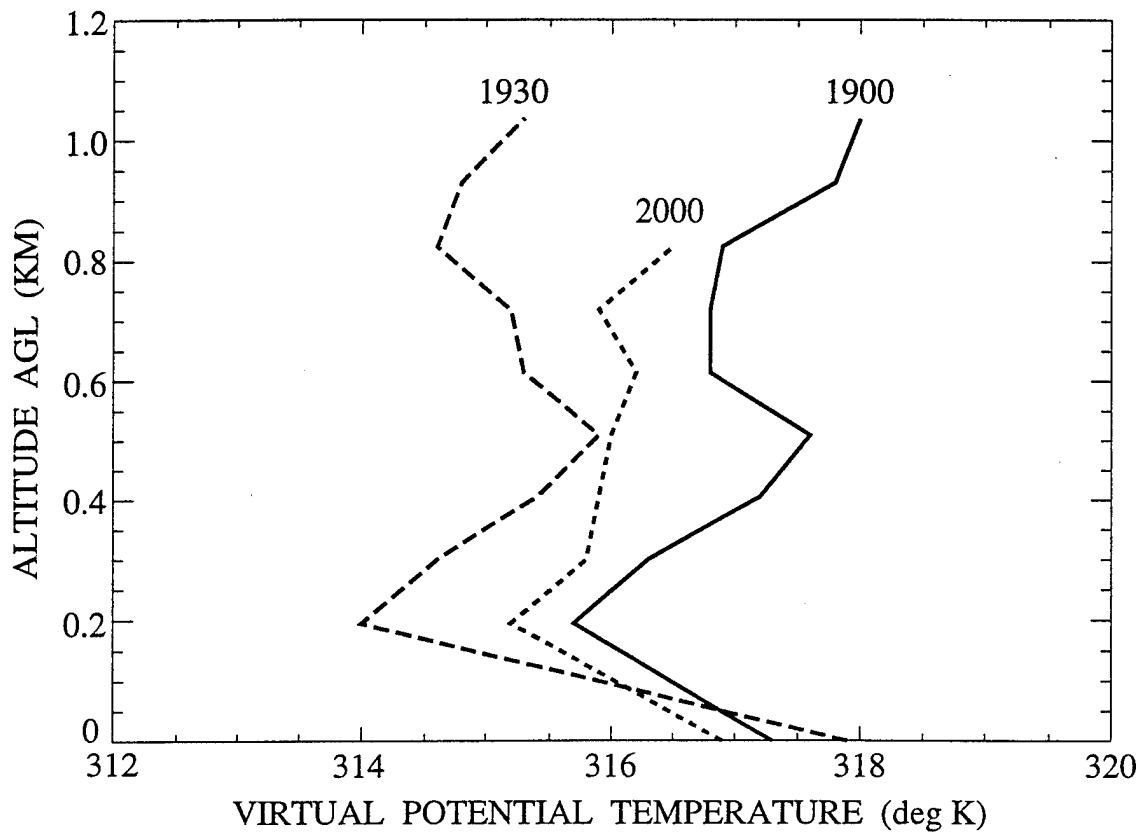


FIG. 16b. Vertical time series plot of virtual potential temperature (deg K) calculated from the Denver RASS at 1900, 1930, and 2000 UTC on 21 June 1993.

assertions, the observations qualitatively agreed well. Exhibited with the gust front passage were the trademark gusty surface winds from the direction of convective activity. Additionally, the surface pressure rose, dew point increased and temperature decreased from the evaporatively cooled downdrafts created by the convection. By 2000, temperature and pressure quickly rebounded indicating a short horizontal distance normal to the gust front and associated cold pool. The gust front moved at 6 m s^{-1} to the east/southeast and was observed to create a misocyclone (Fujita 1981) about 10 km east of MHR at 1955 (Crook and Hobson 1994).

Aloft, the RASS afforded a vertical picture of the cold pool. A series of three virtual potential temperature (θ_v) profiles were calculated from the RASS virtual temperatures and are shown in Fig. 16b. These three profiles represent the boundary layer just before, during, and after the gust front passage. A 200 m deep surface layer exhibited a continual super-adiabatic lapse rate. Above this surface layer, an 800 m well-mixed layer dropped approximately $2 \text{ }^\circ\text{K}$ upon gust frontal passage. This $2 \text{ }^\circ\text{K}$ perturbation was a little low as compared to the gust fronts observed by Goff (1974) which exhibited averaged mean perturbations between $2.4-6.1 \text{ }^\circ\text{K}$. The environment quickly rebounded to a near pre-gust frontal temperature within 30 minutes.

One of the two components of the RKW conceptual model is the strength of the cold pool. Though the RKW simulations created the cold pool from the squall line itself, convection from cycle 2 in this case was initiated upon a pre-existing cold pool. RKW calculated the cold pool strength (c) to be

$$c^2 = 2 \int_0^H (-B) dz \quad (1)$$

where the buoyancy (B) is defined to be

$$B = g \left(\frac{\theta'}{\theta} + 0.61 (q_v - \bar{q}_v) - q_c - q_r \right) \quad (2)$$

and θ is the potential temperature, g is gravity, and q_v , q_c , and q_r are the mixing ratios of water vapor, cloudwater, and rainwater, respectively. The integral is calculated through the depth of the cold pool (H) at a representative location behind the leading nose of the gust front. Since the MHR indicated no precipitation along the gust front between 1915 and 1942, and any clouds present would be over 2.0 km above the gust front (estimated from the LCL of the modified 1930 sounding), equation 1 becomes

$$c^2 = 2 \int_0^H \left(-g \frac{\theta'_v}{\theta_v} \right) dz \quad (3)$$

and is calculated directly from the RASS data. Depth of the

cold pool was determined by the MHR velocity-azimuth display (VAD) analysis (Browning and Wexler 1968) and found to be between 400-600 m. This cold pool is within the range of typical cold pool depths (Wakimoto 1982). Using the ratio $c/\Delta u$, where Δu represents the strength of the ambient low-level vertical wind shear, an optimal growth situation and upright updraft would occur when $c/\Delta u = 1$, a downshear tilted updraft would occur when $c/\Delta u < 1$, and an upshear updraft would occur when $c/\Delta u > 1$. Table 1 shows the range of values for the cold pool to wind shear ratio using a 2.5 km ambient wind shear of 8.0 m s^{-1} (determined from the 1700 CLASS sounding) observed in this case.

Table 1. Values of the ratio of cold pool strength (c) and ambient low-level wind shear (Δu). The integration of the equation for the cold pool strength was accomplished through the depth of the cold pool (H) for the times listed.

Time	H (km)	C (m/s)	C/ Δu
1938	0.6	8.4	1.05
1947	0.4	6.8	0.85

These ratios indicate the updraft tilt should show an upright to slightly downshear tilt upon convective initiation. Weisman (1992) calculated the ratio $c/\Delta u$ for a moderate shear (15 m s^{-1}) over 2.5 km and found an

approximate value of 1.4 by 60 minutes with an upshear tilt ensuing. Values of the ratio were not reported prior to the 60 minute point as the depth of the cold pool was much shallower and created a deep area of lift along the leading edge. In this case, the shallow cold pool, combined with the high LFC, resulted in convection initiating not along the leading edge, but 7-10 km behind it. The implications of this observation will be investigated further in the following two chapters as we look at how the updraft evolved.

Associated with the gust front was strong surface convergence (Fig. 17). This strong surface convergence was further enhanced by the pre-existing convergence from the surface trough shown in Fig. 15. Better resolution of the gust front and associated convergence was obtained when the gust front was located 5 km east over the MHR at approximately 1937. Using extended velocity-azimuth display (EVAD) techniques (Matejka and Srivastava 1991) on the 1933 MHR volume scan, the low-level divergence was alternatively calculated. Fig. 18a shows the surface convergence two orders of magnitude larger than the objective analysis using mesonet observations (see Fig. 17). Values in Fig. 18a were adjusted by accounting for all the convergence of the MHR radial volume occurring within the leading updraft width of the gust front. Young (1995) found that the

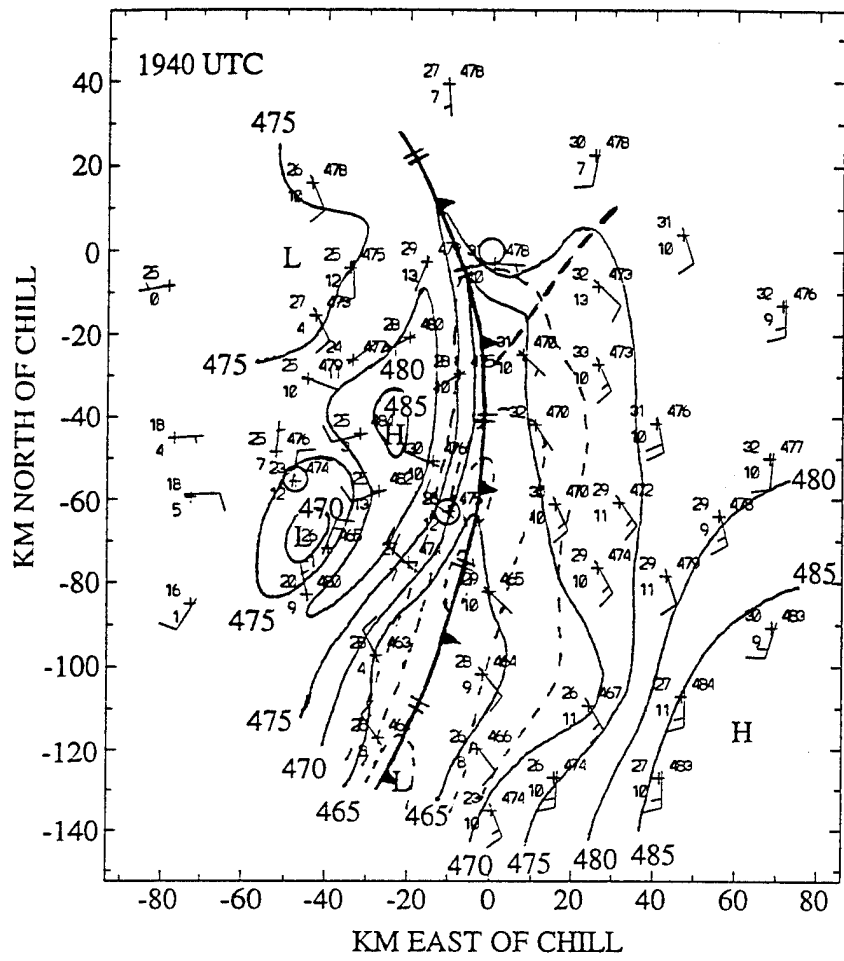


FIG. 17. Mesonet surface analysis for 1940 UTC 21 June 1993. Same plotting convention as in Fig. 12a. Station pressure is contoured at 0.5 hPa intervals (solid). Divergence is contoured at 0.5 times 10^{-4} /s intervals (dashed).

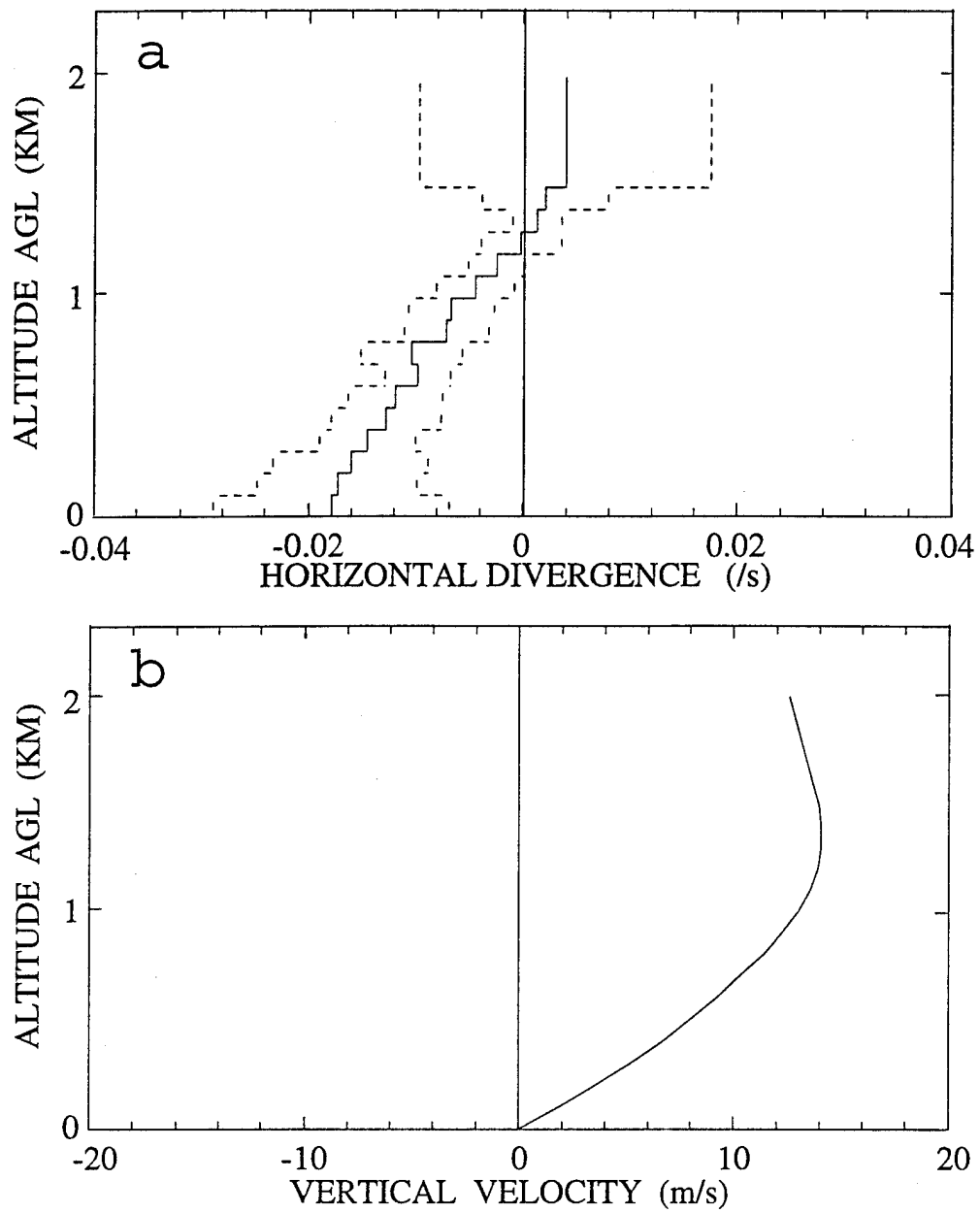


FIG. 18. EVAD vertical profiles of a) horizontal divergence (/s) and b) vertical velocities (m/s) calculated from the MHR radial velocities at 1937 UTC on 21 June 1993.

gust-frontal updraft width to be proportional to the depth of the cold pool. The continuity equation was integrated upward to yield the vertical velocity profile shown in Fig. 18b. Resultant from the gust front was 600 m of lift for the air mass encroaching upon the gust front. A conditionally unstable air mass (see Fig. 7) became even more conditionally unstable to neutral causing the convective inhibition to be eliminated. Any thermal or perturbation along the gust front now had no CIN to overcome and resulted in uninhibited ascent and convective initiation.

Chapter 5

DOPPLER RADAR ANALYSIS

A series of analyses of Doppler radar derived winds, associated kinematic fields, and surface mesonet data are presented for cycle 2 of the MCS. Of primary emphasis will be the detailed analyses at 2017 and 2102. These analyses are representative of the formative and intensifying stages of MCS growth. Within the context of the analyses, inhomogeneities along the squall line will be discussed. Horizontal cross-sections are at 3.0 km AGL with reflectivities from the Mile High Radar. Vertical time series of reflectivity and kinematic fields are shown from analyses performed at approximately 15 minute intervals starting 16 minutes after squall line formation and lasting 93 minutes into its life.

5.1. 2017 Doppler and 2015 Mesonet Analyses

In this section we look at the kinematic structure and associated surface data that is representative of the formative stage of MCS growth. The original four convective cells were still present 35 minutes after initiation (Fig. 19). The reflectivities to the west of the labelled

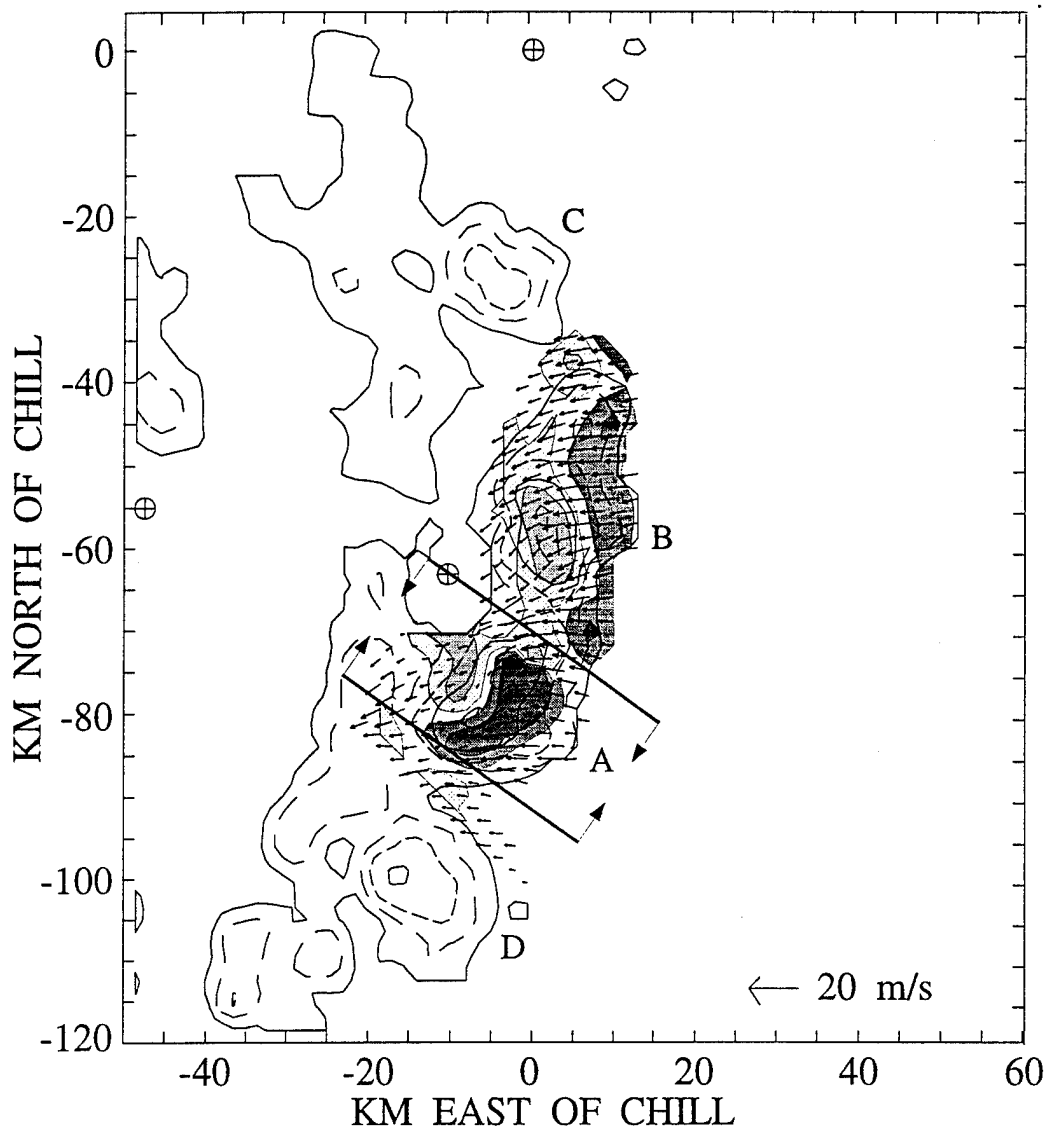


FIG. 19. Triple-Doppler analysis at 3.0 km AGL for 2017 UTC on 21 June 1993. MHR reflectivity contour intervals are in 10 dBZ increments beginning with 10 dBZ. Vectors depict line relative flow. A vector whose length equals one grid interval represents 5 m/s. Light contours enclose downdrafts; the starting contour is 0 to -2 m/s and the next contour is less than -2 m/s. Dark contours enclose updrafts; the starting contour is 2 to 4 m/s and the next contour is greater than 4 m/s. Areas not contoured below the vector field represents updrafts 0 to 2 m/s. Circles identify the three Doppler radars. Reflectivity cells labelled A, B, C, and D are discussed in the text. Heavy lines identify portion of the line used in developing vertically averaged cross-sections.

convective cells were the convection from cycle 1 that laid down the outflow boundary and initiated cycle 2's convection. An area of general upward motion was found along the leading edge of the cells with general downward motion on the trailing edge of the reflectivity cells. Imbedded within the general upward and downward couplet was an area of maximum upward motion found downshear of cell A with an associated stronger downdraft upshear. The stronger upward and downward velocity couplets were highly correlated with the stronger reflectivity cores. It is hypothesized that the stronger precipitation formed in the tilted updrafts associated with strongest upward velocities. Through precipitation loading and evaporative cooling of hydrometers, negatively buoyant air developed, causing convective-scale downdrafts correlated with convective-scale updrafts. These updraft and downdraft "couplets" are critical to storm longevity and are typically associated with supercells. The area of upward motion was initiated by surface convergence along the gust front and was enhanced by mid-level convergence apparent along the leading edge of the 40 dBZ reflectivity cores.

The updraft tilt was examined objectively using the axis of maximum vertical velocities. Connecting the centers of the maximums and minimums of the horizontal divergence field also yielded a similar orientation to the updraft.

In Fig. 20a an upshear tilted updraft in the lowest 4 km was contrasted to a nearly upright mid to upper-level updraft. The low-level upshear tilted updraft was a function of flow over the gust front ahead of the line. Winds near storm top diverged into a leading and trailing anvil with the strongest flow occurring on the downshear side.

Approximately 3 minutes after this Doppler analysis at 2020, cell E developed on the northern end of the line as cell C started to die. The vertically averaged cross-section of cell A on the southern end of the MCS (see Fig. 20a) is contrasted with cell E on the northern end (Fig. 20b), both at nearly 30 minutes into their respective lives. The vertical cross-section normal to cell E revealed differences in the horizontal divergence pattern. The mid-level convergence for cell A was located ahead of the convective core. Cell E's convergence was located more towards the middle of the convective core. Also for cell E, the storm top divergence maximum was located downshear of the mid-level convergence, contrasting with the divergence maximum for cell A which formed directly above. Cell E's vertical cross-section further revealed a slight downshear tilt of the reflectivity core along with a more pronounced downshear anvil.

On the surface at 2015, the meso-analysis shows ridging between the dying convection of cycle 1 and the new cells of

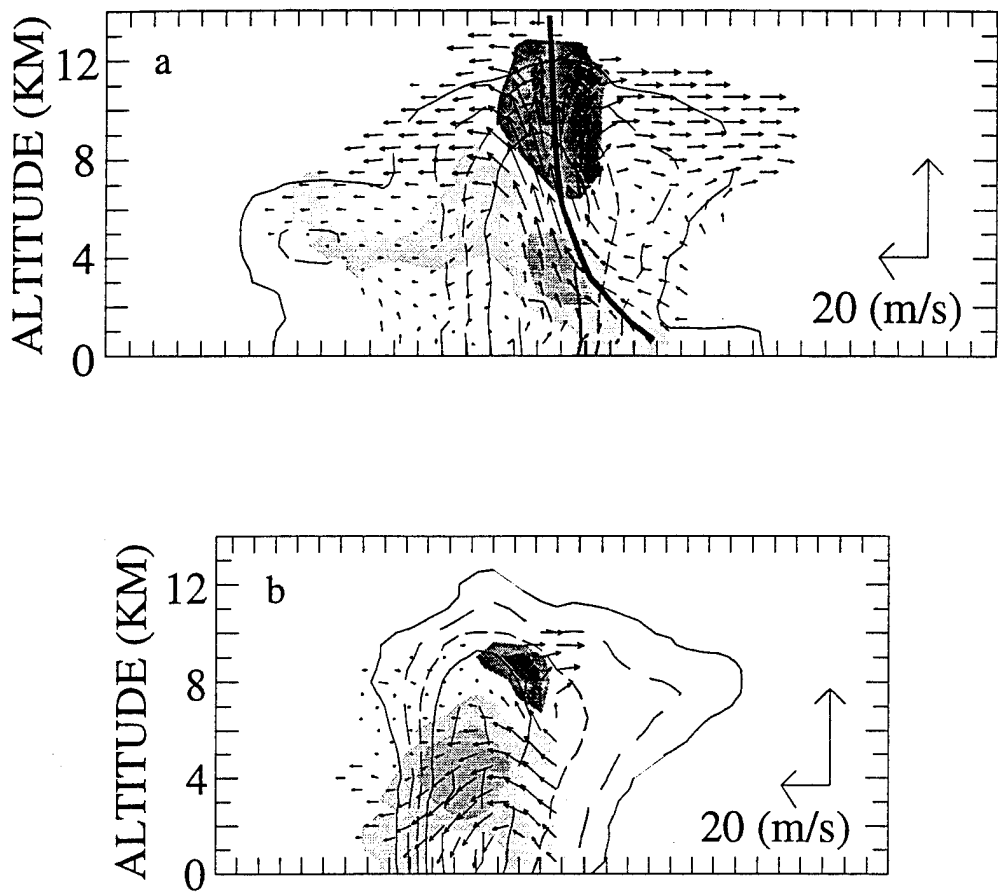


FIG. 20. Triple-Doppler analysis for a) cell A at 2017 UTC and b) cell E at 2045 UTC on 21 June 1993. Both cells were at approximately similar stages in their life cycles.

Reflectivities are a composite of the three radars with contour intervals in 10 dBZ increments beginning with 10 dBZ. Vectors depict line relative flow. A vector whose horizontal length equals one grid interval represents 7.5 m/s and vertical length equals one grid interval represents 5 m/s. Light contours enclose convergence; the starting contour is 0 to -1×10^{-4} /s and the next contour is less than -1×10^{-4} /s. Dark contours enclose divergence; the starting contour is 1×10^{-4} to 2×10^{-4} /s and the next contour is greater than 2×10^{-4} /s. The dark line in a) represents the axis of maximum updraft speeds.

cycle 2 (Fig. 21). This region was the area of the surface cold pool established by cycle 1's convection. A leading surface trough was coincident with surface convergence caused by the gust front.

5.2. 2102 Doppler and 2100 Mesonet Analyses

In this section we look at the kinematic structure and associated surface data that is representative of the intensifying stage of MCS growth. This stage is characterized by the individual cells growing and merging to form a contiguous rain area.

The original cells A, B, and D that comprised the line were about 80 minutes old at this point, while the newer northern cell E was 42 minutes old. Cells A and D merged approximately 15 minutes prior to this time and henceforth are labeled just A and referred to in the text as line A (Fig. 22). Mid-level convergence along the entire leading edge of the line enhanced the pre-existing upward vertical velocities created by surface convergence, though stronger areas of upward and downward motion were still positively correlated to the reflectivity cores. Orientation of the updraft and downdraft couplets in respect to the reflectivity cores along the length of the line varied. To the south, where the line was oriented about 30° of north,

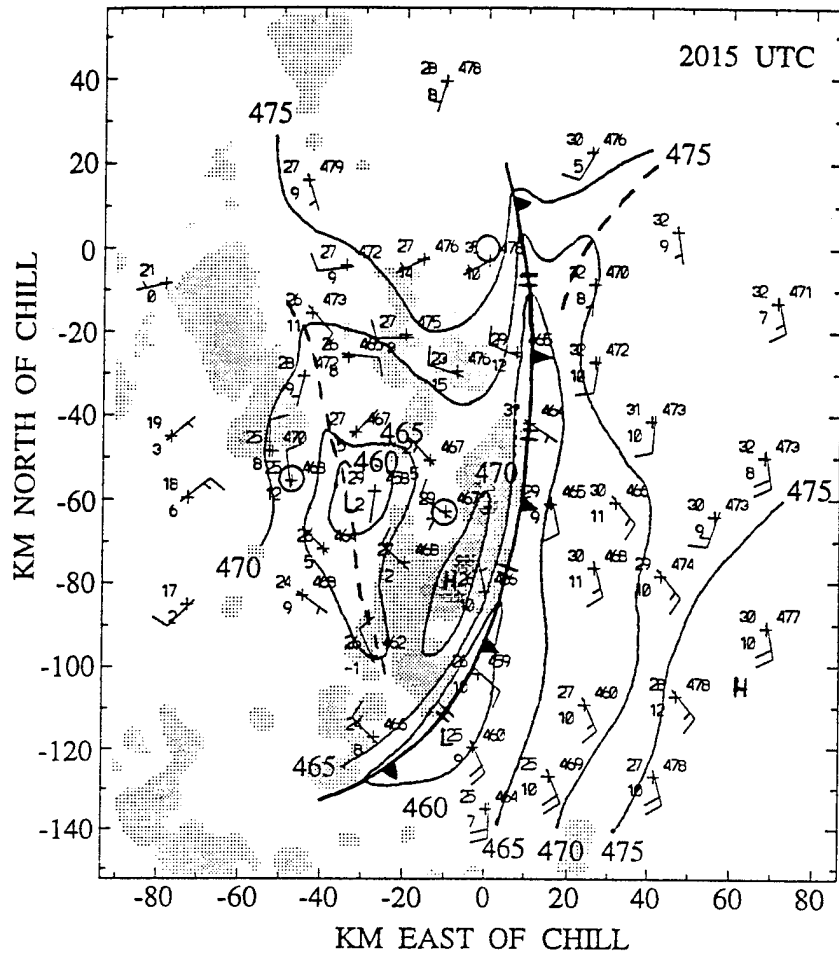


FIG. 21. Mesonet surface analysis for 2015 UTC 21 June 1993. Same plotting convention as in Fig. 12a. Station pressure is contoured at 0.5 hPa intervals (solid). MHR reflectivity cross section at 3.0 km for 2017 UTC with shading contoured at 15, 30, and 45 dBZ intervals.

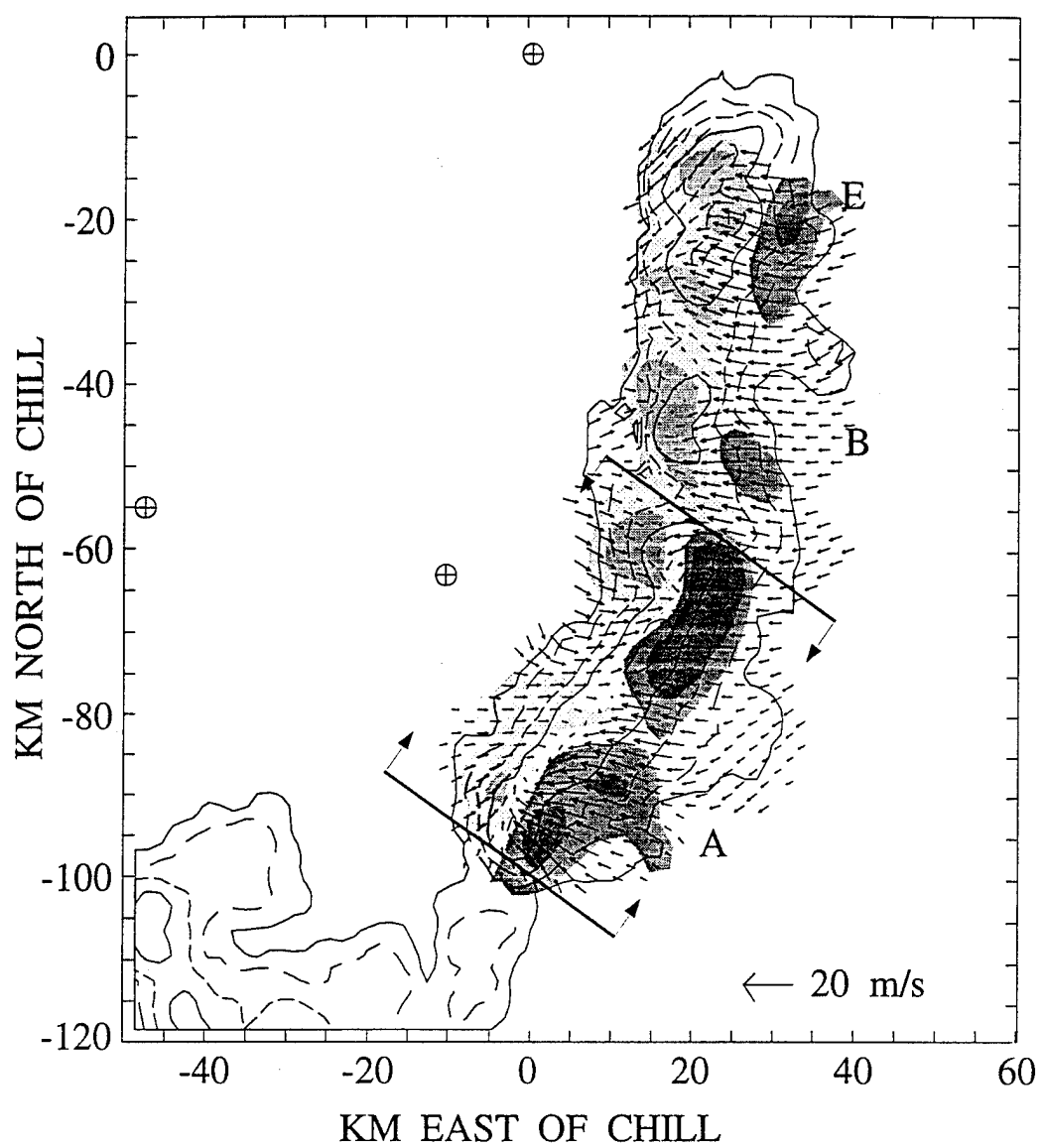


FIG. 22. As in Fig. 19 except for 2102 UTC 21 June 1993.

the velocity couplet was on the leading and back edge of the reflectivity core. The northern cells that were oriented in a north/south line had the updraft further ahead of the reflectivity core with the downdrafts located coincident to the reflectivity core. One particularly strong vertical motion couplet at the northern end of the southern line was associated with mid-level cyclonic flow and a developing mesocyclone. Also present was mid-level rear-to-front flow. This rear-inflow was prevalent throughout the back of the southern line labelled A but was not seen on the back of the northern cell E where front-to-rear flow was observed.

The averaged cross-section for the southern 40 dBZ line in Fig. 23a showed the vertical structure at the intensifying stage. A maximum average vertical velocity of 9.6 m s^{-1} was attained in the updraft with a localized maximum of 17.5 m s^{-1} . The mid-level convergence and upper-level divergence maximums had not changed much in position from the previous analysis. However, the low-level convergence center moved farther away from the convective core associated with the movement of the gust front. As in the previous analysis (see Fig. 20a), the reflectivity core again tilted slightly downshear. The upper-level anvil was well developed with a preference in growth to the downshear side. The anvil on the upshear side was 28 km wide while the downshear side was 33 km wide.

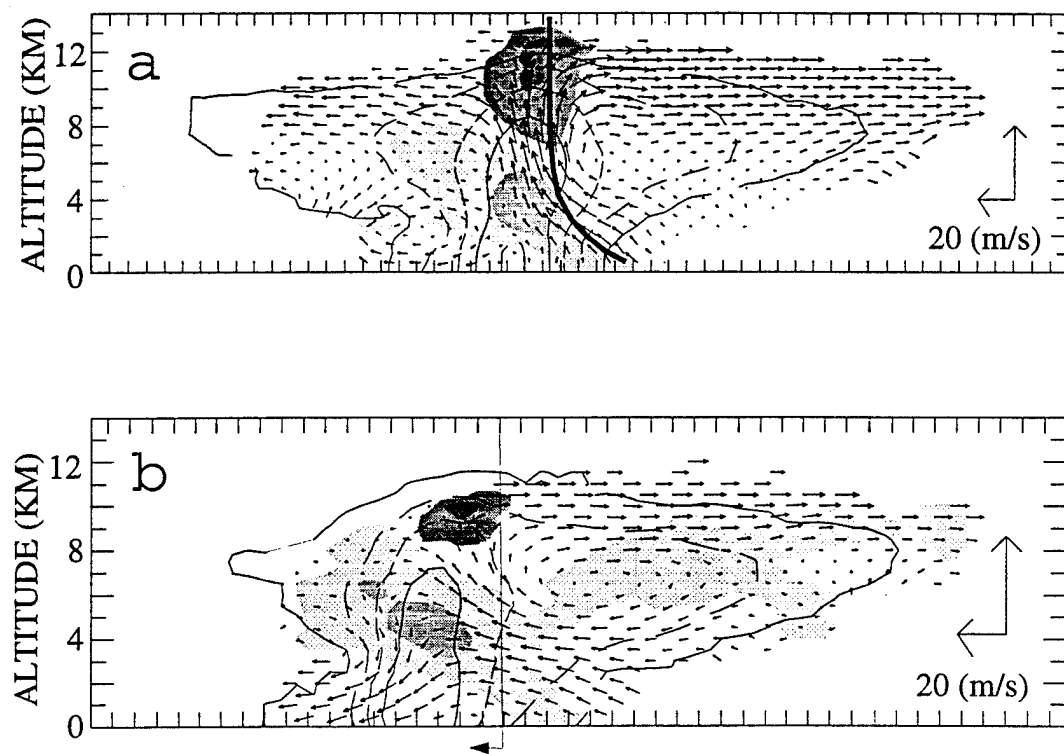


FIG. 23. As in Fig. 20 except for a) line A at 2102 UTC and b) cell E at 2131 UTC 21 June 1993. To the left of the line in b), the vertical component of the wind is unreliable.

The extent of the rear-inflow is seen clearly in Fig. 24 which showed contours of the u-component of wind normal to the line. A small averaged area of rear-inflow of over 5 m s^{-1} existed while the maximum localized speed was 8.8 m s^{-1} . Studying rear-inflow within the stratiform region of squall lines, Smull and Houze (1987b) classified rear-inflows as moderate for magnitudes between $5-10 \text{ m s}^{-1}$. As observed with Ogura and Liou (1980) for the mature stage of a mid-latitude squall line, this intensifying stage also showed a nearly conservative band of u-momentum front-to-rear flow with stronger flow at the rear of the upshear anvil.

Comparing the vertically averaged cross-section of cell E (Fig. 23a) with line A (see Fig. 23b) at the same point in its growth yielded some striking differences. Cell E showed a distinct downshear anvil with descending front-to-rear inflow, extending downshear almost the entire length of the 40 km anvil. A broad, gradual updraft led into the 25 dBZ reflectivity core for cell E in contrast to a narrow, more pronounced updraft for line A.

Associated with the leading anvil was an area of cyclonic flow approximately 25 km in diameter and located between 6 and 8 km (Fig. 25). Cyclonic flow in the anvils of MCCs and MCSs are commonly seen and called mesoscale convective vortices (MCVs) (Johnston 1982, Fritsch and Zhang

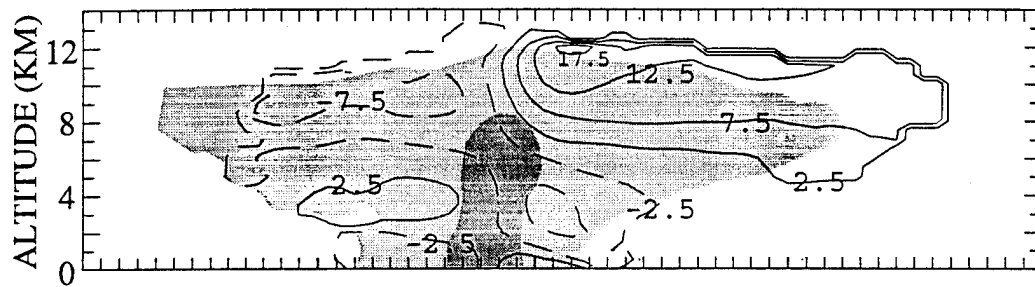


FIG. 24. Isotachs of the averaged u-component of the wind perpendicular to line A at 2102 UTC 21 June 1993. Dashed contours are -2.5 and -7.5 m/s. Solid contours are 2.5, 7.5, 12.5, and 17.5 m/s. Averaged composite reflectivity of the three Doppler radars is shaded at 10 (light) and 40 dBZ (dark). Horizontal axis is ticked every 2 km.

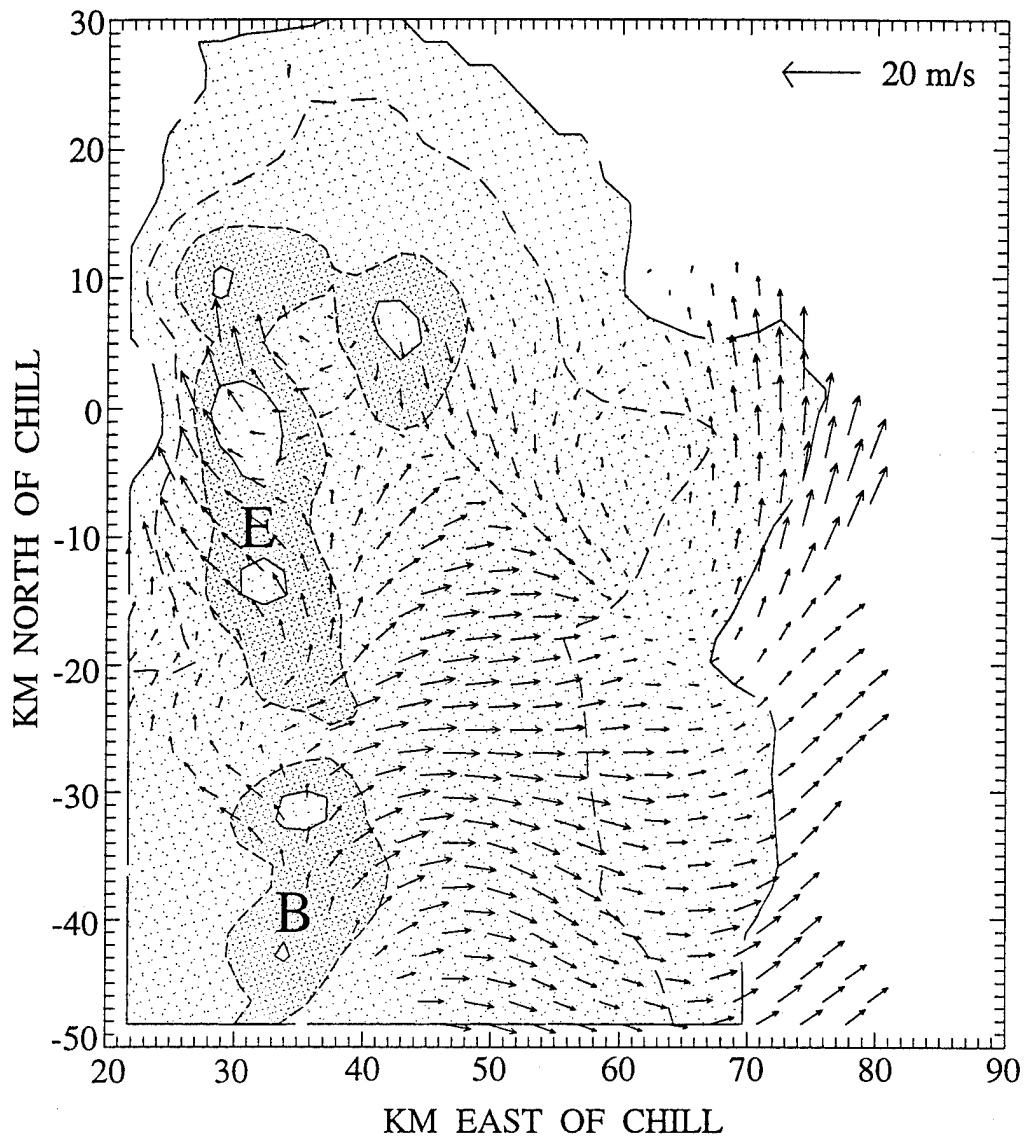
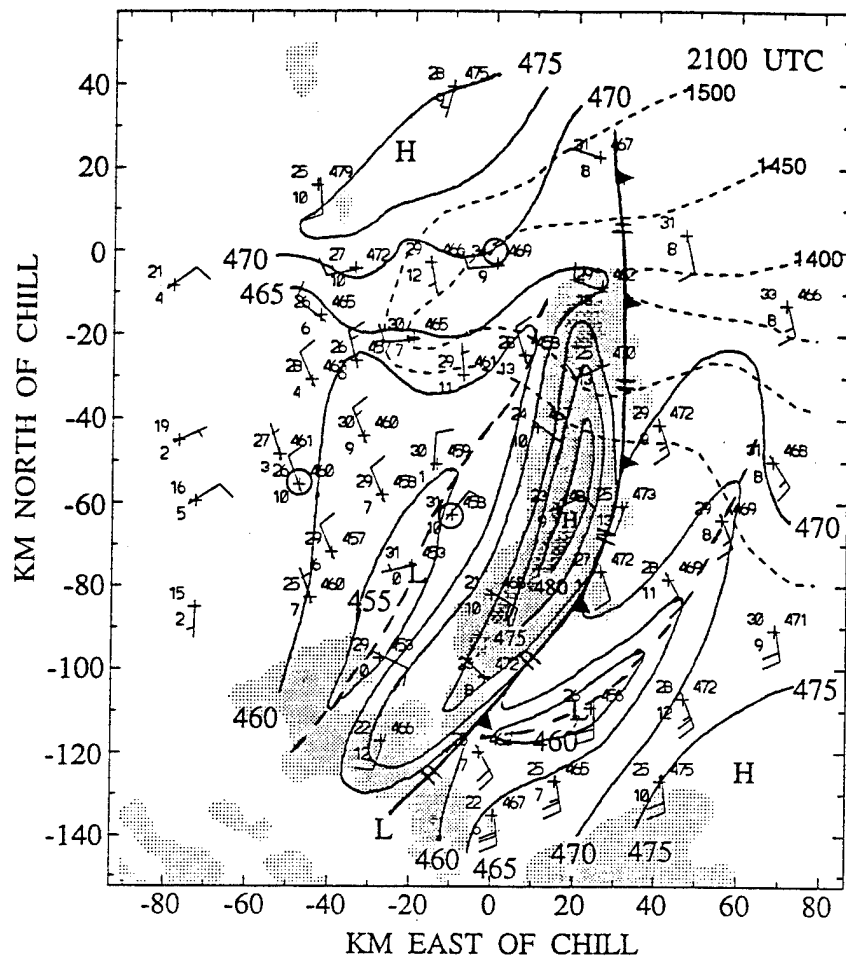


FIG. 25. Dual-Doppler analysis using CHILL and MHR at 7.5 km AGL for 2102 UTC on 21 June 1993. MHR reflectivity contour intervals and shading are in 10 dBZ increments beginning with 10 dBZ. Vectors depict line relative flow. A vector whose length equals one grid interval represents 5 m/s. Cells B and E are identified.

1987, Stirling and Wakimoto 1989, Brandes 1990). This MCV developed after the previous analysis 15 minutes earlier (not shown) and as this is the last available Doppler analysis, we could not determine the evolution of the cyclonic flow. Short-lived circulations of varying intensities were present at mid to upper levels starting at 2045 and onward (not shown) and were determined to be turbulent eddies rather than dynamically forced features. Therefore any conclusions about the observed cyclonic circulation and possible MCV would be premature.

The effects of the squall line on the surface is shown in Fig. 26. At 2100, a well defined mesohigh was located beneath the line of convection. A broad region of higher pressure was also located in front of the convection under the leading anvil. Warm south-southeasterly winds ahead of the squall line suggested that the gust front had not propagated well ahead of the convection and therefore was not the cause of the higher pressure under the leading anvil. Three troughs existed, one being the gust front along the leading edge of the convection, another located behind the storm in a wake-low position, and a third located further ahead of the gust front trough. Speed convergence was evident across the leading trough.



5.3. Vertical Profiles of Kinematic Fields

Further insight into the development of the squall line and the differences between the southern and northern ends is ascertained through a time-series of vertical profiles. Fig. 27 reveals the average horizontal divergence for the first six analysis times for cell/line A. At the surface, weak divergence generally strengthened in time suggesting an increasing influence from evaporatively cooled downdrafts. Convergence at mid-levels dominated with progressively increasing strength over time. Also noted was an increased depth to the mid-level convergence with the level of non-divergence (LND) stopping at about 6 km in the final analysis. Near storm top, divergence quickly peaked, then weakened for about 45 minutes, strengthened again, then finally weakened to a temporal minimum. Associated with these divergence profiles are a series of maximum upward velocities (Fig. 28). These values are contrasted with the values calculated by Weisman (1988) for a 2-D non-hydrostatic model under weak-shear conditions. Though the magnitudes are roughly 25% less than Weisman's simulation, the orientation of maximums and minimums are highly correlated. In Weisman's simulations, the second vertical velocity maximum at 60-75 minutes was the result of new convection being initiated by a propagating gust front. In

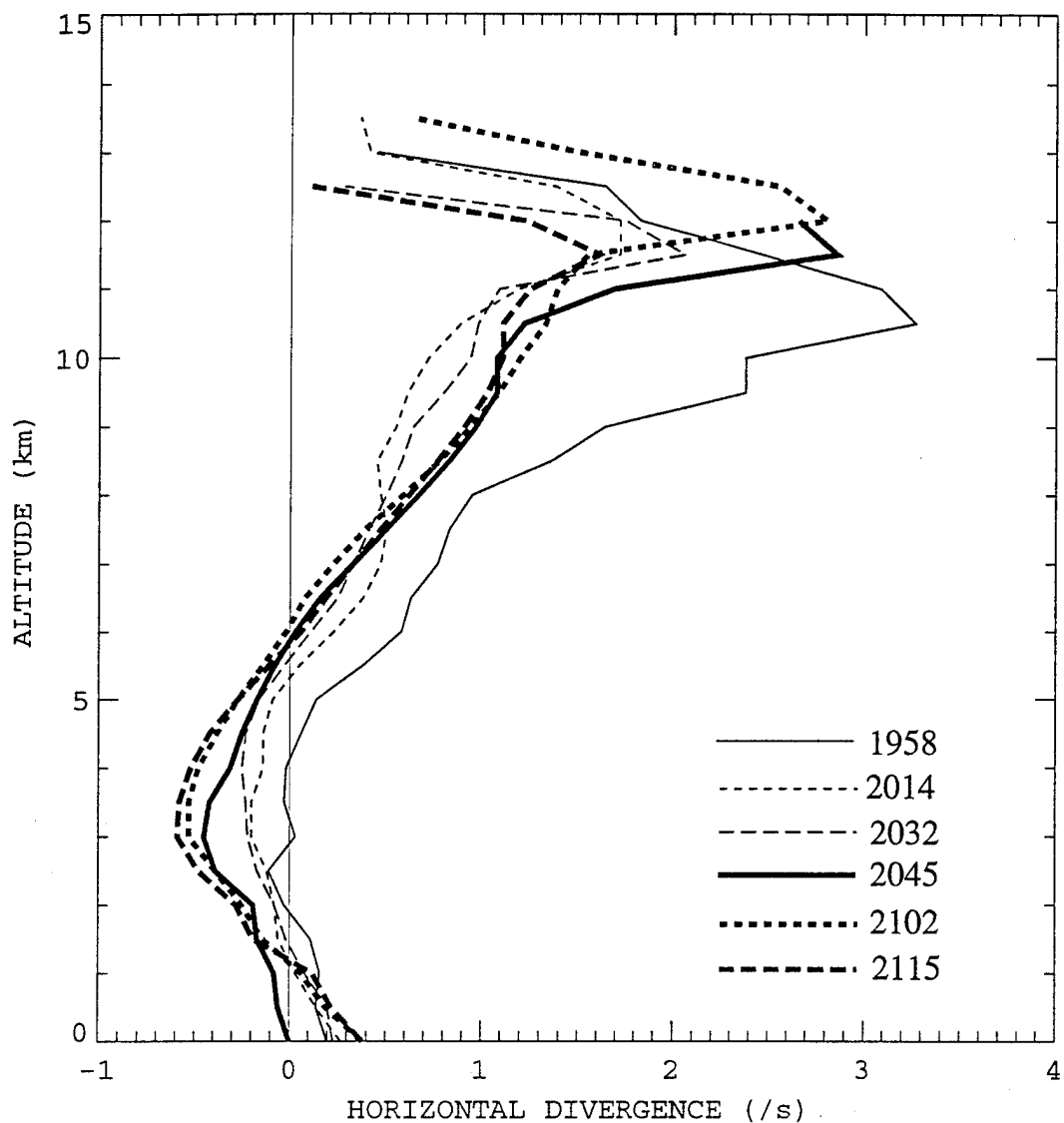


FIG. 27. Vertical time series plot of horizontal divergence ($10^{-4} /s$) calculated upon cell/line A for the times 1958 UTC through 2115 UTC on 21 June 1993.

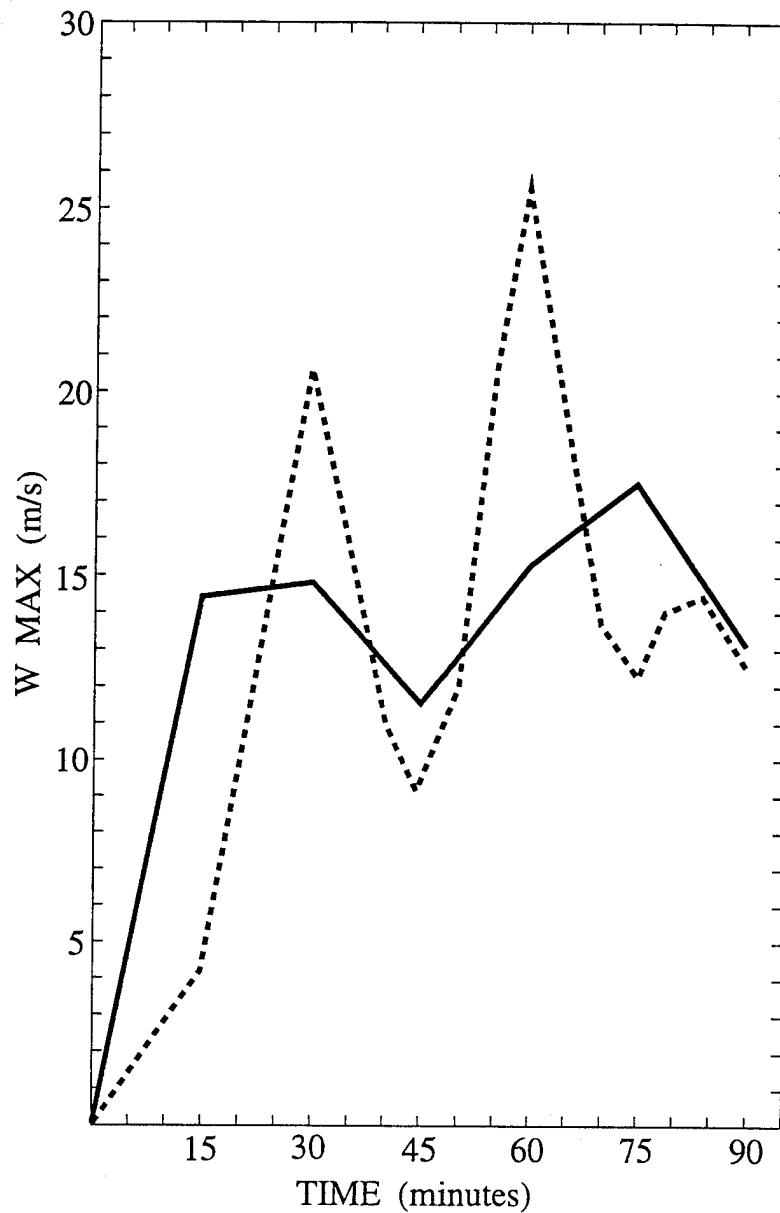


FIG. 28. Time series plot of the maximum vertical velocities for the WKR numerical simulation for 2.5 km deep surface shear layer at 10 m/s oriented perpendicular to the line (solid) and the observed values for cell/line A (dashed) for the first 90 minutes.

this study, the 75 minute vertical velocity maximum was the result of an influx of higher θ_e air. The lesser maximum updraft speed was attributed to the environmental conditions which yielded a CAPE of 1149 J kg^{-1} while Weisman's simulated environment had a CAPE of 2200 J kg^{-1} .

Vertical profiles of horizontal averages in a 2 km wide box, centered approximately 10 km ahead and behind the convective cores of the previously defined line segments, were constructed to further categorize the flow around the MCS. The boxes were advected with the storm to show the evolution of the flow at approximately the same location in the storm. This was done separately for the southern and northern sections of the line.

Figure 29 shows the results for the southern section. The back of the squall line showed an increasing surface outflow at low-levels. On the front, there was no indication that the gust front leading the squall line propagated away from the storm. With the strengthening outflow at the surface, the increasing mid-level convergence (see Fig. 27) provided mass for downdrafts and correlated well with the surface divergence. At mid-levels, an increased rear-inflow was readily apparent on the back. The maximum winds were generally found at about 3.5 km with a magnitude of 4.7 m s^{-1} . On the front side of the squall line, the storm relative inflow increased with the maximum

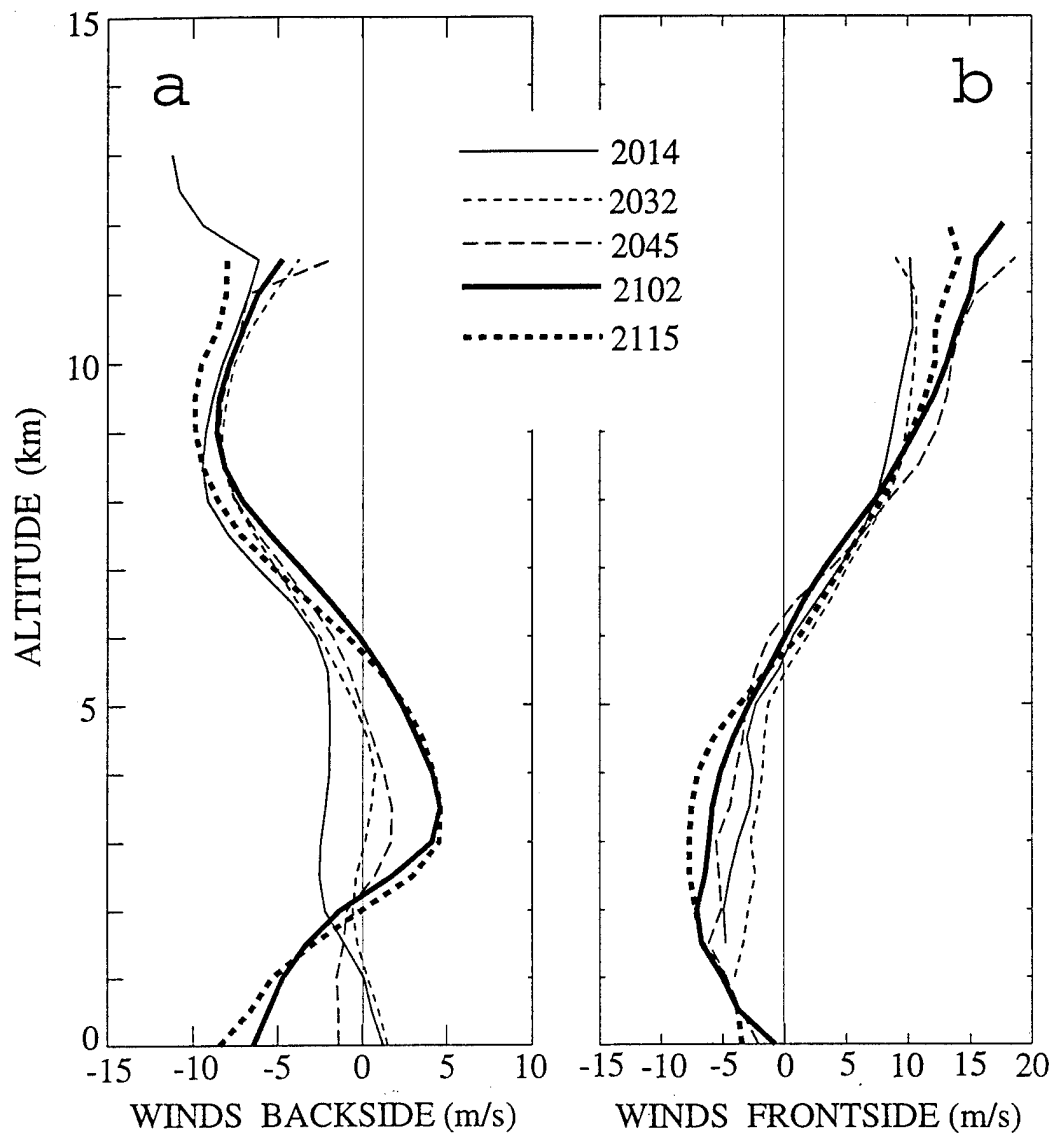


FIG. 29. Vertical time series plot of averaged winds (m/s) calculated upon cell/line A on the a) back and b) front of main convective line for the times 2014 UTC through 2115 UTC on 21 June 1993. Domain used for the averaging was located approximately 10 km behind and ahead of main convective line and was advected with the storm to yield winds representative of the same approximate location within the storm.

winds found lower at 2.5 km and stronger at 7.7 m s^{-1} than the back side of convection. Vertical cross-sections of low-level flow showed the low-level updraft becoming more tilted with time. Since the low-level, upshear tilted updraft did not extend throughout the depth of troposphere, an increased horizontal component of the wind enhanced convergence at mid-levels. The convergence at mid-levels in the divergence profile also correlated well with the vertical wind profiles. Near storm top on the back side, the negative velocities remained nearly uniform in structure and speed. The maximum flow in the upshear anvil at the 9 km level was 8.5 m s^{-1} . The front side did experience fluctuations that account for the differing divergence strengths aloft (see Fig. 27). Most of the change in upper-level divergence was attributed to flow downshear of the storm. The magnitude of the flow in the downshear anvil varied between 10.0 to 18.5 m s^{-1} . When upper-level divergence and upward velocities were maximized, the flow in the downshear anvil was between 130-145% larger than that of the flow in the upshear anvil.

Differences between the divergence profiles of cell/line A (see Fig. 27) and cell E are seen in Fig. 30. Surface divergence and mid-level convergence were persistent though varied in strength throughout the cell's intensification. Maximum mid-level convergence for cell E was about 100%

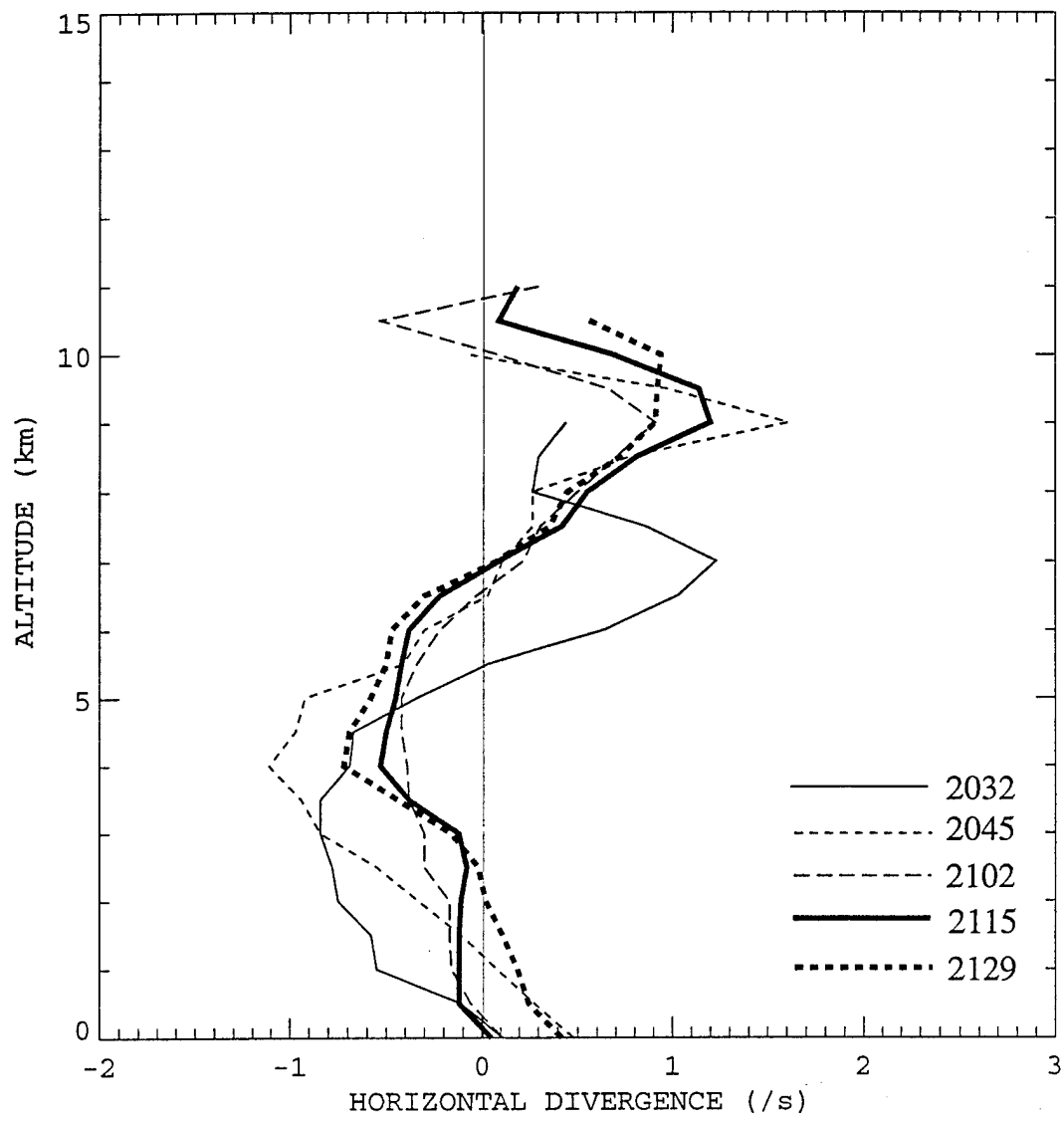


FIG. 30. Vertical time series plot of horizontal divergence ($10^{-4} /s$) calculated upon cell E for the times 2032 UTC through 2129 UTC on 21 June 1993.

greater than the maximum for cell/line A. Also the LND was located approximately 1 km higher for the final analysis time as compared to the maximum height for any of the analysis times for cell/line A. The height of the maximum in the convergence was approximately 4 km which was also 1 km higher than cell/line A. The upper-level divergence location and strength were believed to be suspect above 9 km caused in part by the storm-top being unresolved as a result of the low maximum scan height by the CSU-CHILL radar.

Plots of vertical winds on the front and back of cell E, (Fig. 31), were calculated in a similar fashion as Fig. 29. Winds on the back side of the storm in Fig. 31a exhibit the greatest variability of all vertical wind profiles. Winds were generally front-to-rear below 4 km and rear-to-front above 4 km. General levels of relative maximas and minimas are labelled on the profile. The horizontal wind profile for the front side (Fig. 31b) was much more consistent than the back-side and looked very similar to the profile for the cell/line A (see Fig. 29b). Diverging winds from stronger rearward flow on the back than the front correlated well with the divergence profile. Surface flow on the front did experience an increased strength to the point where the flow was moving away from the MCS. This flow suggested that the gust front may have started moving away from the squall line. At mid-levels up to 4.5 km, stronger rearward flow on

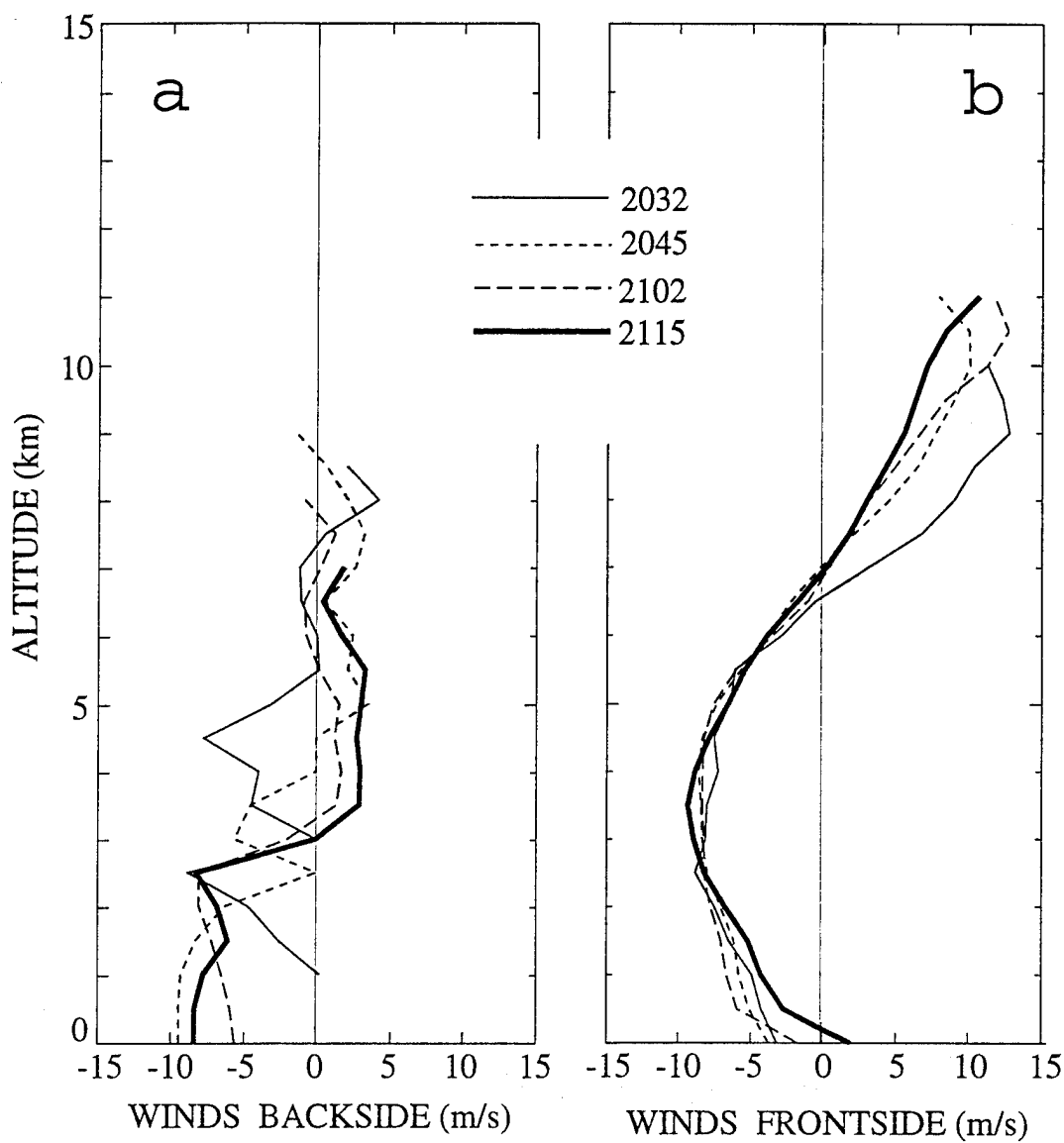


FIG. 31. Vertical time series plot of averaged winds (m/s) calculated upon cell E on the a) back and b) front of main convective line for the times 2032 UTC through 2115 UTC on 21 June 1993. Same procedures used to determine wind profile as in Fig. 29.

the front than the back caused speed convergence. From 4.5 to 6.5 km, the mid-level convergence became a combination of both speed and directional convergence. At upper levels, speed divergence existed due to stronger leading flow along the front than the back. Above 8.0 km on the back-side of the cell, there was little to no flow rearward which agreed with the lack of an upshear anvil.

A time series of the updraft tilt is shown in Fig. 32. The tilt was objectively determined by connecting the maximas of surface convergence, mid-level convergence, and upper-level divergence. This method correlates well with the axis of maximum upward motion as seen in Figs. 20a and 23a. For the southern cell/line A (Fig 32a), the only tilt to the updraft was from low to mid levels which was primarily below cloud base. This tilt is associated with the gust front moving away from the line. From mid to upper levels within the storm, a nearly upright updraft existed throughout the analyses. The upright updraft did exhibit a slight upshear tilt throughout which allowed the updraft and downdraft to remain separate. For the northern cell E (Fig. 32b), the low to mid levels again show the upshear tilted updraft. The location of the upper level divergence maxima tended to move rearward with time. This factor is attributed to the unresolved storm-top. By the last analysis, the divergence location was considered to be more

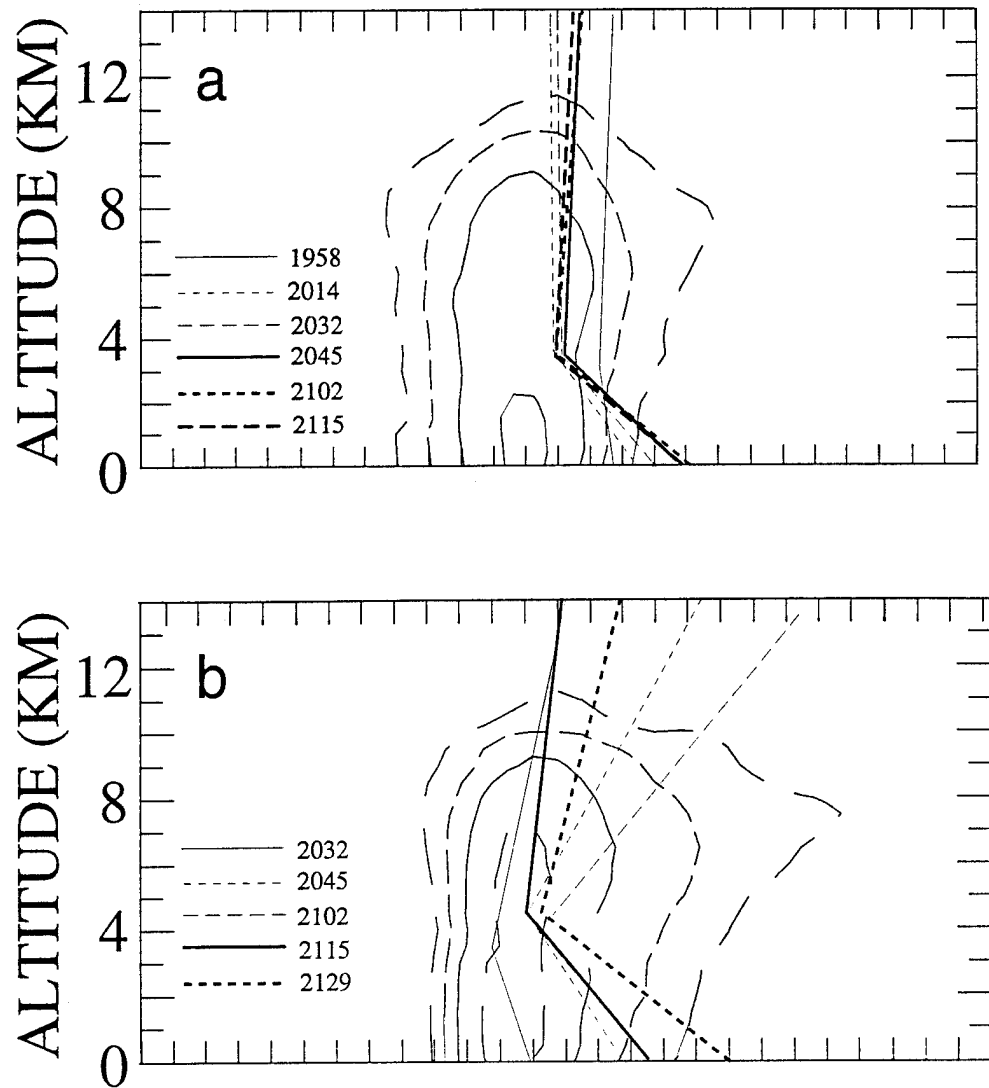


FIG. 32. Vertical time series plot of updraft tilt calculated upon a) cell/line A and b) cell E for the times indicated in the respective legends for 21 June 1993. Updraft tilt objectively determined by connecting the maximums of the surface convergence, mid-level convergence, and upper-level divergence. Representative reflectivities are at 2017 for cell/line A and 2045 for cell E. Reflectivities are contoured at 10 dBZ intervals starting at 20 dBZ.

representative of the true situation as more of the storm-top was resolved after moving farther away from the CSU-CHILL radar. This last analysis showed a downshear tilt from mid to upper levels which was opposite to the southern end.

Asymmetries between cell/line A and cell E persisted throughout the analyses. The asymmetries identified in this chapter included the differing location of the anvil and rear-inflow jet, updraft orientation and structure, divergence and wind profiles. In the following chapter we address these asymmetries in light of the observed environmental inhomogeneities. We also compare these observations with the RKW conceptual model.

Chapter 6

DISCUSSION

Many asymmetries existed within the 21 June 1993 squall line that did not fit the Houze et al. conceptual model (see Fig. 1). In numerical simulations by WKR, the evolution of convective lines (which included the Houze et al. squall line structure) under a wide range of vertical shear conditions was accomplished. Comparisons are made between this observed case and the WKR simulations for a low-level vertical wind shear of 10 m s^{-1} through 2.5 km and 5.0 km AGL (WKR; see Figs. 5 and 15 respectively) which was closest to our observed 8 m s^{-1} shear over similar levels. When the simulations are compared to both the 40 dBZ cell/line averaged vertical cross-sections for the northern and southern ends (see Fig. 23a and 23b), many differences are observed (Table 2). The occurrence or non-occurrence of all the WKR features within the squall line were all explained by the relationship between the downdraft induced cold pool and ambient vertical wind shear. With so many differences observed, one has to consider the validity of the model and the reasoning behind the explanations for the model results. Answers to why discrepancies existed between the numerical simulations and observations may rest upon the

Table 2. Comparisons between the WKR numerical simulations using vertical wind shear of 10 m s^{-1} over 2.5 and 5.0 km and the observations between cell E on the northern end of the squall line and cell/line A on the southern end.

	Conceptual Model	Observed North	Observed South
Upshear tilted updraft throughout the depth of the troposphere	Yes	NA	No
Predominantly upshear anvil	Yes	No	No
Propagation of squall line through a typical multi-celled fashion	Yes	No	No
Rear-inflow jet	No	No	Yes
Descending front-inflow jet below the leading anvil	No	Yes	No

inhomogeneous environmental factors present in this observed event. The numerical simulations were initialized with a homogeneous environment whereas the observed environment was inhomogeneous. These inhomogeneities are almost always present in the environment and have a significant role in the establishment of observed asymmetries and variance from within squall lines.

6.1. Impacts of Shear

Vertical wind shear is recognized as a major contributor to the structure and longevity that many convective systems exhibit (Chisholm and Renick 1972, Weisman and Klemp 1982, 1984). In the numerical modeling work of Thorpe et al. (1982), Weisman and Klemp (1986), and WKR, moderate shear confined to the lowest 2.5 km with constant winds above was determined as optimal to the strongest and longest-lived convective systems. By varying the shear profile alone, a wide range of observed squall line structures and longevities were simulated. For squall line structures, WKR found that weak shear oriented perpendicular to line produced a wide band of short-lived ordinary cells. Moderate shear oriented perpendicular to line produced regenerating short-lived cells along the gust front in a multicellular fashion. Strong, deep shear oriented at a 45°

angle to the line manifested a series of quasi-steady, rotating supercells. In all WKR simulations, shear was confined to the lowest 5 km.

Fig. 33a,b shows the shear profile relative to the line for both the northern and southern ends using the 1700 sounding. Shear below 7 km was generally less than 10 m s^{-1} but above this was a strong 30 m s^{-1} shear layer over 5 km deep. Numerical simulations documented in literature do not show the analyses for upper-level shear profiles since the low-level shear is considered more important to MCS growth and longevity. Therefore, inferences from other simulations were required to account for the impact this upper-level shear may have had on the squall line. Such a simulation for a 5 km deep layer was accomplished by WKR for a 20 m s^{-1} shear (WKR; see Fig. 17). Although the shear layer was 7 km lower than our observed case, the structure of the simulated vertical cross-section was very similar to what was observed (much more than to the 10 m s^{-1} shear over the lowest 2.5 km (WKR; see Fig. 5)). A more accurate downshear anvil and mid-level inflow were now observed in the stronger, deeper sheared simulations. The reason for the downshear anvil is an upper-level, horizontal, downshear directed pressure gradient (WKR, see Fig. 18). Raymond (1978) diagnosed and Cotton and Anthes (1989, pg. 425) documented simulations that produced regions of positive

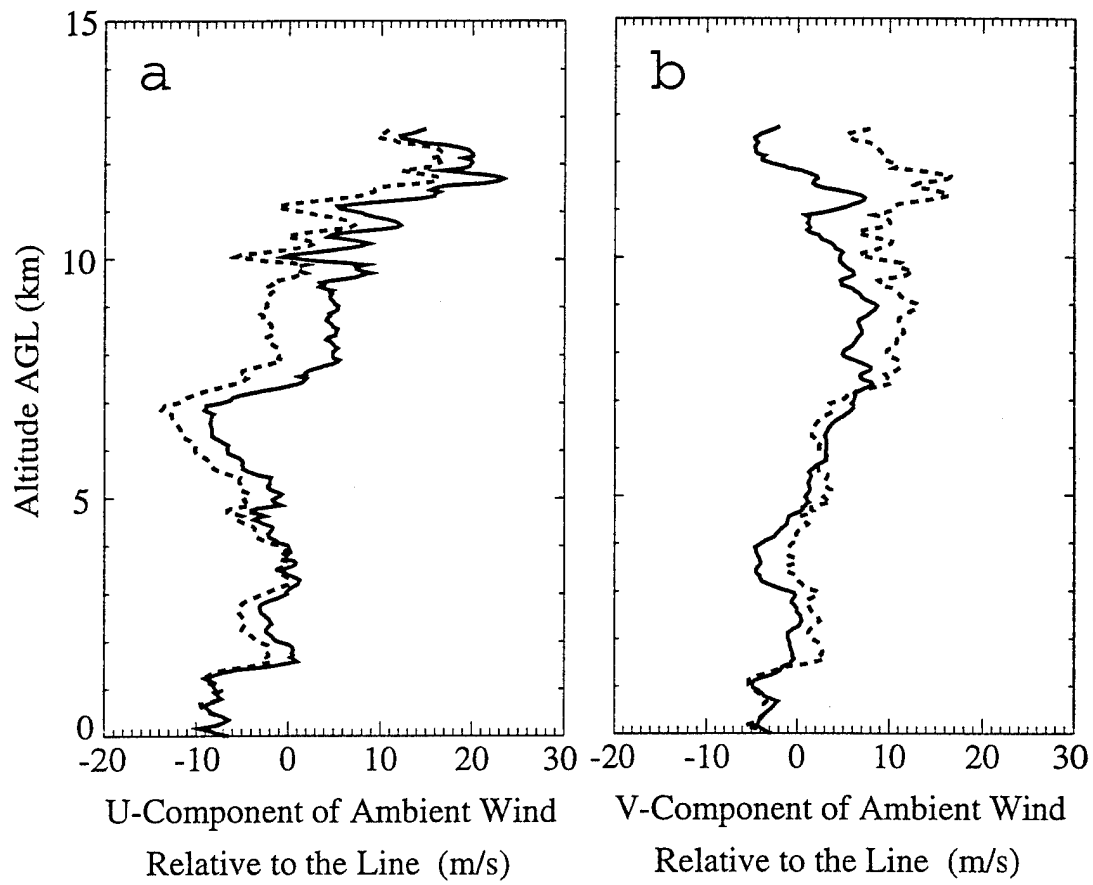


FIG. 33. Ambient wind profiles of a) u-component of the wind and b) v-component of the wind relative to the differently oriented line. Cell E (solid) was oriented north/south and cell/line A (dashed) was oriented north-northeast/south-southwest. Ambient wind determined from the 1700 UTC 21 June 1993 CLASS sounding.

pressure anomalies upwind of actively growing cumuli in a sheared environment. The higher upwind pressures were attributed to non-hydrostatic pressures in the horizontal caused by easterly momentum updraft air encountering westerly flowing, environmental air. It is plausible that this physical mechanism may have been the cause of our downshear anvil. Fig. 34 shows the environmental winds relative to storm motion for the three WKR simulations and the observed 21 June squall line. At low-levels, westward motion and shear of varying strengths exists for all cases. At mid to upper-levels westward relative motion exists for the two upshear anvil cases and eastward relative motion dominates over the two downshear anvil cases. This suggests that many of the observed features present within this case and the simulations may have occurred from the squall line's relative motion in the ambient shear which induced non-hydrostatic forces of varying strengths at all levels. This is contrary to the cold pool/ambient low-level shear conceptual model. It states that the tilt of the updraft, which is impacted by circulations along the leading edge to the cold pool, causes the observed features. Although much significance has been placed upon low-level vertical shear, neglecting mid to upper-level shear may result in inaccurate simulations in some cases. This case study does indicate the importance of the upper level shear.

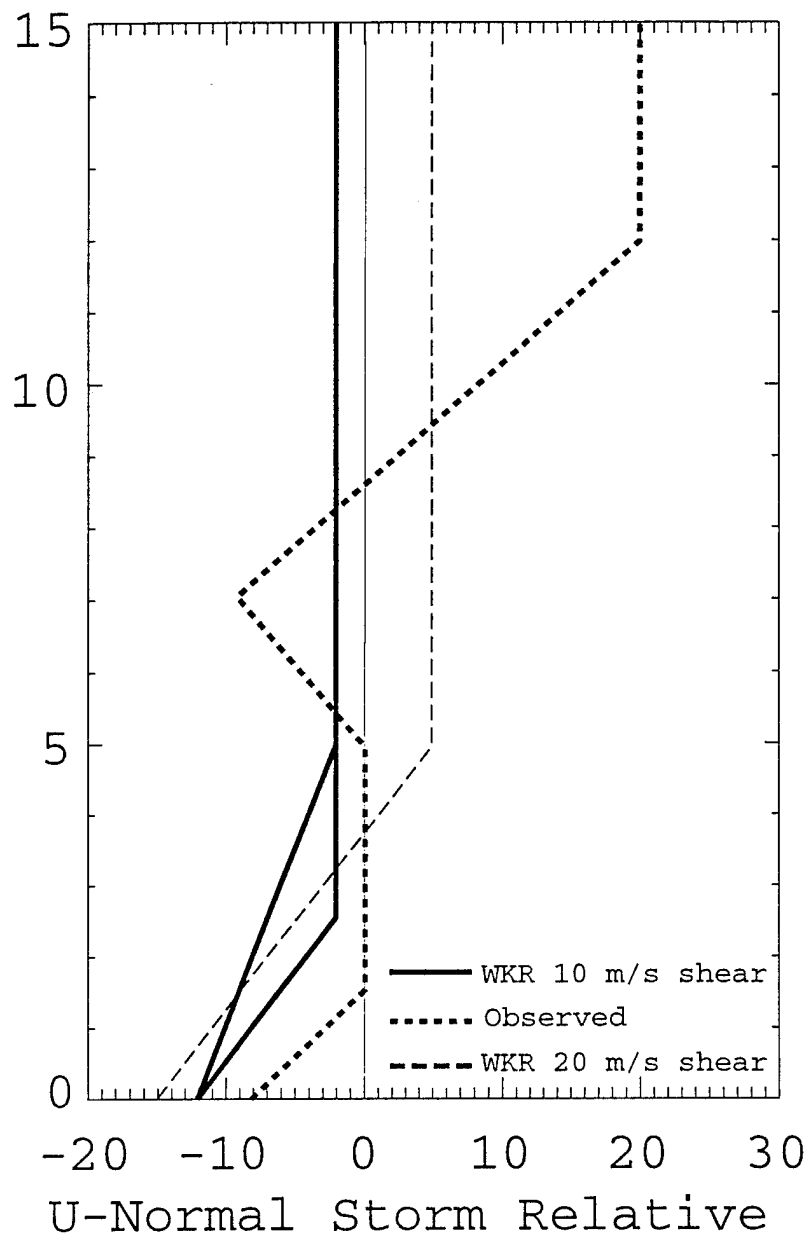


FIG. 34. Wind profile of the u-component of the wind relative to the storm motion. Cases plotted indicated in legend. Positive storm relative flow indicates downshear propagation and negative storm relative flow indicates upshear propagation. Observed storm relative profile from the 1700 UTC 21 June 1993 CLASS sounding.

Within the line itself, two different modes of ordinary cells existed. Bluestein and Jain (1985) in their further discussion section ask, "and since there is a systemic relation between squall line orientation and the vertical shear, could it be that the relative orientation of the surface boundary to the vertical shear is an important factor?" This appears to be true for this case. In Fig. 33a, the northern end of the line, which was oriented in a north/south direction, shows a stronger cross-line flow than the south. But in Fig. 33b, the southern end, which was oriented more northeast/southwest, shows a stronger alongline flow than the north. This does indicate that the orientation of the line could indeed have had an impact on the structure of the squall line and hence its evolution and observed asymmetries.

6.2 Impacts of Thermodynamics and Topography

Like vertical shear, variations in thermodynamics and topography complicated comparisons to the WKR conceptual model and may have also yielded asymmetries along the line. Thermodynamic properties of the environment vary widely in time and space. As noted previously, all the RKW, WKR, and Weisman simulations used a representative sounding in an homogeneous environment for model initiation. Their

sounding showed a LFC of 1.7 AGL from an approximate surface temperature of 24 °C and dew point of 18.5 °C. These low level conditions are not common for the favored zone of convective initiation along the foothills of Rockies. The observed sounding in Fig. 7 shows a more typical thermodynamic profile which yielded a LFC of 3.1 km. This LFC is over 1.4 km higher than the environment used in the numerical simulations. In the numerical simulations that yielded optimal squall line development, the cold pool that developed was between 1.7 and 2.5 km deep (Weisman 1992; see Fig. 2). With an LFC of 1.7 km, convection starts along the leading edge of the gust front which allows the circulation created from the horizontal buoyancy gradients to enhance the updraft initiated from surface convergence. In this case, convection did not initiate along the leading edge of the gust front. With a shallow cold pool and high LFC, convection was initiated 7-10 km behind the leading edge of the gust front.

In the updraft tilt time series (Fig. 32), the only change in the tilt for the southern end of the squall line was a slight progression to a more upshear tilted updraft at low-levels. From the WKR cold-pool/ambient shear conceptual model, this low-level updraft tilt would be explained by the circulation along the leading edge of the gust front being greater than the circulation inherent in the low-level

ambient vertical wind shear. Their model would also suggest that this upshear tilted updraft created in the low-levels would extend throughout the depth of the troposphere. If this causal relationship were true in all cases, why did the updraft turn sharply upward upon reaching cloud base as observed in this case? This observation suggests that the circulations did not dominate the observed structure but that other factors existed.

It is hypothesized that the location of the convection 10 km behind the leading edge of the gust front and the height of the LFC minimized the impact of the cold pool induced circulation at cloud base. These two observations can be attributed to drier and weakly sheared lower levels which resulted in a shallower cold pool and the higher LCL. Once the rising airmass reached the LCL it became more positively buoyant and accelerated upward. The associated release of latent heat would have created a $p' < 0$ and the horizontal mass convergence that was observed. As the air accelerated upward, it became increasingly shielded from the effects of the environmental shear. The mid to upper-level updraft did exhibit a slight upshear tilt throughout the analyses. This could possibly be a function of the conservation of momentum seen throughout the analyses and shown in one analysis in Fig. 24. The deep, well-mixed sub-cloud layer may have contributed by allowing for a larger

updraft that was less susceptible to entrainment and slower to respond to any pressure gradient forces present, although this could not be shown from our observations.

With the preceded hypothesis, a caveat should be placed on the ratio of the cold pool strength to low-level vertical wind shear to determine the structure and longevity of squall lines (RKW, WKR, amongst others). This conceptual model is only applicable to specific environmental conditions.

The issue of the updraft is further considered as we look at the impact topography had on the horizontal thermodynamic field. As recognized in the introduction, many of the MCS that occur over the Midwestern United States find their roots along the eastern slopes of the Rocky Mountains where topography varies greatly. The impact of topography upon the initiation of cycle 1 convection along the Front Range is addressed in chapter 3. Here we look at the impact that the topography of the northeastern Colorado plains had in determining the discrepancies between the conceptual model and within the line.

Figure 26 shows the northern cell located in the Platte River valley while the southern end of the line is located along the Palmer Divide. The difference in surface height from one end of the squall line to the other was approximately 0.5 km. Although θ_e values for the air mass

entering the squall line were generally the same, excluding the concentrated moisture tongue, the type of air mass was generally different. To the north in the region of the lower Platte River Valley, temperatures were generally higher while the dew point temperatures were lower than the air to the south along the Palmer Divide. The higher southern end had a lower lifted condensation level (LCL) and shallower mixed layer while the lower northern end had a higher LCL and deeper mixed layer. These differences could impact the updraft size and structure through the lifting of the mixed layer. The higher southern end would have a narrower updraft and would therefore be more susceptible to entrainment. The lower northern end would have a broader updraft and a more undiluted updraft core. As seen in Fig. 23a, the updraft in the southern line showed an updraft that quickly turns upward upon reaching the LCL. To the north, the updraft was generally deeper and did not exhibit the sharp turn upward that occurred on the southern end. Another result of the deeper, drier sub-cloud layer would be increased evaporational cooling in the downdrafts. Therefore to the north you might expect to see a stronger and faster moving cold pool. Fig. 31b did show low-level winds moving away from the convective line in time where in the south they did not. This may be a possible explanation for this observation. With the enhanced cold pool and

associated gust front, strengthened surface convergence along the gust front should have increased the likelihood of new cell development. This hypothesis is confirmed as new cell development did occur off the northern end of the squall line.

Although new cells initiated along the downshear side of the southern portions of the squall line, these cells did not develop like the cells to the north did. Some form of suppression precluded the cells from developing.

Circulations below the leading anvil (see Fig. 23a) created from evaporational cooling of stratiform precipitation are hypothesized to have suppressed the convection. This suppression below the leading anvil was aligned above the new cell development that was initiated from the gust front. At about 2230 a strengthened gust front occurred (see Fig. 11). This may have occurred because of a descending rear-inflow jet, collapse of the convective cells, or most likely a combination of the two. This intensified gust front is believed to have propagated out from under the suppression zone into a more favorable environment for convective development. Within one hour, new convection formed discretely out ahead of the old convective line (see Fig. 10g). At this point, the original convective cells and line along the southern portion of the squall line were almost 3 hours old.

Along the northern end of the squall line, circulations below the leading anvil were also present (see Fig. 23b) but convection was not suppressed (see Figs. 10d-f). This is because the suppressive zone was not aligned above with new convective activity but was located farther away from the original squall line. It is suspected that the broadly ascending updraft along the northern portions of the line may have helped to keep the circulation farther out front of the squall line. Whereas the southern portion of the line appeared to propagate discretely, the northern end appeared to propagate in a more typical multicellular fashion. Multicellular convective activity along the northern portion was evidenced in the two lines of convection in Fig. 10f. Although the last two lines of convection occurred in approximately 30 minute cycles, the original convection still existed for almost one hour, again exhibiting a cell lifetime not typically observed.

Chapter 7

SUMMARY AND CONCLUSIONS

On 21 June 1993 a non-severe squall line developed along the northern foothills of the Colorado Rocky Mountains. It was observed by 3 Doppler radars, a dense surface network consisting of 48 PROFS/PAM stations, 2 wind profilers and accompanying RASS, and rawinsondes. This squall line trailed an upper-level short-wave trough and formed in an environment that yielded a CAPE of approximately 1150 J kg^{-1} with weak vertical shear of the horizontal wind at low to mid-levels but strong shear at upper-levels. This MCS was a subset of a larger MCS that moved from Colorado to Minnesota, lasting through 0800, 23 June. Initiation of the system occurred from a gust front that developed from earlier convection over the Front Range.

Significant differences in the structure of the squall line were observed between the southern portion of the line, which was oriented in a north-northeast/south-southwest direction, and the northern portion of the line, which was oriented in a north/south direction.

- A rear-inflow jet was observed on the southern end but not on the northern end.

- A descending front-to-rear inflow jet was observed below the forward anvil in the north but not in the south.
- Towards the north the line was characterized by a dominant forward anvil, while to the south the leading and trailing anvils were of near equal extent.
- New cell growth did not develop under the leading anvil to the south but they did to the north. This resulted from a suppression zone located closer to the convective line in south than in the north.
- Propagation of the squall line appeared to have occurred discretely in the south but occurred in a more typical multicell fashion in the north.
- The surface air along the southern portion of the squall line was cooler, moister, and located at higher elevations along the Palmer Divide, while the surface air along the northern portion was warmer, drier, and located at lower elevations in the Platte River Valley.
- As a result of the previous observation, a shallower sub-cloud layer existed to the south while a deeper sub-cloud layer existed to the north.

This squall line was also compared to the squall line simulations of WKR for the weakly sheared cases. Many differences were observed:

- A rear-inflow jet was observed along the southern portions of the line, but was not simulated.
- A descending front-inflow jet was observed along the northern porions of the line, but was not simulated.
- An upshear anvil was simulated while a predominantly downshear anvil was observed.
- As a result of the downshear anvil not being simulated, the suppression zones were not modeled and the discrete mode of propagation observed in the south was not simulated.
- A LFC of 1.7 km AGL was present in the environment used in the simulations, while a LFC of 3.1 km was found in the observed environment. This difference resulted in new convection forming not along the leading edge of the gust front, but rather 7-10 km behind the leading edge.

- Shear was confined below 5 km in the simulations, while strong shear above 5 km was observed.
- An upshear tilted updraft throughout the depth of troposphere was simulated, while the observations showed a low-level upshear tilted updraft but a nearly upright mid to upper-level updraft.
- The original convective cells lasted from two to three hours in this case, but lasted for approximately one hour in the simulations.
- A squall line was maintained in this low to mid-level weakly sheared environment, while could not be maintained in a similar environment in the simulations.

The simulations of RKW and WKR suggested that the observed features of squall lines could be explained through a balance between the circulations induced by the low-level ambient vertical shear of the horizontal wind ahead of the line and that induced by the horizontal buoyancy gradient along the leading edge of the convectively generated cold pool. These circulations dictated the orientation of the updraft which was key to understanding the structure and longevity of squall lines. Although this balance may be

significant in some cases, observations in this case suggests in differing environments, the hypothesis may need to be expanded.

In this case, the drier thermodynamic profile resulted in convection forming not along the leading edge of the gust front, but rather 7-10 km behind the leading edge and approximately 1.8 km above the top of the cold pool. At this location, the impact of the cold pool induced circulation was minimized. The tilt of the updraft is hypothesized to have resulted from conservation of momentum.

While the low-level shear has been identified as most critical to squall line development, strong upper-level shear present in this case was significant to the establishment of a leading anvil. The leading anvil allowed for the development of a suppression zone which in turn resulted in a discrete mode of squall line propagation along a portion of the squall line. Additionally, many of the observed features of this case may be explained by the non-hydrostatic forces induced by the squall line's relative motion in the ambient shear. Though not proved, asymmetries within the line itself may have been caused in part by the variation in the orientation of the squall line relative to the ambient shear.

The topography helped create small-scale variations in airmass properties along the line. For example, along the

northern portion of the line, a drier, hotter surface layer coupled with a deeper well-mixed sub-cloud layer was observed. To the south, a moister, cooler surface layer was coupled with a shallower well-mixed sub-cloud layer. These differing air masses resulted in asymmetries seen in a variant updraft structure and variable potential for evaporational cooling below the cloud.

The cold-pool/low-level ambient vertical wind shear conceptual model addresses many of the observed features within squall lines. Given the great degree of inhomogeneity that is typically present within the environment at any given time, a simplistic, homogeneously initialized model may lead to misleading conclusions about all squall lines. Observations of this squall line did not fit the conceptual model nor could they be explained purely by a circulation balance along the leading edge of the cold pool. Inhomogeneities in the wind shear (caused by differing orientations) and thermodynamic fields appeared to have been significant in explaining the alongline variance observed in this case.

Recent work by Skamarock et al. (1994) has begun to address these inhomogeneities. Future numerical simulations should consider both typical spatial and temporal variations within the environment. Also, within the context of the homogeneous environment used in the RKW and WKR simulations,

more sensitivity tests should be performed modifying the LFC/LCL, CAPE, and upper-level wind profiles with conditions more representative of the High Plains, squall line birthing grounds.

REFERENCES

Blanchard, D.O. and K.W. Howard, 1986: The Denver hailstorm of 13 June 1984. *Bull. Amer. Meteor. Soc.*, 67, 1123-1131.

Bluestein, H.B. and M.H. Jain, 1985: The formation of mesoscale lines of precipitation: Severe squall lines in Oklahoma during the spring. *J. Atmos. Sci.*, 42, 1711-1732.

_____, ____, and G.T. Marx, 1987: Formation of mesoscale lines of precipitation: Severe squall lines in Oklahoma during the spring. *Preprints, 3rd Conf. on Mesoscale Processes*, Vancouver, B.C., Amer. Meteor. Soc., 198-199.

Brady, R.H. and E.J. Szoke, 1989: A case study of non-mesocyclone tornado development in northeast Colorado: Similarities to waterspout formation. *Mon. Wea. Rev.*, 117, 843-856.

Brandes, E.A., 1990: Evolution and structure of the 6-7 May 1985 mesoscale convective system and associated vortex. *Mon. Wea. Rev.*, 118, 109-127.

Browning, K.A. and F.H. Ludlam, 1962: Air flow in convective storms. *Quart. J. R. Meteor. Soc.*, 88, 117-135.

Browning, K.A., 1964: Airflow and precipitation trajectories within severe local storms which travel to the right of the mean wind. *J. Atmos. Sci.*, 21, 634-639.

_____, and R. Wexler, 1968: The determination of kinematic properties of a wind field using Doppler radar. *J. Appl. Meteo.*, 7, 105-113.

Burghart, C., 1993: SUDS: The System for User-editing and Display of Soundings, Research Data Program, Atmospheric Technology Division, National Center for Atmospheric Research, 39 pp.

Byers, H.R. and R.R. Braham, 1949: The thunderstorm. U.S. Gov't Printing Office, Washington DC, 287 pp. [NTIS PB-234-515.]

Charba, J., 1974: Application of gravity current models to analysis of squall-line gust front. *Mon. Wea. Rev.*, 102, 140-156.

Chisholm, A.J. and J.H. Renick, 1972: The kinematics of multicell and supercell Alberta hailstorms. Alberta Hail Studies, Research Council of Alberta Hail Studies, Rep. 72-2, Edmonton, Canada, 24-31.

Cotton, W.R., R.L. George, and K.R. Knupp, 1982: An intense, quasi-steady thunderstorm over mountainous terrain -- Part I: Evolution of the storm-initiating mesoscale circulation. *J. Atmos. Sci.*, 39, 328-342.

— and R.A. Anthes, 1989: *Storm and Cloud Dynamics*. Academic Press Inc., San Diego, CA, pg. 425, 883 pp.

Crook, A. and B. Hobson, 1994: The relationship between horizontal rolls, convergence lines, and small-scale vortices. *Preprints, 6th Conf. on Mesoscale Processes*, Portland, Amer. Meteor. Soc., 234-237.

Davies-Jones, R.D., 1979: Dual-Doppler Radar Coverage Area as a Function of Measurement Accuracy and Spatial Resolution. *J. Applied Meteor.*, 18, 1229-1233.

Doswell, C.A. III, 1980: Synoptic-scale environments associated with High Plains severe weather. *Bull. Amer. Meteor. Soc.*, 61, 1388-1400.

Dudhia, J. and M.W. Moncrieff, 1987: A numerical simulation of quasi-stationary convective bands. *Quart. J. Roy. Meteor. Soc.*, 113, 929-967.

Fritsch, J.M., R.A. Maddox, and A.G. Barnston, 1981: The character of mesoscale convective complex precipitation and its contribution to warm season rainfall in U.S. *Preprints, 4th Conf. on Hydrometeorology*, Boston, Amer. Meteor. Soc., 94-99.

—, R.J. Kane and C.R. Chelius, 1986: The contribution of mesoscale convective weather systems to the warm-season precipitation in the United States. *J. Climate App. Meteor.*, 25, 1333-1345.

Fovell, R.G. and Y. Ogura, 1988: A numerical simulation of a midlatitude squall line in two dimensions. *J. Atmos. Sci.*, 45, 3846-3879.

Fujita, T.T., 1981: Tornadoes and downbursts in the context of generalized planetary scales. *J. Atmos. Sci.*, 45, 1511-1534.

Gamache, J.F. and R.A. Houze, Jr., 1982: Mesoscale air motions associated with a tropical squall line. *Mon. Wea. Rev.*, 110, 118-135.

Goff, R.C., 1976: Vertical structure of thunderstorm outflows. *Mon. Wea. Rev.*, 104, 1429-1440.

Houze, R.A. and P.V. Hobbs, 1982: Organization and structure of precipitating cloud systems. *Advances in Geophysics*, 24, 225-315

_____, S.A. Rutledge, M.I. Biggerstaff, and B.F. Smull, 1989: Interpretation of Doppler weather radar displays of mid-latitude mesoscale convective systems. *Bull. Amer. Meteor. Soc.*, 70, 608-619.

_____, B.F. Smull, and P. Dodge, 1990: Mesoscale organization of springtime rainstorms in Oklahoma. *Mon. Wea. Rev.*, 118, 613-654.

_____, 1993: *Cloud Dynamics*. Academic Press Inc., San Diego, CA, pg. 334, 573 pp.

Johnston, E.C., 1982: Mesoscale vorticity centers induced by mesoscale convective complexes. *Preprints, 9th Conf. on Wea. Forecasting and Analysis*, Seattle, Amer. Meteor. Soc., 196-200.

Karr, T.W. and R.L. Wooten, 1976: Summer radar echo distribution around Limon, CO. *Mon. Wea. Rev.*, 104, 728-734.

Kessinger, C.J., P.S. Ray, and C.E. Hane, 1983: The Oklahoma squall line of 19 May 1977. Part I: A multiple Doppler analysis of convective and stratiform structure. *J. Atmos. Sci.*, 44, 2840-2864.

Klimowski, B.A., 1994: Initiation and development of rear inflow within the 28-29 June 1989 North Dakota mesoconvective system. *Mon. Wea. Rev.*, 122, 765-779.

Klitch, M.A., J.F. Warner, F.P. Kelly, and T.H. VonderHaar, 1985: Convective cloud climatologies constructed from satellite imagery. *Mon. Wea. Rev.*, 113, 326-337.

Lafore, J. and M.W. Moncrieff, 1989: A numerical investigation of the organization and interaction of the convective and stratiform regions of tropical squall lines. *J. Atmos. Sci.*, 46, 521-544.

Leary, C.A. and R.A. Houze, 1979: The structure and evolution of convection in a tropical cloud cluster. *J. Atmos. Sci.*, 36, 437-457.

Leise, J.A., 1981: A multidimensional scale-telescoped filter and data extension package. NOAA Tech. Memo., ERL WPL-82, Wave Propagation Laboratory, 20 pp. [NTIS N82-31994.]

Maddox, R.A., 1980: Mesoscale Convective Complexes. *Bull. Amer. Meteor. Soc.*, 61, 1374-1387.

Marshall, J.M., A.M. Peterson, and A.A. Barnes, Jr., 1972: Combined radar-acoustic sounding system. *Appl. Opt.*, 11, 108-112.

Matejka, T. and R.C. Srivastava, 1991: An improved version of the extended velocity-azimuth display analysis of single-Doppler radar data. *J. Atmos. Oceanic Tech.*, 8, 453-466.

Menard, R.D. and J.M. Fritsch, 1989: An MCC-generated inertially stable warm core vortex. *Mon. Wea. Rev.*, 117, 1237-1261.

Mohr, C.G. and L.J. Miller, 1983: CEDRIC - A software package for Cartesian space editing, synthesis and display of radar fields under interactive control. Preprints, 21st Conf. on Radar Meteorology, Boston, Amer. Meteor. Soc., 569-574.

Moncrieff, M.W. and M.J. Miller, 1976: The dynamics and simulation of tropical cumulonimbus and squall lines. *Quart. J. R. Meteor. Soc.*, 102, 373-394.

Neilliey, P.P., N.A. Crook, E.A. Brandes, M. Dixon, C. Kessinger, C. Mueller, R. Roberts, J.D. Tuttle, and J.W. Wilson, 1993: The Real-time Analysis and Prediction of Storms program. 5th Int'l Conf. on Aviation Wea. Systems, Amer. Meteor. Soc., 62-64.

Neiman, P.J., P.T. May, B.B. Stankov, and M.A. Shapiro, 1991: Radio Acoustic Sounding System Observations of an Arctic Front. *J. Applied Meteor.*, 6, 881-892.

Newton, C.W., 1950: Structure and mechanism of the prefrontal squall line. *J. Meteor.*, 7, 210-222.

Ogura, Y. and M.-T. Liou, 1980: The structure of a midlatitude squall line: A case study. *J. Atmos. Sci.*, 37, 553-567.

Oye, R. and R. Carbone, 1981: Interactive Doppler editing software. *Preprints, 20th Conf. on Radar Meteorology*, Boston, Amer. Meteor. Soc., 683-689.

_____, 1994: REORDER: A program for gridding radar data, Field Observing Facility, National Center for Atmospheric Research, 20 pp.

Raymond, D., 1978: Pressure perturbations in deep convection. *J. Atmos. Sci.*, 35, 1704-1711.

Rotunno, R., J.B. Klemp, and M.L. Weisman, 1988: A theory for strong, long-lived squall lines. *J. Atmos. Sci.*, 45, 463-485.

Schmidt, J.M. and W.R. Cotton, 1989: A high plains squall line associated with severe surface winds. *J. Atmos. Sci.*, 46, 281-302.

Skamarock, W.C., M.L. Weisman, C.A. Davis, and J.B. Klemp, 1994: The evolution of simulated mesoscale convective systems in idealized environments. *Preprints, 6th Conf. on Mesoscale Processes*, Portland, Amer. Meteor. Soc., 407-410.

Smull, B.F. and R.A. Houze, Jr., 1985: A midlatitude squall line with a trailing region of stratiform rain: radar and satellite observations. *Mon. Wea. Rev.*, 113, 117-133.

____ and _____, 1987a: Dual-Doppler radar analysis of a mid-latitude squall line with a trailing region of stratiform rain. *J. Atmos. Sci.*, 44, 2128-2148.

____ and _____, 1987b: Rear inflow in squall lines with trailing stratiform precipitation. *Mon. Wea. Rev.*, 115, 2869-2889.

Stirling, J. and R.M. Wakimoto, 1989: Mesoscale vortices in the stratiform region of a decaying midlatitude squall line. *Mon. Wea. Rev.*, 117, 452-458.

Struach, R.G., D.A. Merritt, K.P. Moran, K.B. Earnshaw, and D. van de Kamp, 1984: The Colorado wind profiling network. *J. Atmos. Oceanic Technol.*, 1, 37-49.

Szoke, E.J., M.L. Weisman, J.M. Brown, F. Caracena, and T.W. Schlatter, 1984: A subsynoptic analysis of the Denver tornadoes of 3 June 1981. *Mon. Wea. Rev.*, 112, 790-808.

Thorpe, A.J., M.J. Miller, and M.W. Moncrieff, 1982: Two-dimensional convection in nonconstant shear: a model of midlatitude squall lines. *Quart. J. Roy. Meteor. Soc.*, 108, 739-762.

Tripoli, G.J. and W.R. Cotton, 1986: Numerical Study of an observed orogenic mesoscale convective system. Part 1: Simulated Genesis and Comparison with Observations. *Mon. Wea. Rev.*, 117, 273-304.

Wallace, J.M., 1975: Diurnal variations in precipitation and thunderstorm frequency over the conterminous United States. *Mon. Wea. Rev.*, 103, 406-419.

Wakimoto, R.M., 1982: The life cycle of thunderstorm gust fronts as viewed with Doppler radar and rawinsonde data. *Mon. Wea. Rev.*, 110, 1060-1082.

Weisman, M.L. and J.B. Klemp, 1982: The dependence of numerically simulated convective storms on vertical wind shear and buoyancy. *Mon. Wea. Rev.*, 110, 504-520.

____ and ____, 1984: The structure and classification of numerically simulated convective storms in directionally varying wind shears. *Mon. Wea. Rev.*, 112, 2479-2498.

____ and ____, 1986: Characteristics of isolated convective storms. *Mesoscale Meteorology and Forecasting*, Amer. Meteor. Soc., 331-358.

____, ____, and R. Rotunno, 1988: Structure and evolution of numerically simulated squall lines. *J. Atmos. Sci.*, 45, 1990-2013.

____, 1992: The role of convectively generated rear-inflow jets in the evolution of long-lived mesoconvective systems. *J. Atmos. Sci.*, 49, 1826-1847.

Wilczak, J.M. and J.W. Glendening, 1988: Observations and mixed-layer modeling of a terrain-induced mesoscale gyre: The Denver cyclone. *Mon. Wea. Rev.*, 116, 2688-2711.

Young, G., 1995: Associate Professor, Pennsylvania State University. From conversation on 8 June 1995.

Zhang, D.L. and J.M. Fritsch, 1987: Numerical simulation of the meso β -scale structure and evolution of the 1977 Johnstown flood. Part II: Inertially stable warm-core vortex and mesoscale convective complex. *J. Atmos. Sci.*, 44, 2593-2612.

Zipser, E.J., 1977: Mesoscale and convective-scale downdrafts as distinct components of squall line structure. *Mon. Wea. Rev.*, 105, 799-814.

— and T.J. Matejka, 1982: Comparison of radar and wind cross-sections through a tropical and a Midwestern squall line. *Preprints, 12th Conf. on Severe Local Storms*, San Antonio, Amer. Meteor. Soc., 342-345.